COMPUTER SIMULATION STUDIES OF FASTION YTTRIA-STABILISED CUBIC ZIRCONIA

By: Pudumo Jimmy Chaba

Submitted in fulfilment of the requirements for the degree of Master of Science in the Department of Physics in the Faculty of Mathematics and Natural Sciences, University of the North.

Supervisor: Professor Phuti Esrom Ngoepe

Turfloop, 20 November 1999

Private Bag x1106

Sovenga

0727

DECLARATION

I declare that the dissertation hereby submitted to the University of the North for the degree of Master of Science has not previously been submitted by me for a degree at this or any other university, that it is my own work in design and in execution, and that all material contained therein has been duly acknowledged.

.....

Pudumo J Chaba

20 November 1999

TO MY PARENTS

KANYANE AND LEKGAU

AND MY WIFE

LEBOGANG

ACKNOWLEDGEMENTS

My sincerest thanks to a distinguished scholar and supervisor, Professor P E Ngoepe, who has read the drafts of the dissertation with considerable care. His comments and suggestions inspired many improvements in this work, and greatly enhanced its usefulness as a referral material in the studies of yttria-stabilised cubic zirconia.

The investigation of the fundamental properties of cubic zirconia has necessarily involved the assistance of many people. It is hard to imagine anywhere besides the University of the North (UNIN) where this work could have been done. To this end, I would like to thank the UNIN management as well as the Computer Centre staff. The latter gave their time generously and responded quickly to a number of requests.

I would be extremely remiss if I did not thank Khomotso Reginald Kganyago and Ben Fourie for writing some of the software that was used to analyse the data collected from molecular dynamics simulations. My sincere gratitude also goes to Francis Pratt for typing the initial drafts of this dissertation.

I also thank my parents, my wife and members of my family for their unfailing support and encouragement.

ABSTRACT

Stabilised cubic zirconia is an important engineering material. Its high ionic conductivity, especially at high temperatures, makes it suitable for use as an electrolyte in solid oxide fuel cells as well as in devices such as oxygen sensors, electrochemical oxygen pumps, susceptors for induction heating, resistance heating elements and electrodes for magnetohydrodynamic power generators.

At the fundamental level, the nature of the defect interactions between the impurity cations and the oxygen vacancies is not well understood and presents challenging problems. In the present investigation, computer modelling methods were used to clarify the nature of the defect structure and its effects, the defect interactions and ordering, the transport mechanism as well as related properties in ZrO_2 (x mol % Y_2O_3), for x = 9.4, 15, 21 and 24. The defect and thermodynamic properties of this material were investigated using static lattice simulations, using the CASCADE and THBREL computer codes, respectively. The transport properties were derived from molecular dynamics simulation techniques using the FUNGUS code.

The present investigation presented for the first time elastic constants, and their temperature dependences, in 9.4 mol%, 15 mol%, 21 mol% and 24 mol% concentrations using the complementary computer simulation techniques. The calculated values of elastic constants agreed well with those from experiment. Various configurations were tested and it was found that in general the *I*-type configuration was most stable; and was subsequently used as the structural entity on which supercells for molecular dynamics (MD) calculations were formed.

Furthermore, the oxygen vacancies were found to be preferentially located at NNN positions to the dopant yttria cations, in agreement with experimental results and computer simulation studies on calcia-stabilized cubic zirconia.

The magnitudes of the oxygen ion diffusion coefficients were found to be comparable to those of liquids as in other fastion conductors. These magnitudes decreased with increasing yttria content. This was ascribed to the trapping of oxygen vacancies in large defect complexes. The magnitudes also decreased with decreasing temperature as in other fluorite structured materials.

Cation-cation and cation-anion radial distribution functions (RDFs) were found to be typical to those found in solids. Thus, the FCC structure, even at a high temperature such as 1600 K, was preserved indicating that yttria-stabilised cubic zirconia is a solid electrolyte. On the otherhand, anion-anion RDFs were typical to those found in liquids, indicating that the oxygen ions formed a weakly correlated subsystem.

TABLE OF CONTENTS

LIST OF TABLES

LIST OF FIGURES

CHAPTER 1

INTRODUCTION AND GENERAL SURVEY

Solid electrolytes, more popularly known as fastion conductors, are electrolytes whose ionic conductivities, well below their melting points, are comparable with those found in the liquid state. These materials are of particular interest to both physicists and technologists because of their intricate conduction mechanism. As a result, the past decade has witnessed the introduction of new techniques, both theoretical and experimental, for investigating these compounds. At the moment research on defect, thermodynamic, transport and structural properties is at such an advanced stage that the properties of these materials are understood much better. This chapter outlines fastion conduction, phenomenological models, properties of yttria-stabilised cubic zirconia and reviews previous studies on fastion conductors, with special reference to yttria-stabilised cubic zirconia, using both experimental and theoretical techniques.

1.1 IONIC TRANSPORT AND DEFECT MECHANISMS

In this section ionic transport in fastion conductors based on different types of defect mechanisms is discussed. This will be followed by a brief discussion of the phenomenological model, which is an essential theoretical model explaining the mechanisms responsible for order-disorder transitions.

The basic theory of ionic transport in solids at the macroscopic level concern both diffusion and conductivity, i.e. matter and charge transport (Wagner 1943, Catlow 1986a). A hop diffusion model is appropriate in fastion conductors with a hopping distance $d_o \approx 2\text{Å}$, diffusion coefficient $D = 10^{-5}\ cm^2s^{-1}$ and site dwell time t_{dwe}

($\approx$ 3ps) $\geq$ t_{sp} ($\approx$ 0.5 ps), where t_{sp} denotes the time spent between sites. Thus diffusion is a process of discrete jumps of particles over an energy barrier and it is this hopping process that gives rise to ionic conductivity, provided an energetically accessible empty site is available in the immediate vicinity of the ion.

Chandra (1981) has identified five properties that characterise fastion conductors :

(a) the number of available empty sites exceeds the number of ions;

(b) the ionic conductivity is high $(10^{-1} - 10^{-4})\Omega^{-1}cm^{-1}$;

(c) the principal charge carriers are ions which implies an ionic transference number close to unity;

(d) the electronic conductivity is small, with electronic transference number, t_e, less than 10^{-4}.

(e) the activation enthalpy is low.

During diffusion and ionic conduction, ions move through the lattice. The diffusion process only occurs when defects are present in the lattice. The four major types are :

(a) Schottky defects, which form when positive and negative ions leave their normal lattice sites, thereby creating vacancies, and eventually residing at internal or external surfaces;

(b) Frenkel defects, which occur when ions move to intestitial positions and leaving vacancies at their lattice sites;

(c) dislocation and boundaries;

(d) electronic defects and substitutions.

The first two types of defects are mainly responsible for ionic transport. Some possible transport mechanisms involving these defects are shown in figure 1.1. Figure 1.1(a) shows the vacancy mechanism in which atoms merely jump into vacancies while figures 1.1(b) and 1.1(c) involve interstitials or Frenkel defects. An interstitial mechanism (figure 1.1(b)) involves hops by interstitials from interstice to interstice. Another manner in which interstitials can be transported is when an interstitial hops to a normal lattice site pushing the atom there to another interstice and is known as the "concerted" or "interstitialcy" mechanism (figure 1.1(c)). Conduction via defects involving several disordered atoms in a ring, giving rise to a "ring" mechanism, has been identified (Chandra 1981).

1.2 PHENOMENOLOGICAL MODELS

The phenomenological model is one of the theoretical approaches that are used to clarify the mechanisms responsible for the transitions to the fastion phase. The second theoretical model is computer simulation, discussed in Chapter 2. Other theoretical models are discussed by Boyce and Huberman (1979), Chandra (1981) and Ngoepe (1987).

In the phenomenological models, the interaction of thermally generated defects determines whether the charge carrier density will increase abruptly or continuously at the transition temperature. This results in an associated increase in conductivity. Several phenomenological approaches to the diffuse transition have been based on defect interactions (Catlow *et al.* 1978, Huberman 1974, Rice *et al.* 1974, Welch and Diënes 1977). Illustration of how the high temperature phase transition may be simulated, will be based on the models proposed by Huberman (1974), Rice *et al.* (1974) and Welch and Diënes (1975, 1977).

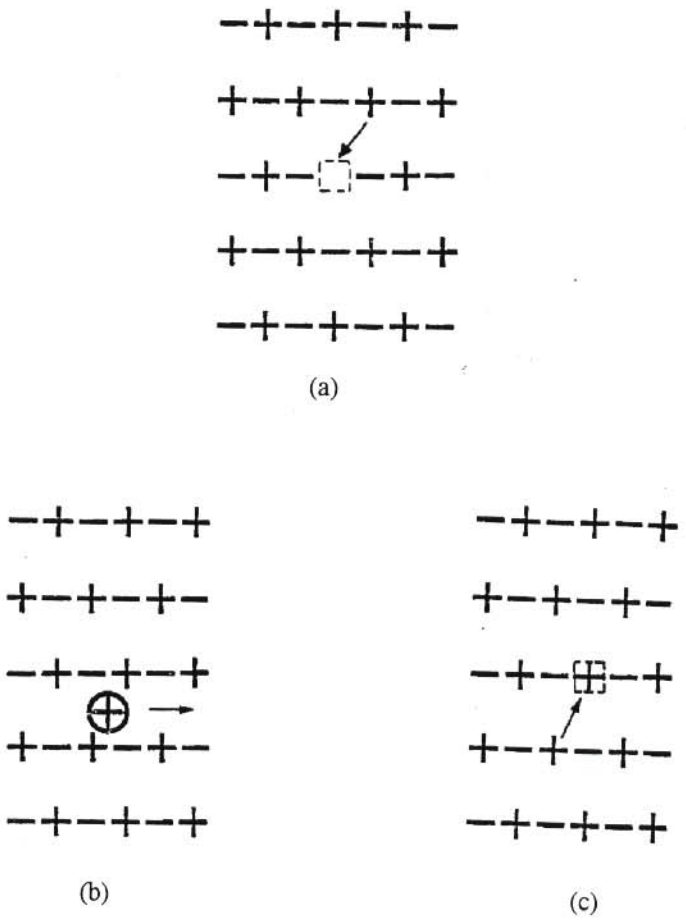

Figure 1.1 Possible ion transport mechanisms in ionic solids: (a) vacancy mechanism, (b) interstitial mechanism and (c) interstitialcy mechanism

The phenomenological models are generally characterised by the free energy of the crystal having the form

$$F(n) = nh_o - h_i(n) - nS_vT - S_c(n)T \qquad 1.2.1$$

where n denotes the interstitial concentration, h_o is the Frenkel defect formation energy at $n = 0$, $h_i(n)$ is the defect interaction energy which reduces the effective Frenkel energy as n increases, S_v is the defect vibrational entropy, S_c is the configurational entropy and h_o is the Frenkel pair formation energy at $n = 0$.
The formation energy is given by

$$E(n) = nh_o - h_i(n)$$

in accordance with the Huberman's model. The Welch and Diënes model assumes that $E(n)$ varies quadratically with n as

$$E(n) = nh_o - h'n^2$$

without going into details of defect interactions. The condition of a free energy minimum

$$(\partial F/\partial n)_T = 0$$

determines the equilibrium value of n at a fixed temperature in each model. The different types of phase transitions are determined by the values of the phenomenological constants chosen, the detailed nature of the transition and the disordered state being controlled by $h_i(n)$ and S_c (Strassler and Kittel 1965, Huberman 1974, Rice *et al.* 1974, Welch and Diënes 1975, 1977).

In fluorites a quantitative application of equation 1.2.1 is consistent with the anion Frenkel defect concentration rising rapidly near the transition temperature T_c. This is due to the attractive defect interactions. High temperature Brillouin scattering studies (Catlow *et al.* 1978) indicated that repulsive interactions become important at concentrations of $n \geq 0.1$ and suppress further generation of defects. This would result in limited disorder as opposed to the earlier suggestions of massive

fluorine disorder in a "liquid-like" state (Derrington and O'Keefe 1973).

1.3 YTTRIA-STABILISED CUBIC ZIRCONIA

In this section properties of yttria-stabilised cubic zirconia will be discussed in terms of structure, transformation and cubic stabilisation. This is particularly important since these aspects have a significant bearing on the observed defect and transport mechanisms in this material.

Stabilised cubic zirconia is an important engineering material. Apart from its use as a structural material, it also finds applications in a variety of devices because of its diversified properties. Its high ionic conductivity, especially at high temperatures, makes it suitable for use as an electrolyte in solid oxide fuel cells (Etsell and Flengas 1970, Dell and Hooper 1978, Steele 1992, 1995, Moulson and Herbert 1990, Minh 1993, Kilner *et al.* 1997) as well as in devices such as oxygen sensors (Ketron 1989, Etsell and Flengas 1970), galvanic cells for measuring both oxygen activities in gaseous environments and thermodynamic quantities (Steele 1968, Goto and Pluschkell 1972, Rapp and Shores 1970, Tretyakov and Kaul 1972, Etsell and Flengas 1970, Schmalzreid and Pelton 1972), resistance heating elements and electrodes for magnetohydrodynamic power generators (Wolff 1969, Etsell and Flengas 1970, Hammou *et al.* 1971) and susceptors for induction heating (Etsell and Flengas 1970, Hull *et al.* 1988).

1.3.1 STRUCTURAL PROPERTIES

A low temperature fluorite structure (Fm3m) may be viewed as a simple cubic array of anions with cations occupying alternate cube centers (Hodby 1974). In a primitive cube of side x the fluorite structure consists of three interpenetrating face centered cubic lattice with the first lattice of species A located at origin (0, 0, 0)

and having a translational vector

$$\left(0 \quad , \quad 0.5\,x \quad , \quad 0.5\,x\right);$$

$$\left(0.5\,x \quad , \quad 0 \quad , \quad 0.5\,x\right);$$

$$\left(0.5\,x \quad , \quad 0.5\,x \quad , \quad 0\right)$$

Ions of type B are located on two further lattices with similar translational vectors but with the origin at $\left(0.25\,x,\ 0.25\,x,\ 0.25\,x\right)$ and $\left(0.75\,x,\ 0.75\,x,\ 0.75\,x\right)$. The interstitial site is located at a cube center coordinated by eight ions of type B. Both the A ion and interstitial sites possess an O_h symmetry whilst the site of the B ion has a T_{2g} symmetry. The fluorite structure provides a close packing of different ion species and two individual hard sphere-like ions are in contact when the condition

$$4.45 \geq \frac{r(A)}{r(B)} \geq 0.73$$

is satisfied (Wyckoff 1965). Here r(A) and r(B) represent the radii of species A and B, respectively. Contact between distinct ions is favoured predominately by strongly ionic compounds with formula AB_2 possessing large ions of component A. The fluorite structure in yttria-stabilised cubic zirconia is shown in figure 1.3.1.1.

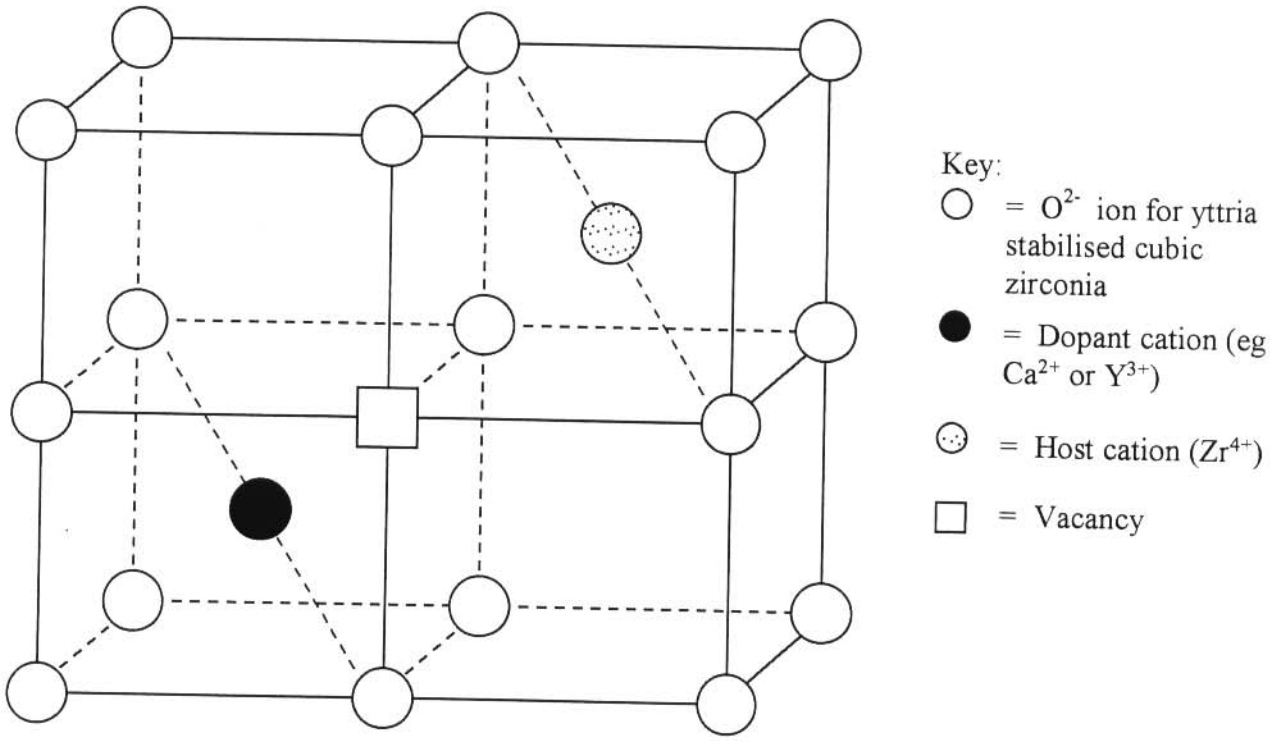

Figure 1.3.1.1 The fluorite structure of cubic zirconia

1.3.2 STRUCTURAL TRANSFORMATION IN ZrO_2

More than five polymorphisms of zirconia are reported in the literature (Subbarao 1981, Ho 1982, McCullough and Trueblood 1959, Smith and Newkirk 1965, Teufer 1962). They have been examined as a function of temperature using infrared (Phillippi and Mazdiyasni 1971, Feinberg and Perry 1981), Raman (Kermidas and White 1974, Anastassakis *et al.* 1975, Ishigame and Sakurai 1977, Hamilton and Nagelberg 1984, Perry *et al.* 1985) and luminescence (Asher *et al.* 1976) spectroscopy. However, only there polymorphisms are well established.

Pure zirconia possesses a monoclinic structure $\left(P2_1/C\right)$ at ambient temperatures (Asher *et al.* 1976, Ishigame and Sakurai 1977). The monoclinic phase can be described as a distortion of the cubic fluorite (CaF_2)-type structure. The zirconium ions have a coordination number of seven. A structural transition to the tetragonal structure $\left(P4_2/nmc\right)$ occurs at about 1300 K. This form represents a slightly distorted fluorite structure (Teufer 1962, Smith and Newkirk 1965). This transition is athermal and diffusionless (Bansal and Heuer 1972), which is characteristic of a martenistic transformation. The transformation is further accompanied by a change in coordination from seven to eight. A tetragonal to cubic transformation was observed at about 2640 K (Smith and Cline 1962, Nikol'skii *et al.* 1972) with each Zr^{4+} ion still coordinated by eight equidististant O^{2-} ions since no bond configuration change occurs. The cubic phase of ZrO_2 has the fluorite structure Fm3m.

1.3.3 CUBIC STABILISATION OF ZrO_2

The polymorphism of pure ZrO_2 restricts the practical usefulness of pure zirconia as the structural transitions are accompanied by substantial and disruptive volume changes (about 9%). It is for this reason that interest has been centered on

compounds of zirconia which form a stable structure. Ruff and Ebert (1929) and Duwez *et al.* (1951) postulated that an oxide could stabilise ZrO_2 if its radius is similar to that of the zirconium cation and has a cubic fluorite structure. Dietzel and Tober (1953) added the requirement that the metal-oxygen bonds of the oxide must be more ionic than those of ZrO_2. These conditions are satisfied when oxides such as CaO and Y_2O_3 form non-stoichiometric compounds with zirconia such as ZrO_2(x mol% CaO) and ZrO_2(x mol% Y_2O_3), respectively (Etsell and Flengas 1970, Dell and Hooper 1978). A concentration of the stabilising oxide in the range 8 to 36 mol% is required to stabilise zirconia to the cubic phase (Duwez *et al.* 1951).

An aliovalent cation is a cation whose charge differs from that of the host cation. If the dopant ion has a lower vacancy than that of the host cation, an anion vacancy is formed; otherwise an interstitial anion vacancy is created. Thus, in zirconia systems one oxygen vacancy is produced if a host oxide cation, Zr^{4+}, is replaced by a divalent substitutional cation, Ca^{2+}, or by a pair of trivalent substitutional cations, Y^{3+}. These oxygen vacancies are introduced as charge compensating defects. Commercial cubic zirconias have the formulae $Zr_{1-x}Ca_xO_{2-x}$ and $Zr_{1-2x}Y_{2x}O_{2-x}$. The stabilised form of cubic zirconia is much less susceptible to thermal shock, is highly resistant to the effects of oxidising environments and is stable up to 2800 K. It is this high temperature reliability that makes stabilised cubic zirconia important in technology of materials. Some of the physical properties of cubic zirconia are given in table 1.3.3.1.

Table 1.3.3.1 Physical properties of cubic zirconia

Quantity	Magnitude	Unit
Y_2O_3 concentration range	8 - 36	mol%
Refractive index	2.15 - 2.18	
Transparent region	300 - 7000	nm
Hardness	7 - 8	Moh's scale
Lattice constant	5.14 - 5.22	10^{-10}m
Melting point	2800	K

1.4 LITERATURE REVIEW

Numerous experimental techniques, notably Brillouin scattering, ultrasonic, electrical conductivity and neutron, Raman and quasi-elastic scattering, have been used to study properties of fastion conductors.

Fundamental studies on cubic zirconias in the past decade have provided essential information that helped clarify not only the intricate defect and conduction mechanisms but the underlying structural properties as well. The observations and conclusions arrived at using both experiment and computer simulation are reviewed in this section.

1.4.1 EXPERIMENTAL CALCULATIONS AND OBSERVATIONS

The order-disorder transformation at 1300 K in both ZrO_2(x mol% CaO) and ZrO_2(x mol% Y_2O_3) systems has been the subject of numerous investigations (Carter and Roth 1968, Steele and Fender 1974, Allpress and Rossell 1975, Alpress *et al.* 1975, Faber *et al.* 1978, Hudson and Moseley 1976, Cohen *et al.* 1981, Morinaga

and Cohen 1979, 1980, Botha *et al.* 1993). Neutron scattering (Steele and Fender 1974, Faber *et al.* 1978) and x-ray diffraction (Cohen *et al.* 1981, Morinaga and Cohen 1979 1980) studies indicate that the disordered state, which lacks long-range order on the oxygen sublattice, results from the displacement of oxygen ions along the [100] direction. Thus, since these experiments were conducted at ambient temperature subsequent to cooling, static lattice displacements were often favoured in the intepretations. This was demonstrated by Feinberg and Perry (1981) in their Raman scattering work on ZrO_2 (12 mol% Y_2O_3). They compared the spectrum of the zirconia system with one phonon density of states derived from a rigid ion model and confirmed that the polarised spectra, arising from contributions of modes throughout the Brillouin zone, originate from the breakdown of wave vector selection rules owing to the structurally disordered oxygen sublattice. In particular, Steele and Fender (1974) observed smaller [111] outward motions in addition to the [100] movements of nearest-neighbour oxygen ions towards the vacancies.

Point defects have been identified as directly responsible for ionic transport (Wagner 1943, Etsell and Flengas 1970). However, at the fundamental level information on the nature of the defect structures and transport mechanisms giving rise to fastion conduction is sparse and present challenging problems. The ordering of defects has been observed in stabilised zirconia when annealed for prolonged periods below the transition temperature (Carter and Roth 1968, Dell and Hooper 1978). The observed gradual decrease in ionic conductivity was attributed to the ageing phenomenon originating from the ordering of both cations and anions (Allpress *et al.* 1975, Allpress and Rossell 1975).

Hudson and Moseley (1976) have suggested the presence of oriented intergrowths

of monoclinic ZrO_2 to be responsible for the observed diffuse electron scattering and for the resulting super structure. Faber *et al.* (1978) explained neutron scattering results from single crystals of ZrO_2(x mol% CaO) and ZrO_2(x mol% Y_2O_3) in terms of collective [100] displacements on the oxygen sublattice. On the other hand, x-ray diffraction studies (Morinaga and Cohen 1979 1980) indicate [100] displacements in both ordered and disordered states. They suggested that the [100] displacement in the disordered state may be a precursor to the ordering process and may be related to the transformation from cubic to tetragonal phase at 2573 K. Teufer (1962) described the tetragonal phase as resulting from anion displacements from the cubic fluorite positions along [100] directions. The motion of oxygen ions results in quasi-elastic light scattering (Perry and Feinberg 1980, Suemoto and Ishigame 1983). Both workers associated the polarizability fluctuations with the motion of the oxygen ions. The oxygen ions migrating to neighbouring sites have to overcome barrier heights, which are dependent on the arrangement of the Y^{3+} and Zr^{4+} ions.

Andersen *et al.* (1985, 1986b) and Osborn *et al.* (1986) used high temperature coherent diffuse neutron scattering to probe both the local deformations in the vicinity of an oxygen vacancy and longe-range correlations. The observed room temperature diffuse intensity was ascribed to two main contributions: (a) a relatively vacancy-free tetragonally distorted region whose volume decreases with increasing dopant concentration and (b) a region in which vacancies and their aggregates are present. The aggregates were found to be stable on the time scale which can be determined by neutron scattering up to a temperature of 1900 K in ZrO_2 (9.4 mol % Y_2O_3). The scattering becomes quasi-elastic above 1200 K. This behaviour was attributed to more stable small defect clusters or single vacancies, and was associated with ionic conduction. Furthermore, the tetragonal region was

found to be negligible for Y_2O_3 concentrations above 18 mol % suggesting a direct relation between the cubic phase stabilisation and the mechanism involved in the distortion.

Elastic constants measurements are crucial since these quantities provide fundamental information concerning the interionic forces in solids. Furthermore, they are used extensively in the derivation of the interionic potentials used in computer simulation studies of solids (Catlow 1986a). Elastic constants of cubic zirconia have been measured at room temperature by ultrasonic (Pace *et al.* 1969, Farley *et al.* 1972, Hailing and Saunders 1982, Hart *et al.* 1986) and Brillouin scattering techniques (Botha *et al.* 1993, Aleksandrov *et al.* 1975, Chistyi *et al.* 1977) as a function of composition. The ultrasonic measurements were extended to 1000 K by Kandil *et al.* (1984) who observed a quasi-linear decrease in elastic constants associated with lattice anharmonicity. The quasi-linear behaviour was explained in terms of the quasi-harmonic approximation (Garber and Granato 1975). A study by Ngoepe and Comins (1987) using Brillouin scattering methods in ZrO_2(x mol% Y_2O_3), with x = 9.4, 15, 21 and 24, have shown the softening of the acoustic mode frequencies above about 1100 K which are somewhat similar to those observed in other fluorite-structured compounds.

High temperature Brillouin scattering and refractive index measurements (Botha *et al.* 1993) on the behaviour of the elastic constants of cubic zirconia has shed new light on the properties of ZrO_2(x mol% Y_2O_3). This investigation presented for the first time a complete set of elastic constants of cubic zirconia in the 300 - 1400 K temperature region. A significant elastic constant anomaly was observed above a characteristic transition temperature, T_c, which is dependent of the concentration of Y_2O_3. This behaviour was attributed to cooperative development of disorder

emanating from defect-defect interactions. It was concluded that the observed significant differences associated with disorder process, leading to features common with the transition to the fastion phase in the other fluorites, suggest a different nature of defects created in cubic zirconia.

1.4.2 THEORETICAL CALCULATIONS

In this section previous results obtained from computer simulation studies are reviewed. These concern the calculation of defect energies, ionic transport and structural properties obtained using static lattice simulations, molecular dynamics methods, Monte Carlo techniques and quantum mechanical methods. The first two techniques are the major methods in the present investigation and as such Chapter 2 discusses them in detail.

1.4.2.1 *STATIC LATTICE SIMULATION*

Static lattice simulation techniques have been used to investigate the behaviour of elastic constants in alkaline-earth fluorides CaF_2, SrF_2, BaF_2 and PbF_2 (Catlow and Norgett 1973, Harley *et al* 1975, Catlow *et al.* 1977, 1978). All the elastic constants, and their combinations, were observed to decrease linearly with increasing temperature up to the transition temperature, T_c. Vacancy activation energies in CaF_2, SrF_2, BaF_2 and $SrCl_2$ were calculated by Catlow and Norgett (1973) and Catlow *et al.* (1977). In general, low activation energies, as compared to experimental values, were obtained, indicating the uncertainity around the precise nature of the anion migration mechanism. Leslie (1983) has attributed the observed differences between the calculated and the experimental values to the exclusion of the treatment of ligand field effects while Harding (1985) ascribed the discrepancies to the neglect of entropy terms rather than problems with the adopted interionic potential model. Defect formation and activation energies in the tysonite-structured

LaF_3 were calculated using the CASCADE computer program by Jordan and Catlow (1987). Frenkel disorder was found to be favourable. Ngoepe *et al.* (1990) used the THBREL code to determine lattice energies and elastic constants in LaF_3. The calculated temperature gradients of the elastic constants were reproduced satisfactorily below 1150 K. Furthermore, Frenkel disorder was found to be favourable, confirming ealier results by Jordan and Catlow (1987).

The current direction of the field of static lattice simulations is increasingly towards complex and semi-ionic materials. Catlow (1986b) determined the defect energies of BaT_iO_3 and observed that Schottky defects are favourable in this material. Catlow (1981) reviewed earlier applications to non-stoichiometric oxides such as $Fe_{1-x}O$, TiO_{2-x} and UO_{2+x}. Catlow and Fender (1975) used the HADES program to perform lattice energy calculations based on the Born model to examine the possible structures in $Fe_{1-x}O$. They identified a basic and stable cluster comprising four vacancies and one tetrahedral Fe^{3+} ion, i.e. 4:1 cluster. Their results agree with those from microscopy (Iijima 1974) and neutron diffraction (Cheetham *et al.* 1971) studies. The complex near-stoichiometric TiO_{2-x} was investigated by Catlow and James (1982) and they observed the predominance of vacancy point defects, which aggregate into shear planes at higher deviations from stoichiometry. Jackson *et al.* (1986) used the CASCADE simulation program to determine the dependence of the calculated Frenkel formation energy on the size of region I in uranium oxide. Their results show a saddle point energy occuring with 200 particles, in contrast to 100 particles used by Catlow (1977). The work by Jackson *et al.* (1986) gave high cation migration energies. This was attributed to the inadequacies of the ionic model to describe the interactions at the saddle point for cation migration in uranium dioxide.

Doped fluorite oxides differ from the halide systems discussed above in that disorder is generated by impurities rather than thermally. The most widely studied fluorite oxides are ZrO_2 and CeO_2. When stabilising agents such as CaO and Y_2O_3 are added to ZrO_2, the dopant cation substitutes for the zirconium ion and oxygen vacancies are created for charge compensation. Butler *et al.* (1983) studied CeO_2 using both HADES and CASCADE simulation codes and concluded that the binding energies are strongly sensitive to the radius of the impurity ions. The calculations by Jackson *et al.* (1986) showed that a large component of the binding energy is due to elastic effects arising from the mismatch between dopant and host ion radii. It is for this reason that the largest energy was obtained for Sc^{3+} which has the smallest radius and hence the largest mismatch, in agreement with results from conductivity measurements by Gerhardt-Anderson and Norwick (1981).

The nature of the interaction between the dopant cation and the oxygen vacancies has been widely studied (Etsell and Flengas 1970, Tien and Subbarao 1963, Rhodes and Carter 1962, Allpress *et al.* 1974). Dwivedi and Cormack (1990) investigated the defect structure of calcia-stabilised cubic zirconia by atomistic simulation techniques using CASCADE. Anion defect association energies for oxygen vacancies and impurity calcium ion at both NN and NNN positions suggested the preferential sitting of the vacancies in the NNN position with respect to the dopant cation at low concentration. This is in contrast with results from diffuse scattering of x-rays (Morinaga *et al.* 1979 1980) and neutrons (Steele and Fender 1974) and EXAFS studies (Tuiler *et al.* 1987) but agrees with electron microscopy results (Allpress and Rossell 1975) and EXAFS studies (Catlow *et al.* 1986). Veal *et al.* (1988) suggested that a mixture of vacancies sitting at NN and NNN positions might occur at high concentrations based on observations from EXAFS studies. Dwivedi and Cormack (1990) explained their findings in terms of the larger size of

Ca^{2+} ions which impose a cubic symmetry on the anion sublattice at NNN positions. Anion vacancy association energies for NN positions were found to be negative. Schottky intrinsic disorder with low energy per defect was identified, in contrast with the prevalence of Frenkel disorder in other fluorite-structured oxides (Buchanan 1986).

Mackrodt and Woodrow (1986) also reported a lower value of energy per defect for Schottky disorder in ZrO_2. Dwivedi and Cormack (1990) argued that because of the small radius of the Zr^{4+} ion, ZrO_2 has the natural tendency to transform to the monoclinic form in which the zirconium ion is sevenfold coordinated by oxygen ions, thus providing a closer packing of the oxygen ions around the cation. Anion vacancy migration energies were found to be in the range 0.8 - 1.1 eV (Oishi and Ando 1984, Etsell and Flengas 1970). Dwivedi and Cormack (1990) calculated this energy to be $\sim$ 0.6 eV and suggested that a larger energy of migration might be obtained from large defect complexes.

1.4.2.2 *MOLECULAR DYNAMICS*

Fastion conduction was first demonstrated by Rahman (1976) using molecular dynamics (MD) simulation techniques in CaF_2. In a later study Gillan (1985) observed that diffusion of the anions occurs predominantly along the <100> directions and that the fluorine ions seemed to execute correlated motion. The observed steep slope of the mean-square displacement versus time graph show that the anions were diffusing rapidly while the constant long-time value for the cations implies that these were vibrating about their lattice positions, confirming that the system was in the solid state. Ngoepe and Catlow (1991) observed no anion diffusion in pure CaF_2 below the transition temperature T_c. However, doping this material with La^{3+} ions was seen to promote diffusion below T_c and suppress

diffusion above T_c.

Sindzingre and Gillan (1988) studied both liquid and solid UO_2 at constant pressure using the isobaric-isothermal ensembles introduced by Andersen (1980) and Nosi (1984). The simulation work confirmed that uranium dioxide is an oxygen fastion conductor in accord with neutron scattering experiments (Clausen *et al.* 1984a). The calculated elastic and dielectric constants were compared with those from experiment (Jackson *et al.* 1986) and the agreement was found to be good. The anion diffusion coefficient showed a continuous transition from low values at low temperatures to liquid-like values of about $10^{-5}cm^2s^{-1}$ and higher at high temperatures, in agreement with results obtained in other fluorite-structured materials (Hayes 1978, Gillan and Dixon 1980, Walker *et al.* 1982, Gillan 1986). The cation diffusion constant was found to be immeasurably small. Almost similar results were obtained in the liquid state, however, the cation diffusion coefficient was found to be comparable with the corresponding anion diffusion constant.

Shimojo and Okazaki (1992) have investigated microscopic diffusion mechanism in yttria-stabilised cubic zirconia by means of a polyhedron analysis method. The oxygen migration mechanism was found to be predominantly along the [100] direction and preferably between tetrahedra having a common Zr-Zr edge. The oxygen self-diffusion constants for the 4.85, 10.2 and 22.7 mol% Y_2O_3 at 1800° C were found to be 1.1, 1.9 and 1.6×10^{-6} cm^2/s, respectively, showing a maximum at 10.2 mol% Y_2O_3. In a subsequent study (Shimojo *et al.* 1992) the presence of dopant yttria ions was shown to strongly affect the diffusion of oxygen vacancies. Yttria ions promote oxygen ion migration at low concentrations but with increasing concentration, tetrahedra having the Y-Y edge increases, and the diffusion paths of the anions become restricted by neighbouring Y^{3+} ions, leading

to a decrease in diffusion constant. This was advanced as the explanation for the observed decrease in conductivity with increasing concentration above 10 mol%. This phenomenon was also attributed to a correlated migration of a diffusing ion. The degree of correlation was studied (Shimojo and Okazaki 1992) by examining the relation between successive migrations, especially the ratio of backward migration following the preceding forward one, since the backward migration cancels out the contribution of the forward migration. As the doping level increased the number of backward-forward migrations increased as well. However, at high concentrations most of the increases in oxygen migrations were local forward-backward, leading to a decrease in diffusive migration and diffusion constant.

Shimojo *et al.* (1992) have calculated partial pair distribution functions for all pairs of ions in yttria stabilised cubic zirconia. Cations were observed to form a well-defined FCC lattice while the anion-anion functions were seen to have a weak structure characteristic of a liquid. The NN distances in Zr-Zr were found to be slightly shorter than those for Zr-Y and Y-Y. This was explained in terms of local deformation on the FCC lattice. The shorter Zr-Zr distances arise from strong Coulomb attractions between Zr^{4+} ions on corners of tetrahedron and oxygen ions inside the tetrahedron. The Zr-O distances were shorter than the Y-O distances in agreement with results by Catlow *et al.* (1986) and Veal *et al.* (1988). The difference between Zr-O and Y-O distances was about 0.2 angstroms, which is longer than the distance between the cations. This showed that the oxygen ions inside the tetrahedron were shifted towards a zirconia ion from the normal fluorite position by the presence of the Y^{3+} ion. The first peak was found to heighten, accompanied by a slight decrease in cation-oxygen distance and a broadening in both $g_{Zr\text{-}O}(r)$ and $g_{Y\text{-}O}(r)$ profiles futher away from the first peak, with increasing yttria content. The observed broadening of the profile in $g_{O\text{-}O}(r)$ with increasing

concentration was ascribed to local deformation on the anion sublattice from a simple cubic lattice.

Diffusion in ZrO_2(x Y_2O_3) was found to occur predominatly on the oxygen sublattice (Li and Hafskjold 1995) using molecular dynamics. A maximum in oxygen diffusion was noted near 8 mol% Y_2O_3. The study further revealed that an increase in Y^{3+} - Y^{3+} neighbour clusters tend to trap more oxygen vacancies than isolated Y^{3+}. More such neighbour clusters tend to occur at higher concentrations of Y_2O_3 and lead to reduced oxygen diffusion.

Transport properties in ZrO_2(10 mol% Y_2O_3) were investigated (Khan *et al.* 1998) using computer simulation techniques in the temperature range 873 - 2073 K. The cation mean-square displacements were found to remain almost constant with time, confirming that cation diffusion is insignificant. In contrast, the oxygen ion diffusion increased rapidly with time. It was concluded that the presence of yttria as a stabiliser in zirconia enhances oxygen ion diffusion. Furthermore, results from radial distribution functions showed a considerable disorder in the oxygen sub-lattice. The degree of disorder was found to increase with increasing temperature.

1.4.2.3 *MONTE CARLO TECHNIQUES*

Monte Carlo (MC) simulation technique is essentially a method of computational statistical mechanics ideally suited for calculating ensemble averages in the canonical and grand canonical ensemble. Reviews and papers (Murch 1982a, b, 1984a, b, De Bruin and Murch 1973) give a good indication of the scope and range of application of MC methods. Murch et al. (1986) have combined MC techniques with static lattice simulation methods to study the intriguing problems related to the maximum in conductivity observed in CeO_2(x mol% Y_2O_3). They

noted that the efficacy of ion jumps in effecting conductivity decreases with increasing dopant concentration. The vacancy jumps become decreasingly effective in leading to bulk ionic conductivity at high doping levels, an observation which yields a qualitative insight into the origins of the observed maximum. It is evident that further work needs to be done but results already obtained illustrate the power and potential of Monte Carlo techniques in investigating diffusion in complex systems.

1.4.2.4 *QUANTUM MECHANICAL METHODS*

The simulation procedures discussed already are limited in their range of applications because they cannot be used to model color centers or defects in covalent materials with broken bonds such as semiconductors. In contrast, quantum mechanical (QM) methods are generally applicable to all kinds of defects. These methods involve endeavours at varying levels of approximation to solve the Schrödinger equation for the appropriate defect configurations. The technique has been used to study interstitials in diamond (Mainwood *et al.* 1978, Payne *et al.* 1992) where the $<100>$ split interstitial in a singlet state was found to be most stable. A similar result was obtained by Masri *et al.* (1983) in silicon. Successful applications of the related ab-initio Hartee-Fock methods on the study defects were reported in quartz (Mombourquette and Weil 1985). These studies have indicated the role that can be played by quantum mechanical methods on defect studies. These methods will become increasingly predictive with growing computer power.

Recently, ab-initio (Lindan *et al.* 1997) calculations based on both density functional theory (DFT) and Hartree-Fock (HF) methods were used to investigate the equilibrium structure of the stoichiometric and reduced TiO_2 (110) surface, the atomic and electronic structure of TiO_2 surfaces reduced by removal of oxygen and

addition of potassium as well as the molecular and dissociative adsorption of water at the (110) surface. It was found that both DFT and HF calculations give very similar predictions for the ionic displacements at the stoichiometric (110) surface. It was concluded that spin unpairing was a dominant effect on oxygen vacancies in both the bulk and at the surface. The unpairing of spins leads to a substantial lowering of the total energy and to the appearance of the localised states in the band gap which are observed experimentally.

1.5 MOTIVATION OF THE RESEARCH PROGRAM

The theoretical models presented in section 1.4 have contributed enormously to the understanding of a number of features such as the defect species involved in migration processes, the nature and configuration of defect interactions, defect mobility as well as the extent of disorder at and above the transition to the fastion phase. Information on high temperature elastic properties of pure fluorites, which defines the onset of the fastion phase, has been extended to doped fluorites and fastion conductors with different mobile species, structure and symmetry by Ngoepe (1987). This work helped to classify certain fastion conductors whose transition to the fastion state is not accompanied by structural transitions.

The open, fluorite structure in cubic zirconia provides ample space to allow ionic diffusion. The basis for this argument is obtained from observations in other fluorite structured compounds which exhibit high ionic conductivities. However, at the fundamental level, information on the defect structures and transport mechanism giving rise to fastion conduction is limited and presents challenging problems. In the present investigation computer modelling methods will be used to clarify these processes.

Brillouin scattering and refractive index measurements (Botha *et al.* 1993) have presented temperature variations of a complete set of elastic constants in cubic zirconia. In the present investigation different dopant-oxygen vacancy clusters will be investigated to identify the cluster(s) that reproduce(s) the elastic constants from experiment. The relationship between different configurations and the temperature dependence of the elastic constants will also be investigated using the quasi-harmonic approximation. The appropriate cluster(s) will be used as the structural entity on which supercells from MD calculations are prepared.

Computer simulation studies by Dwivedi and Cormack (1990) have shown the power of static lattice methods in predicting defect energies and processes in calcia-stabilised cubic zirconia. These defect calculations will be extended to cubic zirconia doped with both 9.4 mol% Y_2O_3 and 24 mol% Y_2O_3. The calculated defect energies will be compared with those from experiment and also used to clarify the transport phenomenon obtained from molecular dynamics.

Molecular dynamics studies on yttria-stabilised cubic zirconia (Shimojo and Okazaki 1992, Shimojo *et al.* 1992, Li and Hafskjold 1995) were carried out using randomly selected clusters. Our MD calculations will be based on the preferred dopant-oxygen vacancy cluster(s) thus giving the present investigation a unique originality. It is hoped that the transport and structural properties obtained will help to clarify the defect mechanisms as well as ionic conduction processes in doped zirconia.

The presentation in this dissertation has been arranged in the following manner: Chapter 1 introduced the properties of yttria-stabilised cubic zirconia, which is the subject of the present study. General theoretical techniques used to study this material were outlined. Chapter 2 introduces the theoretical background to the main

computer simulation techniques, namely static lattice and molecular dynamics. Results from static lattice simulations and molecular dynamics are presented and discussed in Chapters 3 and 4, respectively. Chapter 5 summarises the main conclusions and advances recommendations for further studies.

CHAPTER 2

THEORETICAL BACKGROUND AND TECHNIQUES

The present chapter deals with static lattice and molecular dynamics simulation techniques, which are the theoretical methods used in the present investigation. Computer simulation techniques are discussed in detail, paying special attention to the theory behind interionic potential model. This model is equivalent to sample preparation in experiment and thus plays a central role in all simulation studies.

2.1 COMPUTER SIMULATION TECHNIQUES

This section gives an indepth discussion of the major computer simulation methods in the present investigation. The section commences with a review of the interionic potential models and parameterisation of the associated potential parameters in the adopted model. This is followed by an outline of the static lattice and molecular dynamics methods, in that order, wherein advantages and limitations of each technique are highlighted.

Simulation is the testing of a model of some real life situation with a view of determining approximately how the real life situation will behave, without going to the trouble and expense of using the real, physical system. Thus, in computer simulation a computational model whose equations encapsulate the behaviour of a physical system are evaluated and the computer is then used to follow the evolution of that model in detail.

Computer simulations are used to predict properties of systems from an

interionic potential model. They are applied in both physical and biological sciences to probe properties of materials under extreme conditions such as high pressure and temperature, shock and radiation, which are difficult or dangerous to perform experimentally. The simulation techniques have been prompted by the latest developments in supercomputers with high speeds and rapid access memory. They have been used to study bulk and surface properties in condensed matter. Two prominent aspects of the theoretical approaches are : (a) *classical methods* and (b) *quantum mechanical calculations* (Hayes and Stoneham 1985, Catlow 1986a, Wimmer 1996, Catlow 1997). The classical methods are based on the interionic potential models for the material and comprise three main categories: (a) *static lattice simulations*, (b) *molecular dynamics* and (c) *Monte Carlo Methods*. Quantum mechanical techniques mainly involve density functional methods and Hartree-Fock approximations and find applications in a wide variety of materials such as semiconductors, ionic crystals, metal alloys, etc.

Classical static lattice simulation and molecular dynamics methods are the major techniques in the present investigation and as such the present chapter discusses these methods in detail. The different categories of simulations are illustrated in figure 2.1.1 while table 2.1.1 presents the analogies that exist between computer simulation and experiment.

Table 2.1.1 Analogies between experiment and computer simulation

Computer simulation	Experiment
Computer model	Sample
Computer program	Apparatus
Program testing	Calibration
Computation	Measurement
Data analysis	Data analysis

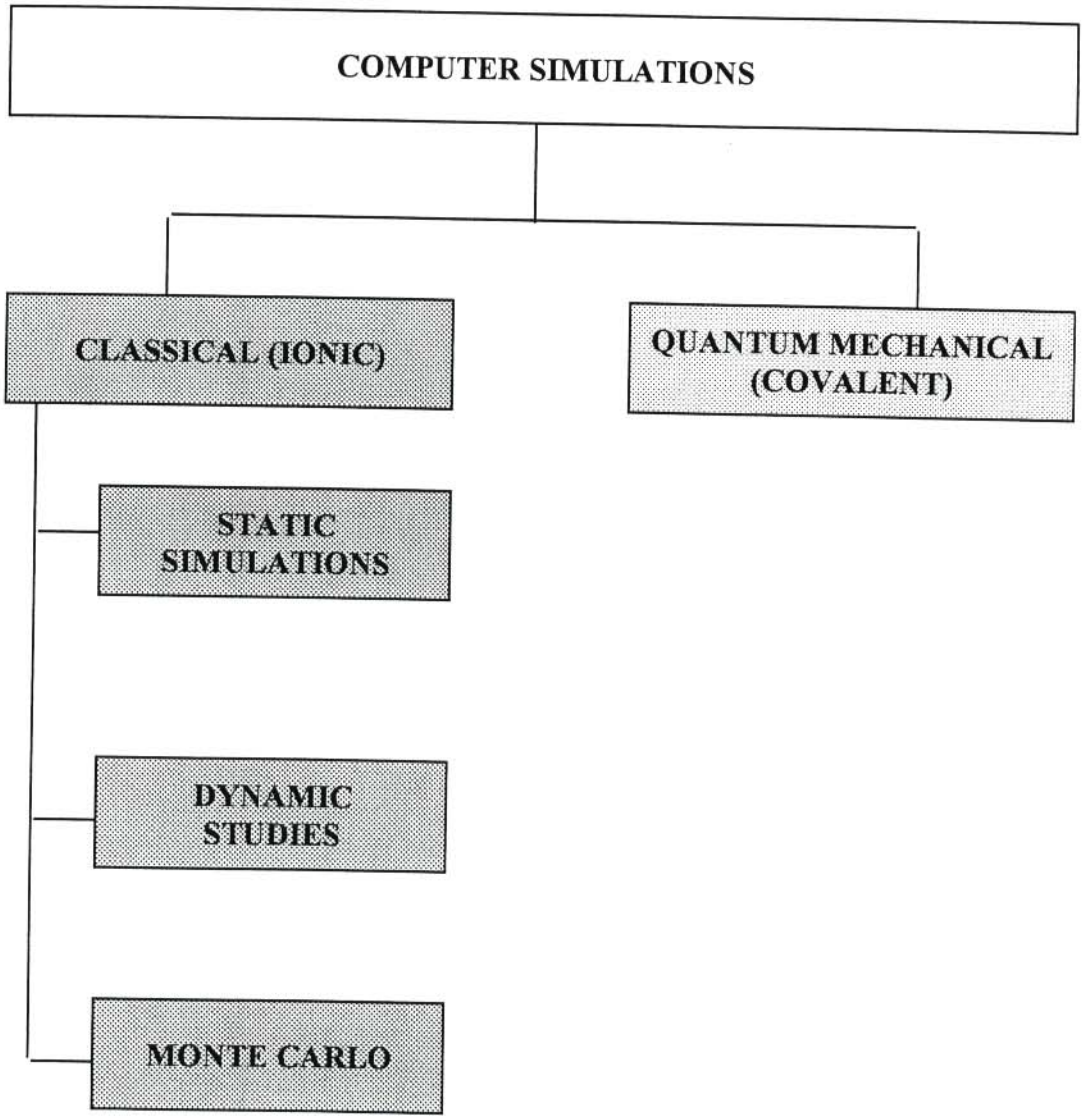

Figure 2.1.1 Different categories of simulation

2.2 INTERIONIC POTENTIAL MODELS

An interionic potential model is a mathematical representation of the potential energy of a system as a function of particle coordinates. The model (a) describes the forces acting between the ions in the solid, (b) helps to determine the reliability of computer modelling studies for the prediction of structural, elastic and dielectric properties, (c) provides a substitute for the explicit solution of the Schrodinger equation and (d) should be accurate, transferable, stable and convenient. As an example a model of pair interaction type is defined by the lattice energy $U_L(r_{ij})$ of an assembly of particles and it is written as

$$U_L(r_{ij}) = \sum_{i>j}' \frac{q_i q_j}{r_{ij}} + \sum_{i>j}' \Phi_{ij} \qquad 2.2.1$$

The various symbols are discussed below. Extensive discussions are given by Catlow and Mackrodt (1982) and Catlow (1997).

2.2.1 *THE LONG RANGE INTERACTIONS*

The first term in equation 2.2.1 represents the long range or Coulomb interactions between point charges q_i and q_j. The sources of the long range interactions are covalence and dispersion and the interactions are best handled via the Ewald summation method (Jackson and Catlow 1988). This method involves the transformation of lattice summations of the coulombic terms from a slowly converging series in real space to a rapidly converging series in reciprocal space.

2.2.2 *THE SHORT RANGE INTERACTIONS*

The second term in equation 2.2.1 represents the short range interactions whose effects come into play when atomic and ionic charges overlap. The

short range interactions with a particular ion are truncated on a sphere centered on the ion and with the radius of the inscribed sphere of the simulation box. This truncation is performed for the simple reason that beyond 10^{-10}m the short range terms are no longer effective. Evidence from quantum mechanical studies suggest that the exponential function is suitable for modelling the short range repulsion between closed shell species. The most common short range interactions are two body and many body interactions.

(a) *Two body interactions*

The interactions may be one of the two types, namely bonded and non-bonded. In the bonded interaction the simplest function applied to a bonding pair of ions is the bond harmonic function

$$\Phi(r_{ij}) = \frac{1}{2} k (r_{ij} - r_0)^2 \qquad 2.2.2.1$$

where r_0 is the equilibrium bond distance and k is the bond force constant. This function is appropriate for $r_{ij} \approx r_0$. The Morse function (Saul *et al.* 1985)

$$\Phi(r_{ij}) = d\left(1 - \exp\left[-\beta (r_{ij} - r_0)\right]\right)^2 \qquad 2.2.2.2$$

is used for larger separations. In equation 2.2.2.2 the quantity d is the dissociation energy of the bond and β is a variable parameter determined from spectroscopic data. The most widely used function for the non-bonded interactions is the Lennard-Jones potential (Allen and Tildesky 1987)

$$\Phi(r_{ij}) = 4\epsilon\left(\left[\frac{\Re}{r_{ij}}\right]^{12} - \left[\frac{\Re}{r_{ij}}\right]^{6}\right) \qquad 2.2.2.3$$

where the steeply repulsive r^{-12} term describes the non-bonded repulsion and the attractive r^{-6} function models the dispersive interaction. The quantity ϵ is the minimum energy of the function with respect to the

infinitely separated atoms and $\Re$ denotes the approximate radius of the atom. This type of function has been used to model rare gas fluids as well as non-bonded interaction in molecular fluids and solids.

An alternative and more popular function is the Buckingham potential (Catlow 1982, 1983) in which the r^{-12} term is replaced by an exponential repulsive term, giving

$$\Phi(r_{ij}) = A_{ij} \exp(-r_{ij} / \rho_{ij}) - C_{ij} r_{ij}^{-6} \qquad 2.2.2.4$$

This is the potential form used in the present investigation. The second term in equation 2.2.2.4 denotes the van der Waal's interactions to which dispersive interactions are added. The van der Waal's interaction is dominant in rare-gas solids and is occasionally important in ionic systems where it may provide attraction between next nearest neighbour ions and always has the the longest range form $- C/r^6$ which is inappropriate at short distances for which it is most important. The dispersive interactions arise from the correlated motions of electrons on different ionic (or molecular) centers. Also, the use of two terms in equation 2.2.2.4 depends on the ranges over which the individual terms are effective.

The cubic fluorite phase of pure zirconia is not stable at low temperatures. This is attributed to the radius of the Zr^{4+} ion being too small for eightfold coordination, resulting in the occurence of low symmetry distortions (Dwivedi and Cormack 1990). In interionic potential terms this means that if the potential is derived by fitting to the fluorite structure, the model will include a large cation radius, thus adversely affecting the calculated properties. Furthermore, that approach assumes that the cubic structure is the equilibrium one, such that calculations performed on the lower symmetry structures will

incorporate a fictitious relaxation energy term since the structure around the defect will try to regain its cubic configuration. This problem was overcome in this work by fitting the rigid-ion potential parameters to a lower symmetry (monoclinic) structure, corresponding to 0 K calculations.

In the present investigation, short range interionic forces were described by the Buckingham potential (equation 2.2.2.4) with the short range parameter C assuming values 0.0 or 27.89. The potential parameters were adjusted via a least-squares fitting routine until the closest agreement between the calculated and experimental quantities has been achieved. Both the high frequency and static dielectric constants were included in the fit, following the suggestion by Catlow (1983). The potential parameters that gave the most reasonable thermodynamic quanties were then used as input in THBREL (Ngoepe et al. 1990, Catlow 1983), CASCADE (Leslie 1982, Leslie and Smith 1989) and FUNGUS (Walker 1982) programs. The short range parameters in both the shell and the rigid-ion models were taken to act between cations and anions as well as between anions and anions, following the studies by Jackson et al. (1986). This is justified given the very large cation-cation separations in yttria-stabilised cubic zirconia (Shimojo *et al.* 1992).

The functions discussed above are simply functions of internuclear distances between pairs of ions and as such have serious shortcomings as increasing evidence suggests that anisotropic terms must be included. This is achieved by taking many body interactions into consideration.

(b) *Many body interactions*

Here the interactions may be one of three forms, namely bond-bending, triple dipole or torsional. The bond-bending interactions are the simplest and has the form

$$\Phi(\theta) = \frac{1}{2} k_B(\theta - \theta_0)^2$$

where k_B is the bond-bending force constant, θ_0 is the equilibrium bond angle and θ is the angle subtended by the central atom in a system of three atoms (Jackson and Catlow 1988). These functions are suitable for covalently bonded systems with O-Si-O bonds. The functions have also enjoyed success when applied in the modelling of force fields for covalently bonded molecules and macromolecules.

We will now discuss the various ways of obtaining the short range potential parameters A, ρ, and C. These parameters may be obtained from one of two main approaches, namely empirical fitting or direct calculation.

(c) *The empirical method*

The empirical method involves the fitting of variable parameters to crystal structure and lattice properties. This involves starting with some initial guess of the parameters followed by a systematic adjustment of the parameters until the differences between the calculated and experimental properties such as elastic constants, dielectric constants, and where possible, phonon dispersion curves, is minimised. The procedure followed in a typical fitting routine using the THBFIT program (Leslie 1982) was extensively discussed by Watson *et al.* (1997). The methodology is summarised below:

A Initial guess of parameters in the specified expression for short-range interactions

B Calculate, at the observed structure :

1. Crystal properties
2. Bulk lattice and internal ion strains

C Minimise

1. Difference between observed and calculated properties
2. Strains

   By adjusting the potential parameters (numerical derivative taken to calculate the magnitude of the adjustment)

D Improved potential mode

E Repeat steps B to D

F Stop at minimum

Note that weights may be applied to observables at stage B.

At the moment, the empirical procedure is the only available approach for determining shell model parameters. The value of the shell model in defect calculations was shown by Dick and Overhauser (1958) . This model is, in essence, a simple mechanical model which couples ionic polarization to the effective overlap forces and describes the harmonic properties of a crystal at small displacements. The procedure normally followed is to:

(a) simulate the outer valence electron cloud by a massless shell of charge Y. Since the shell is massless, it responds instantly and adiabatically to changes in core positions.

(b) simulate the inner electrons and nucleus by a core of charge X. In this way the total charge of the ion is X + Y, which is equal to the oxidation state of the ion. Electrostatically, the core and shell are both

treated as point charges so that relative displacements give a dipole associated with each ion, but no higher multipoles.

(c) assume that the core and shell are joined by a harmonic spring of force constant k.

(d) assume that the mass of the ion is centered at the core and that the short range or overlap forces act through the massless shells. When an electric field, E, is applied to the ion the shell will be displaced from the core and a dipole moment is formed (figure 2.2.2.1).

The interaction between the core and shell is harmonic (since the interionic forces between nearest neighbour shells are harmonic and repulsive) and is given by

$$V_i(r_i) = \frac{1}{2} k_i d_i^2$$

where d_i is the relative core-shell displacement for ion of type i. The free-ion polarizability, α_i, is given by

$$\alpha_i = \frac{Y_i^2}{k_i}$$

The values of the shell charges, spring constant k and the short-range variable parameters A, ρ and C are parameterised by either adjusting the variables until the best possible agreement between the calculated and experimental properties such as dielectric and elastic constants is achieved or by calculation using theoretical methods such as electron gas and ab initio procedures. The shell model was used for the perfect lattice and defect energy calculations reported in Chapter 3.

The empirical method is one of considerable power. However, its range of applications is limited by the fact that it can only be applied to materials for which empirical data is available, although extrapolation procedures may be used in some cases. Secondly, only potentials at internuclear spacings close to those observed in the perfect lattice can be studied. The advantages of this method include the correct reproduction of both the defect energies and the thermodynamic properties of ionic materials. Simulation of fastion conduction in fluorites provides a good example.

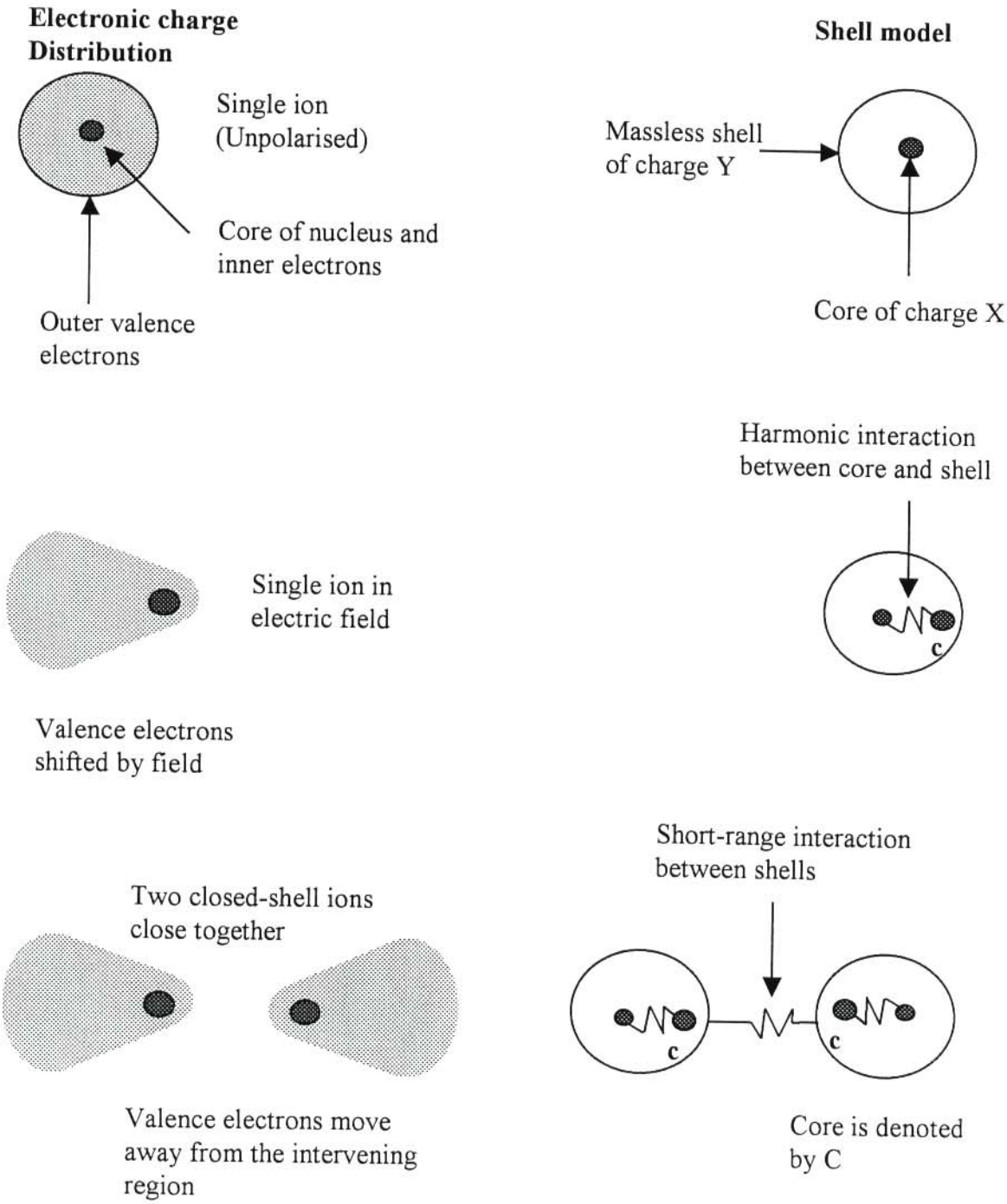

Figure 2.2.2.1 The shell model with short range interactions

2.3 STATIC LATTICE SIMULATIONS

Static lattice calculations involve two aspects, namely (a) perfect lattice calculations and (b) defect energy calculations. This type of simulation does not explicitly include effects of thermal motions of ions in the material and, as such, the method is not able to deal with correlations between diffusing ions. An attempt to include thermal effects is made via the quasi-harmonic approximation, discussed in section 2.3.1.

2.3.1 PERFECT LATTICE SIMULATIONS

Perfect lattice simulations involve the specification of a unit cell structure, which is then repeated infinitely in space in order to generate an infinite periodic system. In modern work, the unit cell may be very large and complex, containing several hundred atoms. Static calculations on perfect structures have three main components (Catlow 1990 and Watson 1997):

(a) *Lattice summations*

The lattice summations of the Coulombic term are slowly converging owing to the r^{-1} dependence of the electrostatic interactions. They must be taken to infinity and not truncated. This is easily achieved by using the Ewald procedure. The lattice summations of the short range terms are handled in real space as they may be safely truncated beyond a cutoff distance.

(b) *First and second order derivatives of the lattice energy*

The lattice energy is the binding or cohesive energy of a perfect crystal per unit cell or per formula unit. It plays a crucial role in treating properties of solids as well as in assessing the relative stabilities of different structures.

Moreover, its derivatives with respect to elastic strain and displacement are related to elastic and dielectric constants. The dielectric constants reflect the response of the solid to an electric field. The high frequency (optical) constant ϵ_∞ gives the response of the electrons alone whilst the static dielectric constant ϵ_0 involves the balance between the direct force of the applied field, the interionic forces and the induced polarisation.

Elastic constants are particularly important as they provide fundamental information concerning the interionic forces in solids. Furthermore, they are a measure of the energy change when a solid is strained uniformly and are related to lattice vibrations and originate from long wavelength acoustic modes associated with relative motion of unit cells. The elastic constants are derived from the lattice energy using a procedure outlined next. Suppose a lattice is near its equilibrium configuration and contains n atoms per unit cell. Using the formalism of Born and Huang (1954) the lattice energy is expressed to second order in the total strain as

$$U_L(\mathbf{R}) = U_L(\mathbf{R}) + \mathbf{g}^T \cdot \delta + \delta^T \cdot \mathbf{W} \cdot \delta \qquad 2.3.1.1$$

where δ denotes the generalised (3n + 6)-dimensional strain vector comprising of 3n internal components, $\delta\mathbf{r}$, and six bulk components, $\delta\epsilon$, such that

$$\sigma = [\delta\mathbf{r}, \delta\epsilon]$$

$\mathbf{g}$ is a vector of first derivatives of the energy

$$\mathbf{g} = \left[\partial U_L / \partial \mathbf{r}, \quad \partial U_L / \partial \epsilon\right] \qquad 2.3.1.2$$

and $\mathbf{W}$ is the corresponding matrix of second derivatives

$$\mathbf{W} = \begin{bmatrix} \partial^2 U_L / \partial\mathbf{r}\partial\mathbf{r} & \partial^2 U_L / \partial\mathbf{r}\partial\epsilon \\ \partial^2 U_L / \partial\epsilon\partial\mathbf{r} & \partial^2 U_L / \partial\epsilon\partial\epsilon \end{bmatrix} \qquad 2.3.1.3$$

$$= \begin{bmatrix} \mathbf{W}_{rr} & \mathbf{W}_{r\epsilon} \\ \mathbf{W}_{\epsilon r} & \mathbf{W}_{\epsilon\epsilon} \end{bmatrix}$$

The configuration, $\mathbf{R}' \equiv \{\mathbf{r}_n\}$ is related to $\mathbf{R}$ via the transformation

$$\mathbf{r}_n = \Delta\epsilon \cdot (\mathbf{r}_n + \mathbf{r}_n)$$

in which $\Delta\epsilon$ denotes the symmetric strain matrix formed from the components of

$$\Delta\epsilon = \begin{bmatrix} \delta\epsilon_1 & \frac{1}{2}\delta\epsilon_6 & \frac{1}{2}\delta\epsilon_5 \\ \frac{1}{2}\delta\epsilon_6 & \delta\epsilon_2 & \frac{1}{2}\delta\epsilon_4 \\ \frac{1}{2}\delta\epsilon_5 & \frac{1}{2}\epsilon_4 & \delta\epsilon_3 \end{bmatrix}$$

The various derivatives in equation 2.3.1.3 can be evaluated using an appropriate form of pair potential. In the absence of external fields, application of the equilibrium conditions $\mathbf{g} = 0$, for lattices without permanent moments, and $\partial U_L/\partial \mathbf{r} = 0$ to equation 2.3.1.1 yields

$$U_L(\mathbf{R}) = U_L(\mathbf{R}_e) + \frac{1}{2}\delta\epsilon \cdot \left[\mathbf{W}_{\epsilon\epsilon} - \mathbf{W}_{\epsilon r} \cdot \mathbf{W}_{rr}^{-1} \cdot \mathbf{W}_{r\epsilon}\right] \cdot \delta\epsilon \qquad 2.3.1.4$$

where R_e denotes the field-free equilibrium configuration. Elastic constants are defined as the second derivatives of the lattice energy with respect to strain, with the lattice energy normalised to unit volume. From equation 2.3.1.4 the elastic constants tensor, C, is given by

$$\mathbf{C} = \left(\frac{1}{V_c}\right)\left[\mathbf{W}_{\epsilon\epsilon} - \mathbf{W}_{\epsilon r} \cdot \mathbf{W}_{rr}^{-1} \cdot \mathbf{W}_{r\epsilon}\right]$$

These basic principles are incorporated into the computer programs PLUTO and THBREL. The latter was used to calculate the thermodynamic properties reported in the present investigation.

The variation of elastic constants with temperature is related to the

anharmonic nature of lattice vibrations (Stern 1958, Born and Huang 1954). One measure of this anharmonicity is the asymmetry of the lattice potential energy. The asymmetry is related to the higher order elastic constants and as such, the temperature dependences of the second order elastic constants depend on the second, third and fourth order elastic constants (Garber and Granato 1975, Born and Huang 1954, Stern 1958, Mitskevich 1963, Hiki *et al.* 1967, Cowley and Cowley 1965). According to the harmonic approximation the internal energy of a system of N particles is given by

$$U = \phi_0 + \sum_{i=1}^{3N}{}' (n_i + \frac{1}{2})\hbar\omega_i$$

where ϕ_0 and n_i denote the potential energy of the particles in their mean positions and the average number of phonons with frequency ω_i at temperature T, respectively. The quasi-harmonic approximation is satisfied when ϕ_0 and ω_i, and their strain derivatives, depend indirectly on temperature through the temperature dependence of the lattice parameter. The adiabatic and isothermal second order elastic constants are given by

$C_{ijklmnp} = \rho_0 \left(\partial^4 U / \partial\eta_{ij}\,\partial\eta_{kl}\,\partial\eta_{mn}\,\partial\eta_{op}\right)_s$ and

$C^T_{ijkl} = \rho_0 \left(\dfrac{\partial^2 F}{\partial\eta_{ij}\,\partial\eta_{kl}}\right)_T$, respectively, where ρ_0, F and η_{ij} denote the density of the system in the initial configuration, the Helmholtz free energy and the Lagrangian strain parameter (Brugger 1964), respectively. Differentiating with respect to strain and temperature yields

$$\left(\frac{\partial C_{ijkl}}{\partial T}\right) = -k_B\rho_0 \sum_{x=1}^{3N}{}' \left(\frac{\partial \gamma_x^{ij}}{\partial\eta_{kl}}\right)_T \qquad 2.3.1.5$$

Substitution of the Gruneisen parameter $\gamma_{ij} = -\dfrac{1}{2\omega_i}\left(\dfrac{\partial\omega_x}{\partial\eta_{ij}}\right)_{T,\eta=0}$

into equation 2.3.1.5 yields

$$\left(\frac{\partial C_{ijkl}}{\partial T}\right) = -k_B \rho_o \sum_{x=1}^{3N} \left[2\gamma_x^{ij}\gamma_x^{kl} - \frac{1}{2\omega_x}\left(C^{TT}_{ijklmr} + C^{STT}_{ijklmrsv} u_s u_r + 2C^{ST}_{klmrsj} u_s u_i + 2C^{ST}_{ijmrsl} u_s u_k \right) N_m N_r \right] \qquad 2.3.1.6$$

where only temperature independent terms appear on the right hand side. The expression above can be expanded for different elastic constants for cubic and all other symmetries. The derivatives in equation 2.3.1.6 are evaluated at the initial configuration and using Voight notation, C_{1111} becomes C_{11}, C_{1122} becomes C_{12} and C_{2323} becomes C_{44}. All other elastic constants are zero or equal to one of the preceeding three, for crystals with a cubic symmetry, as shown below

$$\begin{vmatrix} C_{11} & C_{12} & C_{12} & 0 & 0 & 0 \\ C_{12} & C_{11} & C_{12} & 0 & 0 & 0 \\ C_{12} & C_{12} & C_{11} & 0 & 0 & 0 \\ 0 & 0 & 0 & C_{44} & 0 & 0 \\ 0 & 0 & 0 & 0 & C_{44} & 0 \\ 0 & 0 & 0 & 0 & 0 & C44 \end{vmatrix}$$

The linear temperature variation of the elastic constants in yttria-stabilised cubic zirconia below the fastion transition temperature will be explained in terms of this theory in Chapter 3.

(c) *Energy minimization (E.M.)*

In energy minimization techniques the cell volume and coordinate positions are adjusted, using an iterative computational method, until the minimum energy configuration is attained and the net pressure or strain (stress) is zero. The

state of minimum energy is an equilibrium one and all thermodynamic quantities are calculated when this state has been attained. The pressure is given by the derivative of the free energy with the bulk property, such as thermal expansion coefficient. Thus, it is possible to deduce the elastic constants at various temperatures from the determined expansion coefficients. Energy minimisation techniques are restricted to the prediction of static structures and to those properties which can be described within a harmonic or quasi-harmonic dynamical approximation in which there is no explicit inclusion of atomic motions (Catlow 1990).

The choice of the computational minimisation technique is very important. There are several approaches, mainly in three classes: (a) direct searches, (b) conjugate gradients methods and (c) Newton-Raphson procedures. Direct searches are the simplest methods and use the energy function alone and searches over the whole configuration space until the minimum is located. This method is suitable only for very simple systems with few variables. Much greater efficiency is achieved from the gradient methods in which the derivatives $\frac{\partial U}{\partial x_i}$ with respect to all the structural variables, x_i, are determined. These then guide the direction of minimisation. Much more rapid convergence can be obtained by using the Newton-Raphson methods in which the second derivatives of the energy function are used to guide the minimisation direction. Here the $(j+1)^{th}$ set of coordinates is obtained from the j^{th} set by the relationship

$$x_{j+1} = x_j + \mathbf{W}_j^{-1} \cdot \mathbf{g}_j$$

where $\mathbf{g}$ and $\mathbf{W}$ are defined in equations 2.3.1.2 and 2.3.1.3, respectively. Though these methods are far more rapidly convergent than

gradient procedures, the improved convergence may be lost in the extra computational effort required to store the Hessian matrix $\mathbf{W}^{-1}$. In that case, the simpler conjugate gradient methods, which involve storage of the first derivative of the energy function only are used (Catlow 1983).

2.3.2 CALCULATION OF DEFECT ENERGIES

The aim of computer simulation studies of defects in solids is threefold: Firstly, it is to comprehend the structures and energies of defects and their aggregates, their diffusion mechanism and how they get trapped. Secondly, it is to study the effect of defects on the host crystal and lastly, it is to understand the effect of changes in the host crystal on the defects. Most calculations involve three ingredients: (a) an ionic model (b) an interionic potential model and (c) an efficient computer code and algorithm. The ionic model is usually the shell model, which avoids the instabilities found with simpler models of polarizable point ions. There are basically two methods used for calculating defect energies. These are the two region strategy and the supercell procedure.

2.3.2.1 *THE TWO REGION STRATEGY*

The central problem in static lattice defect energy calculations involves the treatment of the lattice relaxation around the defect. This is particularly crucial for ionic and semi-ionic solids because defects in these solids are generally charged species, owing to the long range of the coulomb forces which lead to a long range relaxation field (Norgett and Lidiard 1972, Catlow and Mackrodt 1982).

There are two important technical features in the calculation of defect

energies. The first point concerns the handling of the host lattice ions far from the defect while the second concerns numerical methods. Three main methods are used in the former case: Firstly, rigid boundary conditions are applied in which ions outside a given region are assumed immobile and unpolarisable. A variant uses a crystallite with a free surface. Secondly, periodic boundary conditions are applied to a regular array of defects. The lattice then consists of large supercells, each containing one defect. Lastly, the Mott-Littleton approximation is used (Mott and Littleton 1938). The two region strategy was used for the defect energy calculations reported in Chapter 3 and, in essence, it involves the division of the lattice surrounding the defect into two regions I and II as shown in figure 2.3.2.1.1.

Region I surrounds the defect and contains generally between 100 and 300 particles. This region is treated atomistically and since the forces exerted by the defect on the surrounding are strong, the relaxation of this region is best handled by the energy minimisation technique. In contrast, for the more distant, weak-field regions, the defect forces are relatively weak and as such lattice relaxation may be treated by more approximate methods. Note that in polar crystals, region II must extend to infinity owing to the long range of the coulomb forces exerted by the effective charge of the defect.

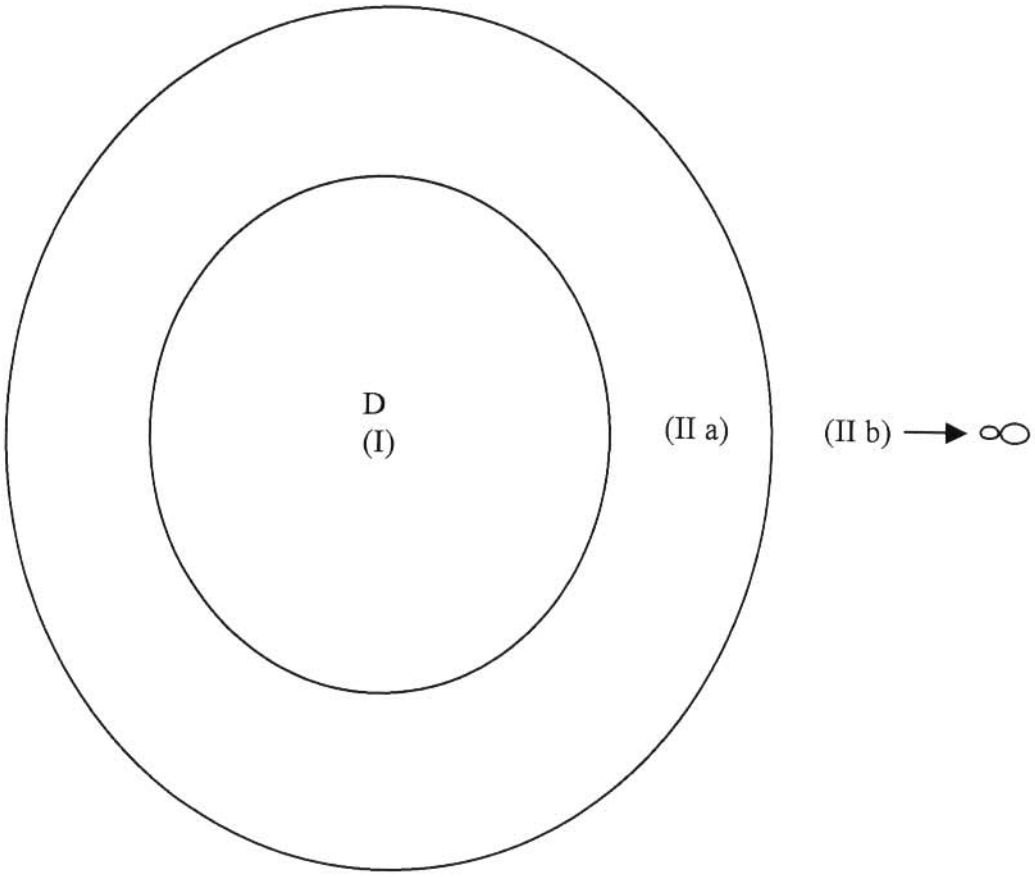

Figure 2.3.2.1.1 The two region strategy for defect calculations. "D" indicates a defect. Note that region IIb extends to infinity

The commonest treatment is based on the Mott-Littleton approximation, which is appropriate for ionic crystals. For dielectrically isotropic materials, the polarisation $\mathbf{P}(\mathbf{r})$, at a point $\mathbf{r}$ from the defect of charge q, is given by

$$\mathbf{P}(r) = \frac{q\mathbf{r}}{r^3}\left(1 - \frac{1}{\epsilon_0}\right) \qquad 2.3.2.1.1$$

where ϵ_0 is the static dielectric constant of the crystal.

Equation 2.3.2.1.1 applies strictly to cubic crystals. For non-cubic materials, more complex expressions are used as discussed by Catlow *et al.* (1982) and Catlow and Mackrodt (1982). Within the two-region approximation the defect formation energy, E_D, may be written as

$$E_D = E_I(\mathbf{x}) + E_{I,II}(\mathbf{x}, \mathbf{y}) + E_{II}(\mathbf{y}) \qquad 2.3.2.1.2$$

where E_I denotes the energy arising solely from the interaction of particles in region I, which is treated in terms of discrete ions with shell or core displacements $\mathbf{x}$; E_{II} is the self energy of region II for which $\mathbf{y}$ is the vector of coordinate displacements and $E_{I,II}$ represents the energy arising from the interaction between regions I and II. In order to avoid consideration of all ion-ion interactions in region II, (a) E_{II} is assumed to be a quadratic, i.e. harmonic function, according to

$$E_{II} = \frac{1}{2}\mathbf{y}.\underline{\underline{A}}.\mathbf{y} \qquad 2.3.2.1.3$$

where $\underline{\underline{A}}$ is a force constant matrix and (b) region II is taken to be in equilibrium under the forces exerted on it by region I. Differentiating E_D with respect to $\mathbf{y}$, and applying the equilibrium condition to region II, it follows that

$$\left(\frac{\partial E_D}{\partial y}\right)_{y=\mathbf{y}} = \left(\frac{\partial E_{I,II}(\mathbf{x},\mathbf{y})}{\partial y}\right)_{y=\mathbf{y}} + \left(\frac{\partial E_{II}(\mathbf{y})}{\partial y}\right)_{y=\mathbf{y}}$$

$$= \left(\frac{\partial E_{I,II}(\mathbf{x},\mathbf{y})}{\partial y}\right)_{y=\mathbf{y}} + \frac{1}{2}\frac{\partial}{\partial y}\mathbf{y}.\underline{\underline{A}}.\mathbf{y}$$

$$= \left(\frac{\partial \underline{E}_{I,II}(\mathbf{x}, \mathbf{y})}{\partial y}\right)_{y=\mathbf{y}} + \underline{\underline{A}}.y$$

$$= 0$$

so that

$$\left[\frac{\partial \underline{E}_{I,II}(\mathbf{x}, \mathbf{y})}{\partial y}\right]_{y=\mathbf{y}} = -\underline{\underline{A}}.y \qquad 2.3.2.1.4$$

Substitution of 2.3.2.1.4 and 2.3.2.1.2 into 2.3.2.1.3 yields

$$E_D = E_I(\mathbf{x}) + E_{I,II}(\mathbf{x},\mathbf{y}) - \frac{1}{2}\mathbf{y}\left[\frac{\partial \underline{E}_{I,II}(\mathbf{x},\mathbf{y})}{\partial y}\right]_{y=\mathbf{y}}$$

thereby removing the explicit dependence of E_D on E_{II}, which is convenient.

Defect calculations therefore consist of the relaxation of region I, followed by the evaluation $E_I(\mathbf{x})$ by direct summation and then $E_{I,II}(\mathbf{x},\mathbf{y})$ and its derivative. For the latter, region II is subdivided into an inner, interface region IIa and an outer region IIb. Region IIa surrounds region I and its displacements are calculated by the Mott-Littleton procedure as the sum of the response from all the charged components at the defect in region I. This is followed by direct summation of the interactions between regions I and II and the determination of their derivatives. The use of the interface, region IIa, is found to be necessary in obtaining accurate results with inner regions of a modest size. For the remainder of region II, region IIb - regarded as a dielectric continuum, the interaction is treated as arising solely from the net effective charge of the defect in region I (Norgett 1974, Catlow *et al.* 1982, Catlow and Makrodt 1982), and the appropriate summations may be evaluated analytically.

2.3.2.2 *SUPERCELL PROCEDURES*

The two region strategy bases its approach on embedding the defect in an

infinite and otherwise perfect crystal. An alternative approach is to set up a defect supercell. A supercell is made up of a number of basic unit cells and must include the surrounding lattice. After introducing the defect in the structure, the defect, as well as the surrounding region of the lattice, are repeated infinitely in space. Supercells of different sizes may be constructed by appropriate choices of lattice vectors. Perfect lattice calculations are then carried out on the resulting structure via energy minimisation techniques. Of particular importance is that the results obtained from this routine converges to those obtained from the two region strategy as the size of the supercell increases. An example of application of supercell methods to tysonite structured LaF_3 is given by Ngoepe *et al.* (1990).

The supercell procedure looks at the impact of defects on the properties of materials such as elastic and dielectric constants. Moreover, the method provides additional information to that obtained from calculations performed on isolated defects because it yields energies of interaction between defects. The disadvantages of the methods include the use of both smaller region I sizes and periodic boundary conditions. The choice of a unit cell and the subsequent specification of a supercell structure is illustrated in figure 2.3.2.2.1.

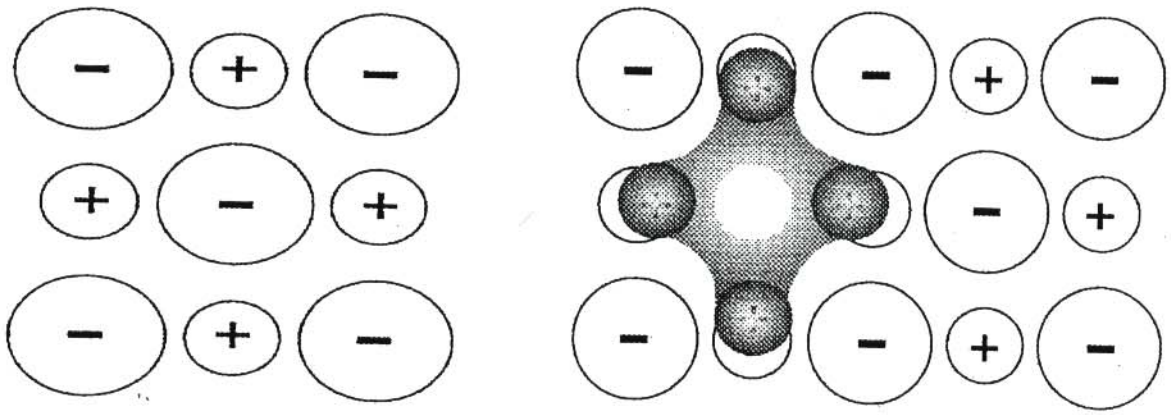

Figure 2.3.2.2.1 The choice of a unit cell and the subsequent specification of the supercell structure

Finally, static lattice simulation methods are limited in that it is not trivial to predict free energies of defects. These methods usually concentrate on internal energies and generalisations to give free energies is not always easy. Secondly, specific defect processes have to be postulated for assessment and although many processes can be tried, one always wonders if a critical process has been left out.

2.4 MOLECULAR DYNAMICS SIMULATIONS

Molecular dynamics (MD) simulation, developed by Alder and Wainwright (1959) and extensively utilised by Jacobs and Rycerz (1997), explicitly includes thermal effects by solving the reversible equations of motion of a dynamical ensemble of particles representing the system. Thus, MD is able to simulate correlations between diffusing atoms, which is not possible with static lattice simulation techniques.

In its original form, MD simulation was carried out under constant particle number, volume and energy, i.e. NVE simulation. However, the more recently developed techniques allow one to work at constant pressure, temperature and number of particles in which dynamic changes in both the lattice vector and the angles occur with time (Parrinello and Rahman 1981). In the present research endeavour NPT simulation was performed by combining the constant pressure method proposed by Andersen (1980) with the constant temperature procedure proposed by Nosi (1984). A variety of statistical ensembles are used in most MD and Monte Carlo simulation techniques. In the microcanonical ensemble NVE simulation is carried out. The canonical ensemble has N, V, and T as constant parameters and the NPT simulation uses the isothermal-isobaric ensemble. Furthermore, in the grand canonical, μVT, ensemble the number of particles is allowed to vary in order to achieve a constant chemical potential μ.

2.4.1 MODELING AND APPROXIMATIONS

In a molecular dynamics simulation one starts by specifying a simulation box comprising a regular array of atoms, molecules or ions arranged and located at lattice sites. This simulation box is usually a cubic supercell. However, the

cubic nature of the box introduces anisotropy since there would be more particles along the cube's body diagonals than elsewhere. This anisotropy may be reduced by enclosing the particles in a more complicated Wigner-Seitz, spherical, type of box. Its advantage is that for a given number of particles and number density, valid correlations are obtained over a greater range of ionic separations. The latter set-up poses several problems, particularly in the indexing of particles as they pass through the walls of the box and in the summations over image particles. Despite its shortcomings, however, the cubic box is commonly used.

A typical classical molecular dynamics sample contains up to ten thousand particles which must necessarily be conserved both inside the system and equivalent surroundings. The number of particles is conserved by creating outside the simulation box, some images of the particles enclosed in the box. This is accomplished by introducing periodic boundary conditions (explicitly assumed) which ensure that when a particle leaves the box on one side, its image from a neighbouring box enters the box on the opposite side (see figure 2.4.1.1).

The periodic boundary conditions give rise to an infinite system without surfaces and as such, Schottky defects cannot be simulated unless vacancies are artificially introduced at the beginning of the simulation. Periodic boundary conditions preserve the shape of the simulation box and hence are appropriate for simulation runs at constant volume.

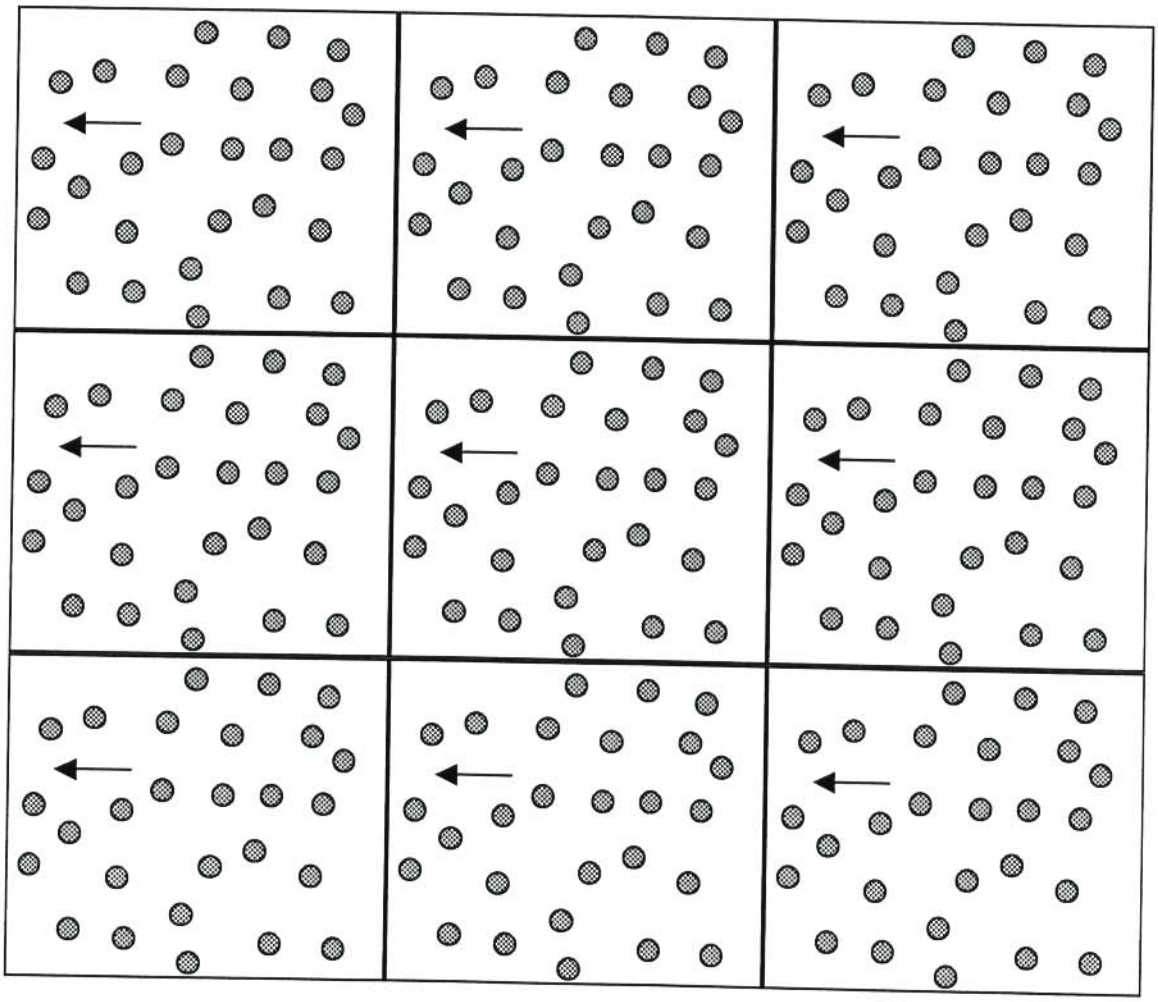

Figure 2.4.1.1 An illustration of periodically repeated ensemble of particles. The arrows below one of the particles indicate that the particle is leaving the box, while its image in an adjacent box enters

However, Parinello and Rahman (1980, 1981) have developed a method which allows the shape of the simulation box to vary under constant pressure conditions. The next step is the assignment of positions, x_i, and velocities $\mathbf{v}_i$ in line with a target temperature, T. Various initial conditions have been used, however, in most cases the particles are given equal kinetic energies with a random selection of the three direction cosines of the velocity and initial positions corresponding to a face-centered cubic lattice. The adopted interionic potentials are then used to calculate the total force **F** acting on each particle. The force acting on the i^{th} particle is given by

$$F_i = \sum_j [- q_i q_j / r_{ij}^2 - A_{ij}/\rho_{ij} \exp (- r_{ij}/\rho_{ij}) - C_{ij}/r_{ij}^6]$$

where the point charges q_i and q_j are separated by a distance r_{ij}. The movement of the particles is described by Newton's equations of motion

$$\frac{d\mathbf{r}_i}{dt} = \frac{\mathbf{p}_i}{m_i} \qquad 2.4.1.1$$

$$\frac{d\mathbf{p}_i}{dt} = \mathbf{F}_i \qquad 2.4.1.2$$

A time step, Δt, is specified. The choice of Δt is very critical. If it is too large, lattice vibrations can occur within the time step leading to gross errors. If it is too small, the simulation will exceed the computer time available. The time step must be shorter than the time scale of any important process in the system such as the period of atomic vibration. Usually Δt lies between 10^{-14} and 10^{-15} seconds. The calculation of the forces takes more than 90% of the total CPU time, with most of the time spend in replacing the continuous differential equations 2.4.1.1 and 2.4.1.2 with discrete, finite difference one-step equations. There are a number of ways in which these equations can be approximated by discrete analogs (Berendsen 1986). In particular, the coordinates and velocities are updated using a simple procedure

based on Newton's equation of motion. The simplest zero order version of this equation is given by

$$x_i' = x_i + v_i \Delta t$$
$$\mathbf{v}_i' = \mathbf{v}_i + \frac{F_i}{m_i} \Delta t$$

where the primes indicate values of x_i and $\mathbf{v}_i$ after time Δt and m_i denotes the mass of particle i. A number of sophisticated updating algorithms that minimise the accumulation of errors on repeated updating due to the finite size of Δt are available. The Beeman (Beeman 1976) algorithm is more popular and has been incorporated into solid-state simulation code by Walker (1982). It is of the form

$$x_i(t + \Delta t) = x_i(t) + v_i(t)\Delta t + [4F_i(t) - F_i(t - \Delta t)] (\Delta t)^2 / (6m_i)$$
$$v_i(t + \Delta t) = v_i(t) \left[4F_i(t + \Delta t) + 10F_i(t) - 2F_i(t - \Delta t)\right] \Delta t/ (12m_i).$$

for an infinitesimally small time-step. The leap-frog algorithm (Hockey 1970) has the form

$$x_i(t + \Delta t) = x_i(t) + v_i\left(t + \frac{\Delta t}{2}\right)t$$
$$v_i(t + \Delta t) = v_i\left(t - \frac{\Delta t}{2}\right) + F_i(t)\Delta t/m_i$$

whereas the Verlet's (Verlet 1967) algorithm has the form

$$x_i(t + \Delta t) = - x_i(t - \Delta t) + 2x_i(t) + F_i(t)(\Delta t)^2/m_i$$
$$v_i(t) = [x_i(t + \Delta t) - x_i(t - \Delta t)] / (2\Delta t)$$

The updating procedure is repeated several thousand times, thus permitting the study of the time evolution of the system. The system is then allowed to settle into equilibrium, which is indicated by a constant temperature. In the equilibration period the ensemble attains equipartition between kinetic and potential energy as well as a thermalised distribution of velocities. After equilibrium the coordinates and velocities of successive time steps are stored and analysed for properties of interest. The analysis will include the

determination of radial distribution functions, diffusion coefficients and a range of correlation functions including the velocity auto-correlation and the van Hove correlation functions.

Molecular dynamics is one of considerable power in the study of the dynamics of condensed matter as it yields detailed dynamical information and includes time as a parameter in the simulation. However, MD is severely limited :

(a) The short time scale of the simulations, typically 10 - 100 ps, restricts the study of fastion conductors since it would not normally be possible to observe a sufficient number of atomic migration events within this time period.

(b) The size of the simulation box raises the second difficulty. The number of mobile species must be very large. Consequently, full unrestricted applications are confined to the study of fastion conductors. Restricted application to non-fastion conductors have been reported by Jacobs and Moscinski (1985) and Gillan and Harding (1986).

(c) The use of periodic boundary conditions.

(d) The inclusion of ionic polarisabiliy is very taxing in CPU time because the electron distribution responds to changes in nuclear positions instantaneously. Hence for each time-step the ionic dipole moments have to be calculated through time-consuming iterative processes. The time factor is further exacerbated by an increased number of species in the simulation. However, it is possible to perform MD calculations using the shell model (Lindan and Gillan 1994)

(e) Only rapid diffusion with diffusion coefficients greater than 10^{-7} cm^2/s may be simulated since the number of atomic displacements is insufficient for slower diffusions in ordinary conductors.

(f) Simulation has to be run at several temperatures in order to extract Arrhenius energies, which is a costly process. And once calculated the Arrhenius energies cannot be easily decomposed into defect formation and migration energy terms. This is naturally and simply achieved in static lattice simulation procedures.

(g) The choice of an interionic potential is normally more restrictive than in energy minisation techniques.

Despite these limitations, MD techniques are widely used and may now be routinely employed in both microcanonical and NPT ensembles. The major advantages include direct provision of the rates of processes, treatment of the liquid state, or other highly defective states with transient defects, or non-equilibrium processes following a sudden perturbation, on exactly the same basis as the solid and the automatic detection of any process occuring with reasonable probability so that the user need not find the right mechanism in advance.

2.4.2 CALCULATION OF PROPERTIES OF INTEREST

In this section the formalism for the calculation of physical and thermodynamic properties such as tracer diffusion constant, radial distribution functions and specific heat will be discussed.

(a) *Tracer diffusion constant*, D_i

The calculation of the tracer diffusion coefficient is particularly straightforward and relies on the outcome of random walk theory (Catlow 1990). The determination of the diffusion constant is crucial because it gives an indication about the rate of diffusion. A particular ion i is chosen from the

mobile sublattice and its position, $r(t_1)$, at time t_1 is noted. A new position, $r(t + t_1)$, after time t is determined, followed by the calculation of $r_i(t)^2 = |r(t + t_1) - r(t_1)|^2$. This procedure is repeated several times but always keeping the same time difference t. The process is then repeated for all ions of the same type. Thereafter, the mean-square displacement $<\Delta r_i(t)^2>$ is determined from the large sample of values of $\Delta r_i(t)^2$. The diffusion constant is obtained directly from the graph of $<\Delta r_i(t)^2>$ versus time in line with $<\Delta r_i(t)^2> = 6D_i|t| + B_i$. The constant B_i is a Debye-Waller factor denoting a thermal factor arising from atomic vibrations and as such, it is related to the mean amplitude of a particle's vibrational motion.

(b) *Self correlation functions*

The mean-square displacement shows the rate of diffusion and little else. Self-correlation functions, on the other hand, provide a means of capturing the diffusion process by giving full probability distributions of the displacements. Three types of self correlation functions are (a) radial distribution function (RDF), (b) Van Hove self-correlation function and (c) velocity auto-correlation function (VAF). The radial correlation function, $g_{ij}(r)$, is the simplest positional correlation function and it gives the probability of finding a particle of type j at a distance r from a particle of type i situated at the origin, O. This function is of particular importance in the study of fastion conductors since it contains information about the structure and interparticle correlations of materials. Furthermore, it gives a measure of long range order in solids. In the present investigation, structural information in yttria-stabilised cubic zirconia is obtained from RDFs and discussed in Chapter 4. The Van Hove self-correlation function $G_i^s(\mathbf{r}, t)$ gives the probability of a particle of type i,

at position vector $\mathbf{r} = 0$ at time $t = 0$, moving to another point $\mathbf{r}$ at time t. Hansen and MacDonald (1976) have shown that the structure of $G_i^S(\mathbf{r}, t)$ gives information about the nature of ionic transport in a material. A Gaussian function indicates a continuous liquid-like migration process whilst a non-Gaussian function shows a hopping migration mechanism. Lastly, VAF gives an ensemble average of the projection of the velocity vector of a particle along its velocity vector at an earlier time t. Details are available from Ladd (1990)

(c) *Ion trajectories and migration mechanisms*

The raw output from molecular dynamics simulation is a voluminous and incomprehensible record of particle coordinates. The best way of making this mass of numbers meaningful is to turn it into pictures. This is accomplished by plotting ion trajectories. The trajectories play a crucial role in ion migration mechanisms as they give an indication of the type of migration process, either vacancy or intertitial, and also illustrates the presence or absence of correlated motion in the system. Vacancy mechanism occurs when the mobile ions move along the $<100>$ directions while interstitial migration mechanisms are along the $<111>$ directions in a fluorite structure formed by yttria-stabilised cubic zirconia.

2.5 SIMULATION CODES

Computer simulation codes used in the present study for static lattice simulation are (a) CASCADE (Leslie and Smith 1989) (b) THBREL, closely related to the PLUTO program (Catlow and Norgett 1978) and (c) THBFIT (Leslie 1982, Watson *et al.* 1997). The computer programs were obtained from Daresbury Laboratory.

(a) *CASCADE (Cray Automatic System for the Calculation of Defect Energies)*

The CASCADE code was used for the defect energy calculations reported in this work. CASCADE was written by Leslie and Smith at Daresbury Laboratory and combines defect and perfect lattice calculations. Although the program was initially adapted to exploit the parallel processor of the CRAY series computers, it was possible to commission the program to run on the VAX mainframe. In a typical calculation, data describing the unit cell and defect are first read in. This is followed by the determination of the point group symmetry about a user defined origin. Ion-ion potentials, which model the crystal structure and the interaction of any foreign ion with it, are read in. This potential is then used to model the perfect, non-defective lattice. Next, strains in the unit cell, elastic constants, dielectric constants as well as the response of the ions to an electric field are calculated. Two spherical regions, regions I and IIa (relaxed using the Mott-Littleton procedure) are defined, followed by the relaxation of the defect structure using the adopted potential.

The calculation of gradients of the defect energy is the most expensive part in terms of computer time because they are calculated at every iteration of the defect energy minimisation. Fortunately, the E.M. procedure uses a Hessian update algorithm so that the second derivative matrix need only be calculated and inverted once. Another taxive step in terms of time is the perfect lattice relaxation option, which in any case is only suitable for small unit cells close to equilibrium. A more detailed discussion is found in Leslie and Smith (1989).

(b) *THBREL*

The THBREL code works in the same way as CASCADE except that in this case defect energies are not calculated. The code is used for perfect lattice calculations and as such yields values for elastic constants, as well as both high and low frequency dielectric constants.

(c) *THBFIT*

The THBFIT code is very much similar to THBREL. The only difference is the use of the FITE directive in THBFIT to indicate that empirical fitting procedures will be carried out.

(d) FUNGUS

This is a general purpose molecular dynamics program that may be applied to crystals of any symmetry, and it incorporates the Ewald procedure for electrostatic summations and the equipartition of kinetic and potential energies (Walker 1982). The periodic boundary conditions are always explicitly implied and the program uses the Born-Mayer form (equation 2.2.2.4) for the short range potentials in the evaluation of the Madelung sums. Its special advantage is that the entire package may be controlled from one driver routine, allowing a great deal of flexibility to the parameters used in the simulations while modifications can be made with the minimum of difficulty.

CHAPTER 3

STATIC LATTICE CALCULATIONS

In this chapter results from ZrO_2(x mol% Y_2O_3), with x = 9.4, 15, 21 and 24, and obtained from static lattice calculations are presented. Two sets of results are reported. First, the formation, migration and activation energies are presented, followed by results of defect associates. These associates are believed to be responsible for the observed ageing phenomenon in stabilised cubic zirconia. The defect energies and processes are discussed in section 3.3.1. Secondly, the elastic constants, dielectric constants and the associated thermodynamic quantities such as the bulk modulus $B = (C_{11} + 2C_{12})/3$, the anisotropy ratio $A = 2C_{44}/(C_{11} - C_{12})$ and the Cauchy relation failure $\Delta = (C_{12} - C_{44})$ are presented. These results are then compared with those obtained from experiment under discussions. Furthermore, since the calculations deal with quasi-harmonic aprroximation, only the linear variations of the thermodynamic quantities with temperature will be taken into account when comparisons are made with results from experiment. Finally, only results from configurations that produced acceptable results when compared with those from experiment are presented in this chapter.

3.1 CALCULATION OF DEFECT ENERGIES

3.1.1 COMPUTATIONAL PROCEDURE

In brief, the techniques used by the CASCADE program are based on an explicit simulation of the defect and the surrounding region of the lattice (region I), while the remainder of the crystal (see figure 2.3.2.1.1) is treated as a continuum using the Mott-Littleton approximation. Elastic perturbations of the continuum region by the defect are ignored and Newton-Raphson minimization methods are used. These

methods reduce the computer time for a calculation by a factor of about 20 compared with the simpler gradients methods. Calculations were performed with both C = 0.0 and C = 27.89, and although defect energies obtained from the latter were generally lower than those obtained when C = 0.0, the results from C = 0.0 were used in the discussions on the basis of the consistency obtained from perfect lattice calculations when this short range parameter was excluded.

The perfect lattice of ZrO_2 used in the present investigation contained 16 oxygen ions and 8 zirconia ions. Table 3.1.1.1 shows the number of different species for the x = 9.4 and x = 24 concentrations. The lattice was stabilised using configurations with vacancies located at both NNN (figure 3.1.1.1) and NN (figure 3.1.1.2) sites to the yttria ions. Due to the small lattices used in CASCADE runs, the procedure for lattice stabilisation was not as straight forward as in perfect lattice calculations. Consequently, the lattice stabilisation procedure will be discussed in greater detail under perfect lattice calculations in section 3.2.1.

Table 3.1.1.1 Number of species with x = 9.4 and x = 24 concentrations used in defect energy calculations.

	Number of different species			
Yttria content (mol %)	Zr^{4+}	Y^{3+}	O^{2-}	$V_o^{\cdot\cdot}$
9.4	6	2	15	1
24	4	4	14	2

The rigid-ion model potential parameters are shown in table 3.1.1.2(a)-(b). The corresponding shell model potential parameters are listed in table 3.1.1.3(a)-(b).

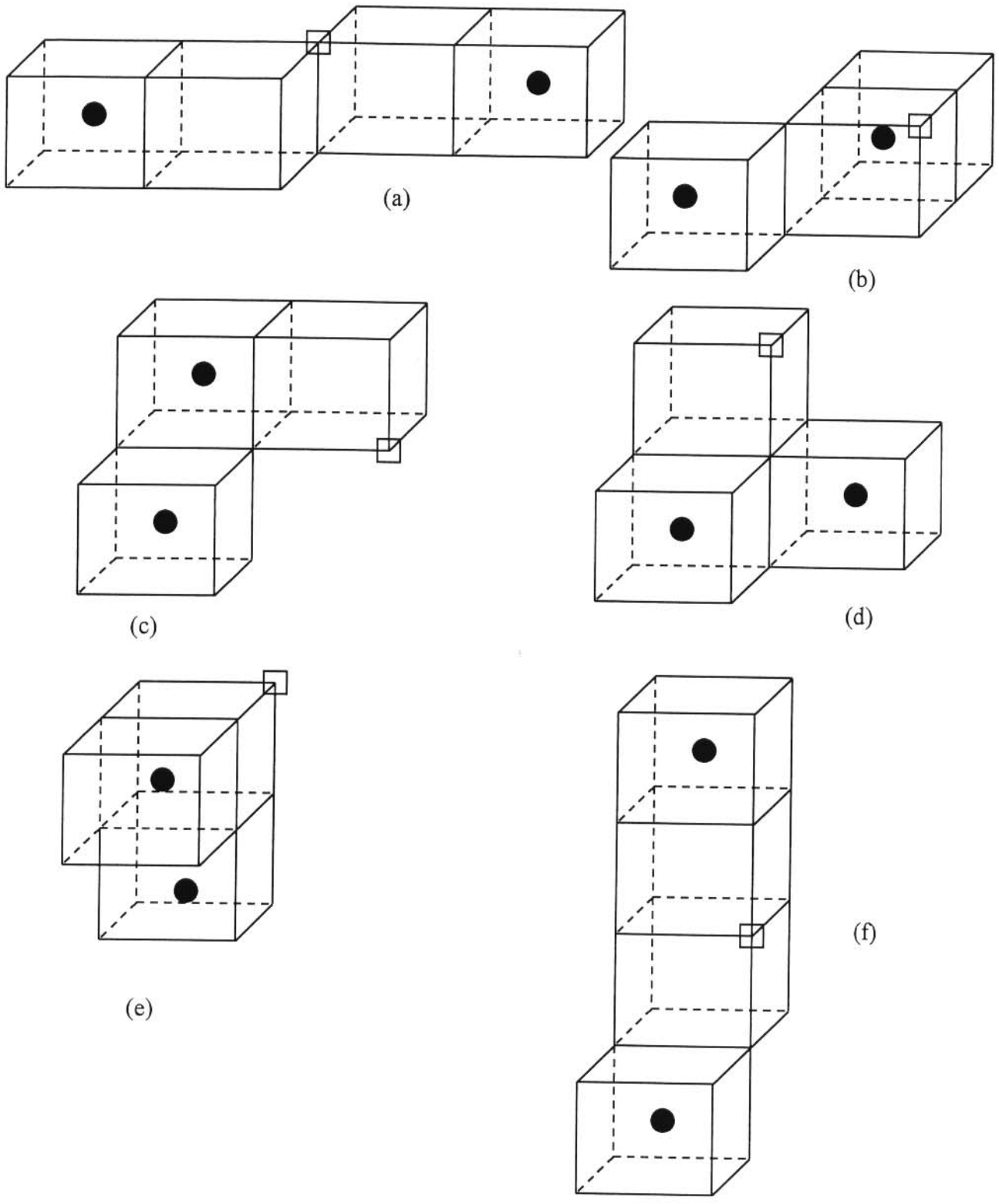

Figure 3.1.1.1 The various structures used for lattice stabilisation of unit cells for calculating defect energies. The Y^{3+} ions are located at NNN sites to the oxygen vacancy

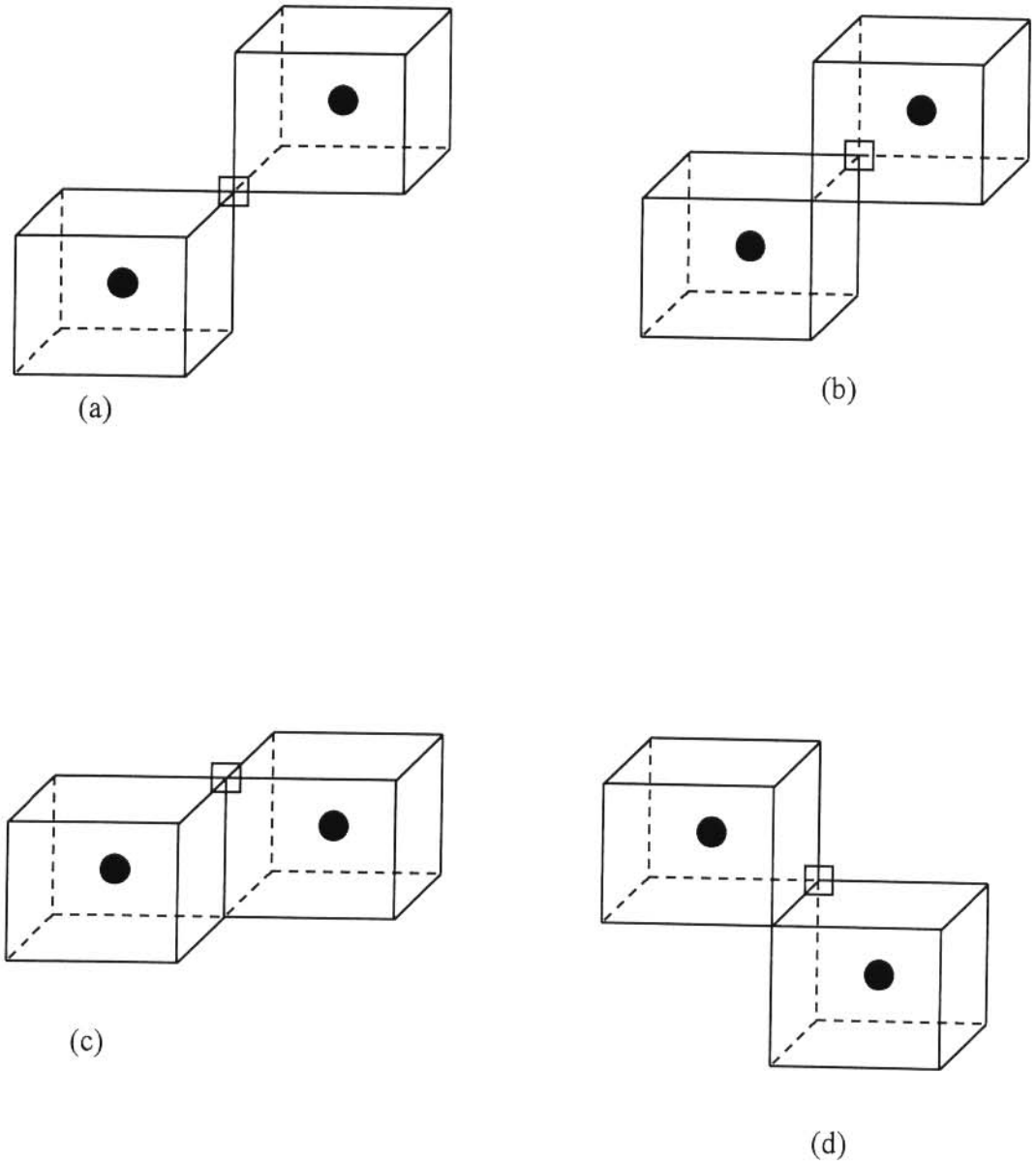

Figure 3.1.1.2 The various structures used for lattice stabilisation of unit cells for calculating defect energies. The Y^{3+} ions are located at NN sites to the oxygen vacancy

Table 3.1.1.2(a) Short range potential parameters used in the rigid-ion model.

Interaction	A (eV)	ρ (eV)	C_o (eV A^{-6})
Zr-O	847.562	0.3885	0.0
Y-O	1345.10	0.3491	0.0
O-O	22764.3	0.1490	0.0

Table 3.1.1.2(b) Rigid-ion parameters

Ion/Interaction	Core charges	Mass	Spring constant k (eV A^{-2})
Zr(core)	4.000	91.244	—
Y(core)	3.000	89.906	—
O(core)-O(shell)	-2.00	15.990	1000000

Table 3.1.1.3(a) Shell model short range potential parameters.

Interaction	A (eV)	ρ_o (A)	C (eV A^{-6})
Zr-O	985.8692	0.37616	0.0
Y-O	1345.100	0.34910	0.0
O-O	22764.30	0.14900	0.0 or 27.89

Table 3.1.1.3(b) Shell model parameters

Interaction	Shell charges	Spring constant k (eV $\mathring{A}^{-2}$)
Zr(core)-Zr(shell)	1.35000	169.617
Y(core)-Y(shell)	-0.25000	145.000
O(core)-O(shell)	-2.07719	27.290

As mentioned in section 2.2.2 the shell model of Dick and Overhauser (1958) is often used in defect studies. This model correctly simulates both the elastic and dielectric properties of materials; which is an essential requirement for reliable calculations of defect energies. It is for this reason that all defect energy calculations reported here were based on the shell model.

Furthermore, ZrO_2 can be stabilised in the cubic phase due to the larger size of the Y^{3+} ions which substitute for the smaller Zr^{4+} ions (Dwivedi and Cormack 1990). Dwivedi and Cormack (1990) have suggested that Y'_{Zr} , because of the larger size of the Y^{3+}, imposes a cubic symmetry on the anion sub-lattice around it. This could be the reason for the stabilisation of cubic zirconia on doping with cations such as Y^{3+}. The defect energies reported in this section were obtained from lattices which were stabilised using the structure in figure 3.1.1.1(a) since this was the only one that converged at CONV with C = 0.0.

Following computer simulation studies by Jackson *et al.* (1986) on uranium oxide, an attempt was made to have about 200 particles in region I (see figure 2.3.2.1.1). In the calculation of oxygen migration energies the saddle point was taken to be a point midway between the oxygen vacancies involved in the migration process. The

activation energy was calculated from the difference between the respective migration and formation energies. That is, $E_{act} = E_{migr} - E_{form}$.

Dwivedi and Cormack (1990) have indicated the existence of interactions between the dopant impurity cations and the charge compensating defects in calcia-stabilised cubic zirconia. This is mainly due to the opposite effective charges on the different defect species. The Kroger-Vink notation, wherein the defect is denoted by a major symbol signifying the species and a subscript indicating the site occupied by the species, was used. A vacancy is denoted by V while an interstitial site is represented by a subscript i. Positive and negative virtual charges are indicated by dot and prime symbols, respectively, as superscripts while defects with no effective charge relative to the unperturbed lattice are indicated by a superscript x. Thus, the interaction between the isolated defects $2Y'_{Zr}$ and $V_o^{\cdot\cdot}$ yields the neutral aggregate $[Y'_{Zr} \cdot V_o^{\cdot\cdot} \cdot Y'_{Zr}]^x$ whose association energy is given by:

$$E_{assoc(i)} = E_{[Y'_{Zr} \cdot V_o^{\cdot\cdot} \cdot Y'_{Zr}]^x} - 2E_{Y'_{Zr}} - E_{V_o^{\cdot\cdot}}$$

Energies of associates from large defect complexes considered in the present investigation may be grouped as follows:

1. simple neutral dopant-vacancy pairs of type $[Y'_{Zr} \cdot V_o^{\cdot\cdot} \cdot Y'_{Zr}]^x$

   The association energy with respect to isolated defects is given by

   $$E_{assoc(i)} = E_{[Y'_{Zr} \cdot V_O^{\cdot\cdot} \cdot Y'_{Zr}]^x} - E_{V_O^{\cdot\cdot}} - 2E_{Y'_{Zr}}$$

2. clusters involving zirconia vacancies.

The associate of type $[Y'_{Zr} \cdot V_O^{\cdot\cdot} \cdot Y'_{Zr}]^x$ with $V_O^{\cdot\cdot}$ at NN sites to the yttria ions (figure 3.1.2.4(b)) was highly unstable, precluding the existence of such a cluster. Negative association energies of various clusters indicate the possibility of formation

of such clusters.

3.1.2 RESULTS FOR DEFECT ENERGIES

Energies of isolated defects in cubic zirconia were calculated from the clusters in figure 3.1.2.1. The results are recorded in tables 3.1.2.1 and 3.1.2.2 for $x = 9.4$ and $x = 24$, respectively, from both CONV, $C = 0.0$ and CONV, $C = 27.89$ (bracketed values). The position of all interstitial defects was in the body center of the empty cube of the anion sublattice.

It was observed from tables 3.1.2.1 and 3.1.2.2, on the basis of lower calculated values, that it was easier to create oxygen vacancies in the $x = 9.4$ concentration than in the $x = 24$ concentration. Furthermore, the oxygen vacancy formation energies were lower, in both concentrations, when $C = 27.89$. On the basis of this observations alone, it was possible to infer that the $x = 9.4$ mol% doped sample would have higher oxygen conductivity. As for interstitial formation energies, their absolute magnitudes seem to suggest a reluctance to interstitial migration in the $x = 9.4$ concentration. However, in the $x = 24$ sample, the propensity was towards interstitial migration. Finally, the high absolute values obtained from cations illustrated the reluctance of migration resulting from these defect species.

The anion vacancy and interstitial migration energies were obtained from the structures in figure 3.1.2.2 and the energies are listed in table 3.1.2.3(a)-(b). Anion activation energies were calculated from the difference between the migration and formation energies. These are also presented in table 3.1.2.3(a)-(b) for $x = 9.4$ and $x = 24$, respectively. The variation of the anion vacancy activation energy with temperature is depicted in figure 3.1.2.3 for $x = 9.4$.

On the basis of the lower calculated activation energy in the $x = 9.4$ sample, it was inferred that this sample would have higher conductivity than the $x = 24$ sample. The results showed clearly that conductivity would be via vacancy migration.

Defect energies of associates of type $[Y'_{Zr} . V_o^{\cdot\cdot} . Y'_{Zr}]^x$ in ZrO_2(9.4 mol% Y_2O_3) were calculated from the configurations in figure 3.1.2.4 and the results are presented in table 3.1.2.4(a)-(b) for both $C = 0.0$ and $C = 27.89$. This has, however, not been done in the $x = 24$ sample because on doping with 24 mol% Y_2O_3 four Zr^{4+} ions, in a sample with 8 Zr^{4+} and 16 O^{2-} ions, are replaced by four Y^{3+} ions, making it difficult to investigate energies of defect complexes involving the interaction of at least two Y'_{Zr} with one or two oxygen vacancies as was done for ZrO_2(9.4 mol% Y_2O_3). However, with advances in computer software larger unit cells would be investigated, permitting the study of larger defect aggregates in ZrO_2(24 mol% Y_2O_3).

The energies of single dopant-vacancy associates in calcia - stabilised cubic zirconia were calculated by Dwivedi and Cormack (1990) using the defect clusters shown in figure 3.1.2.5. The energies are reported in table 3.1.2.5. The highest binding energy was found when the oxygen vacancy was located at NNN sites to a yttria ion.

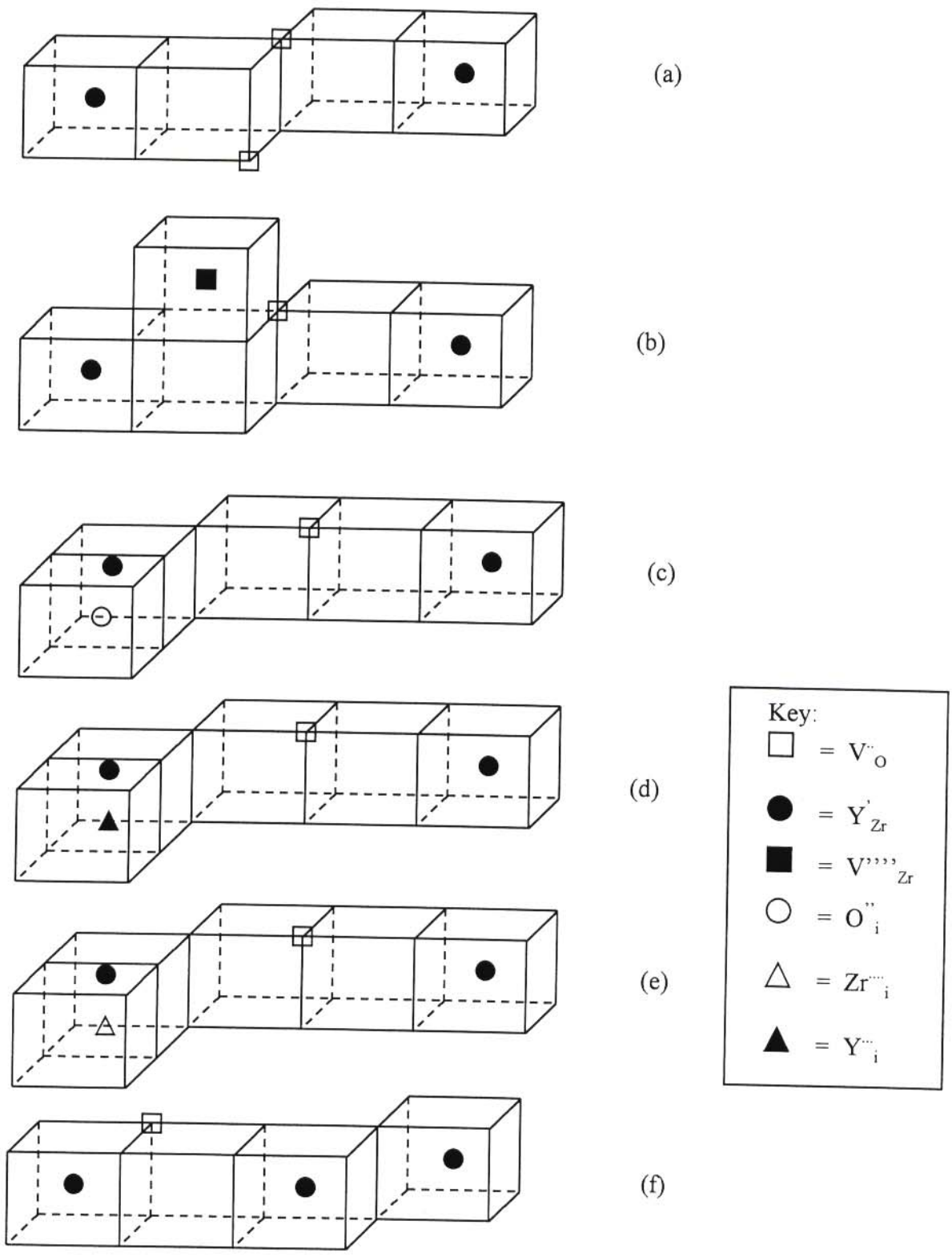

Figure 3.1.2.1 The various defect clusters used for calculating energies of isolated defects in yttria-stabilised cubic zirconia

Table 3.1.2.1 Formation energies of isolated defects in ZrO_2(9.4 mol% Y_2O_3) from CONV, C = 0.0 and CONV, C = 27.89 (bracketed values). The position of all interstitial defects was in the body centre of the empty cube of the anion sublattice.

Defect type	Defect position	Defect energy (eV)	*ZrO_2(x CaO) (eV)
$V_O^{\cdot\cdot}$	Fig 3.1.2.1(a)	13.63 (13.44)	14.77
$V_{Zr}^{''''}$	Fig 3.1.2.1(b)	82.39 (82.06)	86.06
O_i''	Fig 3.1.2.1(c)	-15.87(-15.14)	-9.34
$Zr_i^{\cdot\cdot\cdot\cdot}$	Fig 3.1.2.1(d)	-69.53(-70.08)	-65.913
$Y_i^{\cdot\cdot\cdot}$	Fig 3.1.2.1(e)	-36.20(——)	-12.01#
Y_{Zr}'	Fig 3.1.2.1(f)	34.14 (33.35)	59.86@

* After Dwivedi and Cormack (1990)

\# Formation energy for $Ca_i^{\cdot\cdot}$

@ Formation energy for Ca_{Zr}''

Table 3.1.2.2 Formation energies of isolated defects in ZrO_2(24 mol% Y_2O_3) from CONV, C = 0.0 and CONV, C = 27.89 (bracketed values). The position of all interstitial defects was in the body centre of the empty cube of the anion sublattice.

Defect type	Defect position	Defect energy (eV)
$V_O^{\cdot\cdot}$	Fig 3.1.2.1(a)	16.58 (15.26)
$V_{Zr}^{''''}$	Fig 3.1.2.1(b)	83.45 (——)
O_i''	Fig 3.1.2.1(c)	-10.97(-11.37)
$Zr_i^{\cdot\cdot\cdot\cdot}$	Fig 3.1.2.1(d)	-68.84(-68.25)
$Y_i^{\cdot\cdot\cdot}$	Fig 3.1.2.1(e)	-31.56(-31.41)
Y_{Zr}'	Fig 3.1.2.1(f)	35.51 (35.52)

Key: $V_O^{\cdot\cdot}$ Oxygen vacancy;

$V_{Zr}^{''''}$ Zirconium vacancy;

$O_i^{''}$ Oxygen interstitial ion;

$Zr_i^{\cdot\cdot\cdot\cdot}$ Zirconium interstitial ion;

$Y_{Zr}^{'}$ Yttrium in a Zirconium position; and

$Y_i^{\cdot\cdot\cdot}$ Yttrium interstitial ion.

Following the suggestion by Dwivedi and Cormack (1990), addition of half the association energy to the calculated activation energy gives a value which should be compared with results from experiment. This was done for C = 0.0 at T = 300 and T = 1287 K. The calculated values were compared with those from experiment in table 3.1.2.6.

The positive association energy obtained when C = 27.89 showed that the formation of such associates was doubtful. On the otherhand, when C = 0.0, the possibility of formation of the associates, indicated by negative association energies, is high (table 3.1.2.4(a)).

The experimental values in table 3.1.2.6 were taken from Solier *et al.* (1988). It was evident that the calculated energies from $E_{act} + \frac{1}{2}E_{assoc(i)}$ compared reasonably well with those from experiment. Interactions involving zirconia vacancies are shown in figure 3.1.2.6 while the associated energies are given in table 3.1.2.7. The calculated energies of interactions involving zirconia vacancies were very high, which precluded any existence of such clusters.

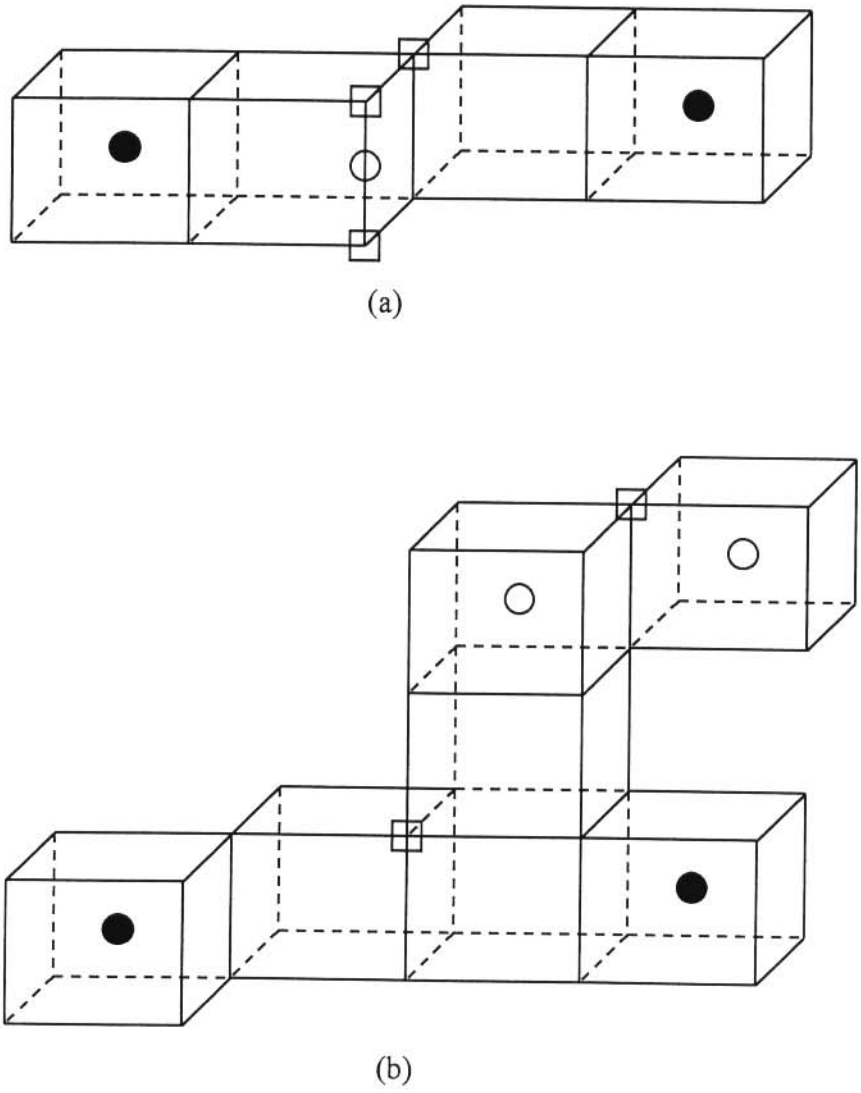

Figure 3.1.2.2 The defect clusters used for the calculation of (a) anion vacancy and (b) anion interstitial migration energy

Table 3.1.2.3(a) Results of migration and activation energies for x = 9.4 from both C = 0.0 and C = 27.89 (bracketed values).

Type of energy	Defect energy (eV)	ZrO_2(x CaO) (eV)
Anion vacancy migration	14.23 (14.11)	
Anion vacancy activation	0.603 (0.670)	0.2-1.37
Anion interstitial migration	-14.17(———)	
Anion interstitial activation	1.670 (———)	

Table 3.1.2.3(b) Results of migration and activation energies for x = 24 from both C = 0.0 and C = 27.89 (bracketed values).

Type of energy	Defect energy (eV)
Anion vacancy migration	17.53 (17.34)
Anion vacancy activation	0.950 (2.080)
Anion interstitial migration	-9.323(-12.04)
Anion interstitial activation	1.647 (0.670)

We are not sure about the reliability of the activation energies for x = 24 samples with C = 27.89 which differ by large amount when compared with those obtained with C = 0.0. These large differences between activation energies obtained with C = 0.0 and C = 27.89 were not observed in the x = 9.4 sample. It is possible that effects associated with complex clusters at high yttria content are taking place.

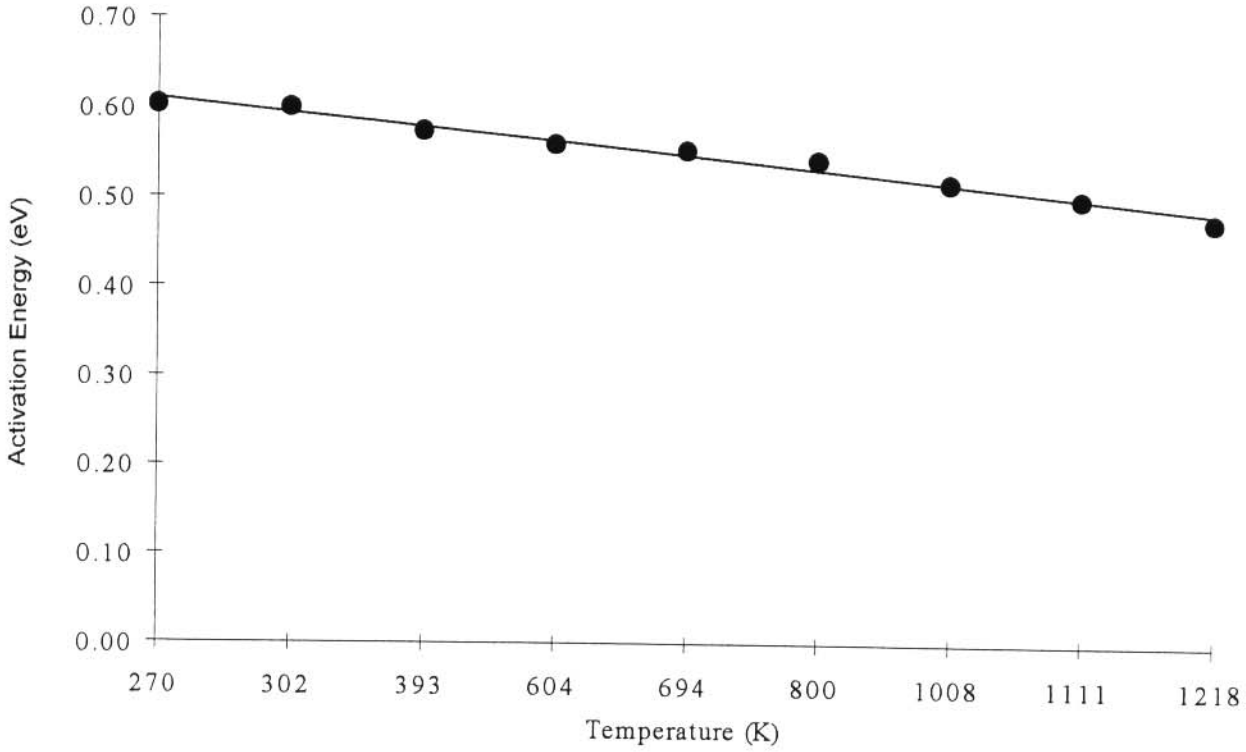

Figure 3.1.2.3 The variation of anion vacancy activation energy with temperature obtained using quasi-harmonic approximation for x = 9.4

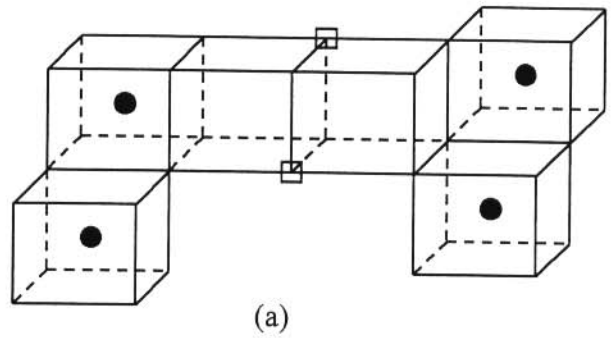

(a)

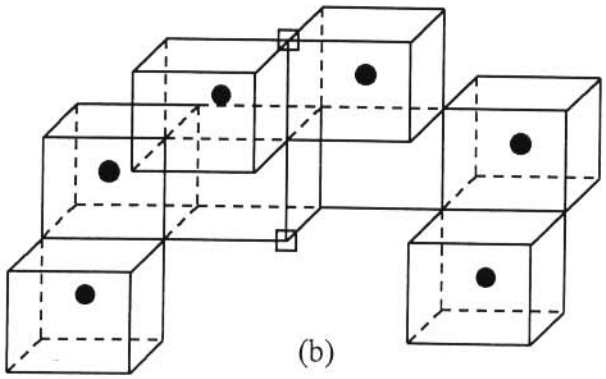

(b)

Figure 3.1.2.4 The various configurations used for calculating defect energies of associates of type $[Y'_{Zr} . V^{\cdot\cdot}_{O} . Y'_{Zr}]^{x}$

Table 3.1.2.4(a) Results of defect energies of associates of type $[Y'_{Zr} \cdot V_O^{\cdot\cdot} \cdot Y'_{Zr}]^x$ in ZrO_2(9.4 mol% Y_2O_3) from CONV, C = 0.0.

Defect type	Defect energy (eV)	$E_{assoc(i)}$ (eV)	$E_{assoc(p,i)}$ (eV)	Defect position
$[Y'_{Zr}.V_O^{\cdot\cdot}.Y'_{Zr}]^x$	81.04	-0.870	———	Fig 3.1.2.4(a)
$[Y'_{Zr}.V_O^{\cdot\cdot}.Y'_{Zr}]^x$	Did not converge			Fig 3.1.2.4(b)

Table 3.1.2.4(b) Results of defect energies of associates of type $[Y'_{Zr} \cdot V_O^{\cdot\cdot} \cdot Y'_{Zr}]^x$ in ZrO_2(9.4 mol% Y_2O_3) from CONV, C = 27.89.

Defect type	Defect energy (eV)	$E_{assoc(i)}$ (eV)	$E_{assoc(p,i)}$ (eV)	Defect position
$[Y'_{Zr}.V_O^{\cdot\cdot}.Y'_{Zr}]^x$	80.93	0.790	———	Fig 3.1.2.4(a)
$[Y'_{Zr}.V_O^{\cdot\cdot}.Y'_{Zr}]^x$	Did not converge			Fig 3.1.2.4(b)

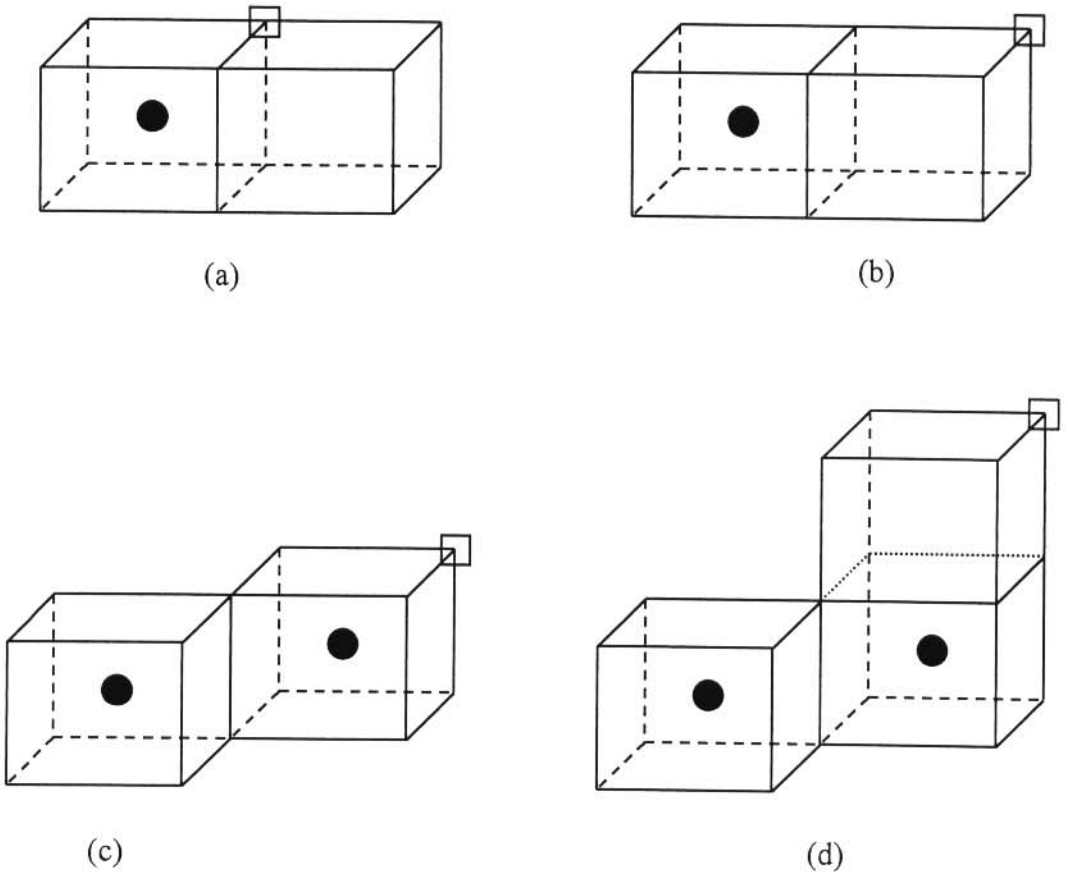

Figure 3.1.2.5 Defect clusters used for calculating defect energies of single dopant-vacancy associates in calcia-stabilised cubic zirconia (Dwivedi and Cormack 1990)

Table 3.1.2.5 Defect energies of single dopant-vacancy associates in calcia - stabilised cubic zirconia (Dwivedi and Cormack 1990).

Defect type	Defect Position	Defect energy (eV)	Assoc energy (eV)
$Ca_{Zr}''.V_O^{\cdot\cdot}]^x$	Fig 3.1.2.5(a)	74.133	-0.495
$[Ca_{Zr}''.V_O^{\cdot\cdot}]^x$	Fig 3.1.2.5(b)	73.951	-0.677
$[Ca_{Zr}''.V_O^{\cdot\cdot}]^x$	Fig 3.1.2.5(c)	74.383	-0.245
$[Ca_{Zr}''.V_O^{\cdot\cdot}]^x$	Fig 3.1.2.5(d)	74.418	-0.210

Table 3.1.2.6 Comparison of the calculated and the experimental anion vacancy activation energies for x = 9.4 from C = 0.0.

Temperature (K)	E_{act} (eV)	$\frac{1}{2}E_{assoc(i)}$ (eV)	$E_{act} + \frac{1}{2}E_{assoc(i)}$ (eV)	E_{act}[Exp]. (eV)
300	0.603 (_)	0.438 (_)	1.041 (_)	1.1600
1287	0.439 (_)	0.438 (_)	0.877 (_)	0.8400

Table 3.1.2.7 Energies of interactions involving zirconia vacancies with C = 0.0 and C = 27.89 (bracketed values).

Defect type	Defect Energy (eV)	$E_{assoc}(i)$ (eV)	Defect position
$[V_O^{\cdot\cdot}.V_{Zr}^{''''}]''$	96.77 (97.10)	0.758 (0.750)	Fig 3.1.2.5(a)
$[V_O^{\cdot\cdot}.V_{Zr}^{''''}.V_O^{\cdot\cdot}]^x$	110.6 (109.5)	0.977 (-0.17)	Fig 3.1.2.5(b)
$[V_O^{\cdot\cdot}.V_{Zr}^{''''}.V_O^{\cdot\cdot}]^x$	Did not converge		Fig 3.1.2.5(c)

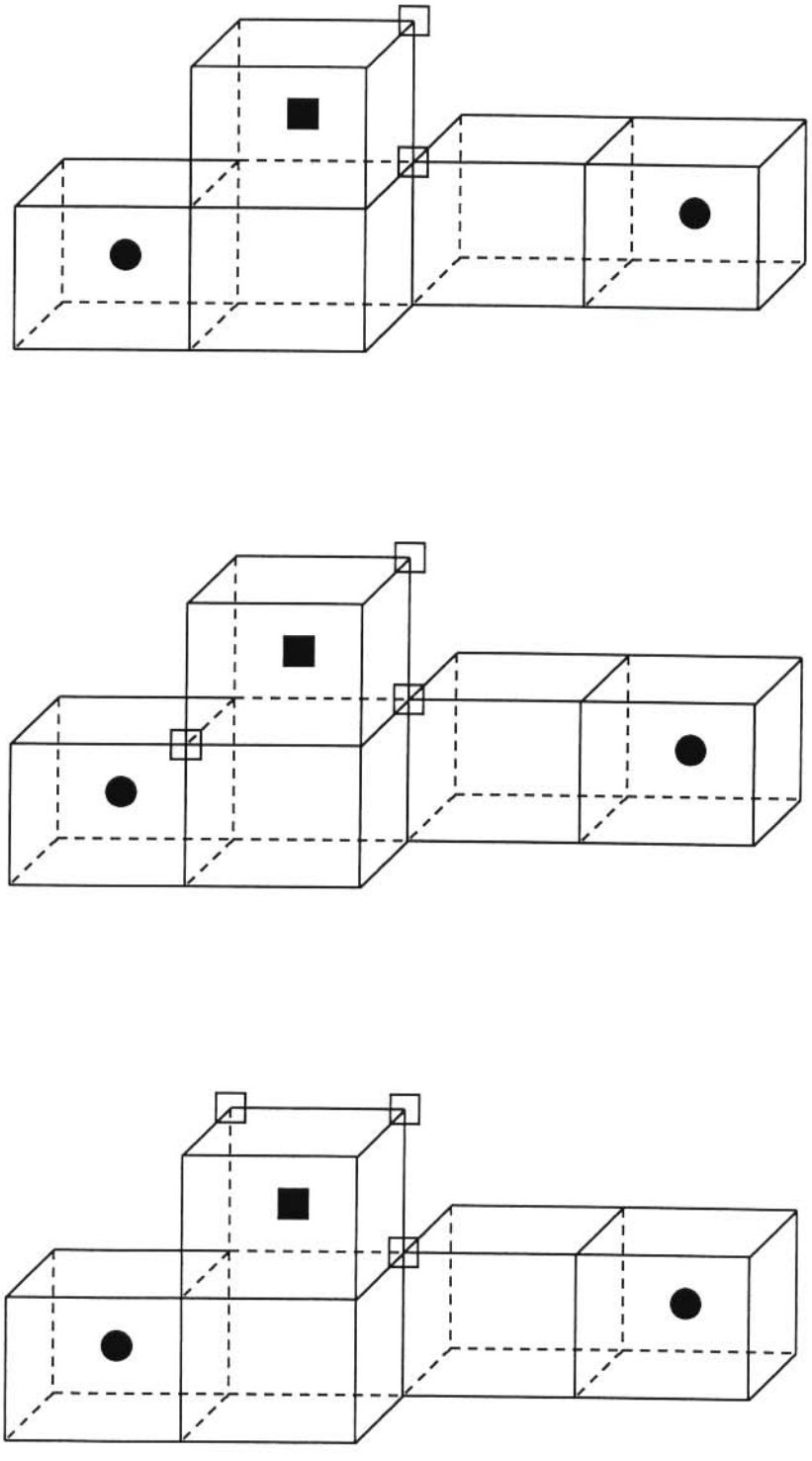

Figure 3.1.2.6 Defect clusters for calculating energies of interactions involving zirconia vacancies

3.2 PERFECT LATTICE CALCULATIONS

Results from perfect lattice calculations are presented in this section. These will be followed by discussions in section 3.3.

3.2.1 COMPUTATIONAL PROCEDURE

In this section the computational procedure followed in the calculation of thermodynamic quantities is presented. The procedure for the construction of supercells is discussed first (same procedure was used in the construction of unit cells used for defect energy calculations). This is followed by a presentation of results from perfect lattice calculations.

Uncertainity prevails around the nature of the structure of dopant-oxygen vacancy complexes in stabilised cubic zirconia (section 1.4.1.1). The two cases wherein the oxygen vacancies were located at NNN and NN sites to the substitutional dopant cations were investigated. The suggestion by Veal *et al.* (1988) that at high concentrations there is a mixture of oxygen vacancies; some at NN and others at NNN positions to the impurity cations was explored for the $x = 24$ concentration.

As discussed in the introduction (section 1.3.3) zirconia can be stabilised in the cubic phase by the addition of appropriate concentrations of Y_2O_3. Pure ZrO_2 was stabilised in the cubic flourite phase at room temperature by the addition of 9.4, 15, 21 and 24 mol% Y_2O_3 according to the formula $Zr_{1-2x}Y_{2x}O_{2-x}$. For instance, for $x = 0.094$ the following was obtained:

$$Zr_{1-2(0.094)}Y_{2(0.094)}O_{2-0.094} = Zr_{0.812}Y_{0.188}O_{1.906}.$$

But originally there were 32 Zr^{4+} ions and 64 Ox^{2-} ions. On doping with 9.4 mol% only $0.812 \times 32\ Zr^{4+} \approx 25.98 \approx 26\ Zr^{4+}$ ions remained, implying the existence of 6 Y^{3+} ions. Charge neutrality was maintained by the creation of 3

oxygen vacancies, resulting in a defective lattice of 61 oxygen ions. The same procedure was followed in doping with the other yttria concentrations. Table 3.2.1.1 shows the number of the different species at various dopant concentrations.

Table 3.2.1.1 Number of ions at various yttria contents used in perfect lattice calculations.

	Number of different species			
Yttria content (mol %)	Zr^{4+}	Y^{3+}	O^{2-}	$V_o^{\cdot\cdot}$
9.4	26	6	61	3
15	22	10	59	5
21	18	14	57	7
24	16	16	56	8

Various configurations involving the positions of the dopant cations relative to the respective oxygen vacancies were tried in order to check the most stable arrangement of the impurity cations and the charge compensating defects. These were labelled the *x*-, *l*- and *y*-group of configurations (see figure 3.2.1.1), in line with the apparent orientation of the dopants with respect to the anion vacancies. Configurations X, X_1, and X_2 belong to the same *x*-group and all have the same orientation of the dopant cations with respect to the oxygen vacancies but with vacancies sitting at different positions. The positions of oxygen vacancies and yttria ions, which sit at NNN sites to the vacancies, for the various orientations considered in the present investigation are the following:

X-configuration:

$V_O^{\cdot\cdot}$(0.375 0.375 0.875)[Y'_{Zr}(0.00 0.25 0.75), Y'_{Zr}(0.75 0.50 0.75)]

$V_O^{\cdot\cdot}$(0.375 0.625 0.625)[Y'_{Zr}(0.00 0.50 0.50), Y'_{Zr}(0.75 0.75 0.50)]

$V_O^{\cdot\cdot}$(0.375 0.125 0.625)[Y'_{Zr}(0.00 0.00 0.50), Y'_{Zr}(0.75 0.25 0.50)]

X_1-configuration:

$V_O^{\cdot\cdot}$(0.375 0.375 0.375)[Y'_{Zr}(0.00 0.25 0.25), Y'_{Zr}(0.75 0.50 0.25)]

$V_O^{\cdot\cdot}$(0.375 0.625 0.125)[Y'_{Zr}(0.00 0.50 0.00), Y'_{Zr}(0.75 0.75 0.00)]

$V_O^{\cdot\cdot}$(0.375 0.125 0.125)[Y'_{Zr}(0.00 0.00 0.00), Y'_{Zr}(0.75 0.25 0.00)]

X_2-configuration:

$V_O^{\cdot\cdot}$(0.625 0.375 0.625)[Y'_{Zr}(0.25 0.25 0.50), Y'_{Zr}(1.00 0.50 0.50)]

$V_O^{\cdot\cdot}$(0.375 0.875 0.875)[Y'_{Zr}(0.00 0.75 0.75), Y'_{Zr}(0.75 1.00 0.75)]

$V_O^{\cdot\cdot}$(0.375 0.125 0.125)[Y'_{Zr}(0.00 0.00 0.00), Y'_{Zr}(0.75 0.25 0.00)]

L - configuration:

$V_O^{\cdot\cdot}$(0.125 0.375 0.125)[Y'_{Zr}(0.50 0.50 0.00), Y'_{Zr}(0.00 0.50 0.50)]

$V_O^{\cdot\cdot}$(0.125 0.625 0.375)[Y'_{Zr}(0.50 0.75 0.25), Y'_{Zr}(0.00 0.75 0.75)]

$V_O^{\cdot\cdot}$(0.375 0.375 0.375)[Y'_{Zr}(0.75 0.50 0.25), Y'_{Zr}(0.25 0.50 0.75)]

L_1-configuration:

$V_O^{\cdot\cdot}$(0.375 0.375 0.375)[Y'_{Zr}(0.00 0.25 0.25), Y'_{Zr}(0.50 0.25 0.75)]

$V_O^{\cdot\cdot}$(0.625 0.625 0.375)[Y'_{Zr}(0.25 0.50 0.25), Y'_{Zr}(0.75 0.50 0.75)]

$V_O^{\cdot\cdot}$(0.375 0.875 0.375)[Y'_{Zr}(0.00 0.75 0.25), Y'_{Zr}(0.50 0.75 0.75)]

L_2-configuration:

$V_O^{\cdot\cdot}$(0.375 0.625 0.125)[Y'_{Zr}(0.00 0.50 0.00), Y'_{Zr}(0.50 0.50 0.50)]

$V_O^{\cdot\cdot}$(0.625 0.125 0.375)[Y'_{Zr}(0.25 0.00 0.25), Y'_{Zr}(0.75 0.00 0.75)]

$V_O^{\cdot\cdot}$(0.625 0.375 0.125)[Y'_{Zr}(0.25 0.25 0.00), Y'_{Zr}(0.75 0.25 0.50)]

L_3-configuration:

$V_O^{\cdot\cdot}$(0.375 0.125 0.625)[Y'_{Zr}(0.00 0.00 0.50), Y'_{Zr}(0.50 0.00 1.00)]

$V_O^{\cdot\cdot}$(0.375 0.875 0.375)[Y'_{Zr}(0.00 0.75 0.25), Y'_{Zr}(0.50 0.75 0.75)]

$V_O^{\cdot\cdot}$(0.375 0.625 0.125)[Y'_{Zr}(0.00 0.50 0.00), Y'_{Zr}(0.50 0.50 0.50)]

L_4-configuration:

$V_O^{\cdot\cdot}$(0.375 0.625 0.625)[Y'_{Zr}(0.00 0.50 0.50), Y'_{Zr}(0.50 0.50 1.00)]

$V_O^{\cdot\cdot}$(0.375 0.125 0.125)[Y'_{Zr}(0.00 0.00 0.00), Y'_{Zr}(0.50 0.00 0.50)]

$V_O^{\cdot\cdot}$(0.875 0.625 0.625)[Y'_{Zr}(0.50 0.50 0.50), Y'_{Zr}(1.00 0.50 1.00)]

L_5-configuration:

$V_O^{\cdot\cdot}$(0.875 0.125 0.125)[Y'_{Zr}(0.50 0.00 0.00), Y'_{Zr}(1.00 0.00 0.50)]

$V_O^{\cdot\cdot}$(0.625 0.375 0.625)[Y'_{Zr}(0.25 0.25 0.50), Y'_{Zr}(0.75 0.25 1.00)]

$V_O^{\cdot\cdot}$(0.375 0.875 0.375)[Y'_{Zr}(0.00 0.75 0.25), Y'_{Zr}(0.50 0.75 0.75)]

Y-configuration:

$V_O^{\cdot\cdot}$(0.875 0.375 0.375)[Y'_{Zr}(0.75 0.25 0.00), Y'_{Zr}(0.75 0.50 0.75)]

$V_O^{\cdot\cdot}$(0.125 0.625 0.375)[Y'_{Zr}(0.00 0.50 0.00), Y'_{Zr}(0.00 0.75 0.75)]

$V_O^{\cdot\cdot}$(0.375 0.375 0.375)[Y'_{Zr}(0.25 0.25 0.00), Y'_{Zr}(0.25 0.50 0.75)]

Y_1-configuration:

$V_O^{\cdot\cdot}$(0.625 0.625 0.375)[Y'_{Zr}(0.50 0.50 0.00), Y'_{Zr}(0.50 0.75 0.75)]

$V_O^{\cdot\cdot}$(0.625 0.125 0.375)[Y'_{Zr}(0.50 0.00 0.00), Y'_{Zr}(0.50 0.25 0.75)]

$V_O^{\cdot\cdot}$(0.125 0.125 0.375)[Y'_{Zr}(0.00 0.00 0.00), Y'_{Zr}(0.00 0.25 0.75)]

As a way of example, $V_O^{\cdot\cdot}$(0.375 0.375 0.875)[Y'_{Zr}(0.00 0.25 0.75), Y'_{Zr}(0.75 0.50 0.75)] denoted an oxygen vacancy located at 0.375 0.375 0.875. Associated with this vacancy there were two yttria ions, sitting at 0.00 0.25 0.75 and 0.75 0.50 0.75. Figure 3.2.1.1(a)-(d) shows the various structures for cations sitting at NNN positions to the oxygen vacancies, as well as the inoic positions in a 96 ion supercell for x = 9.4.

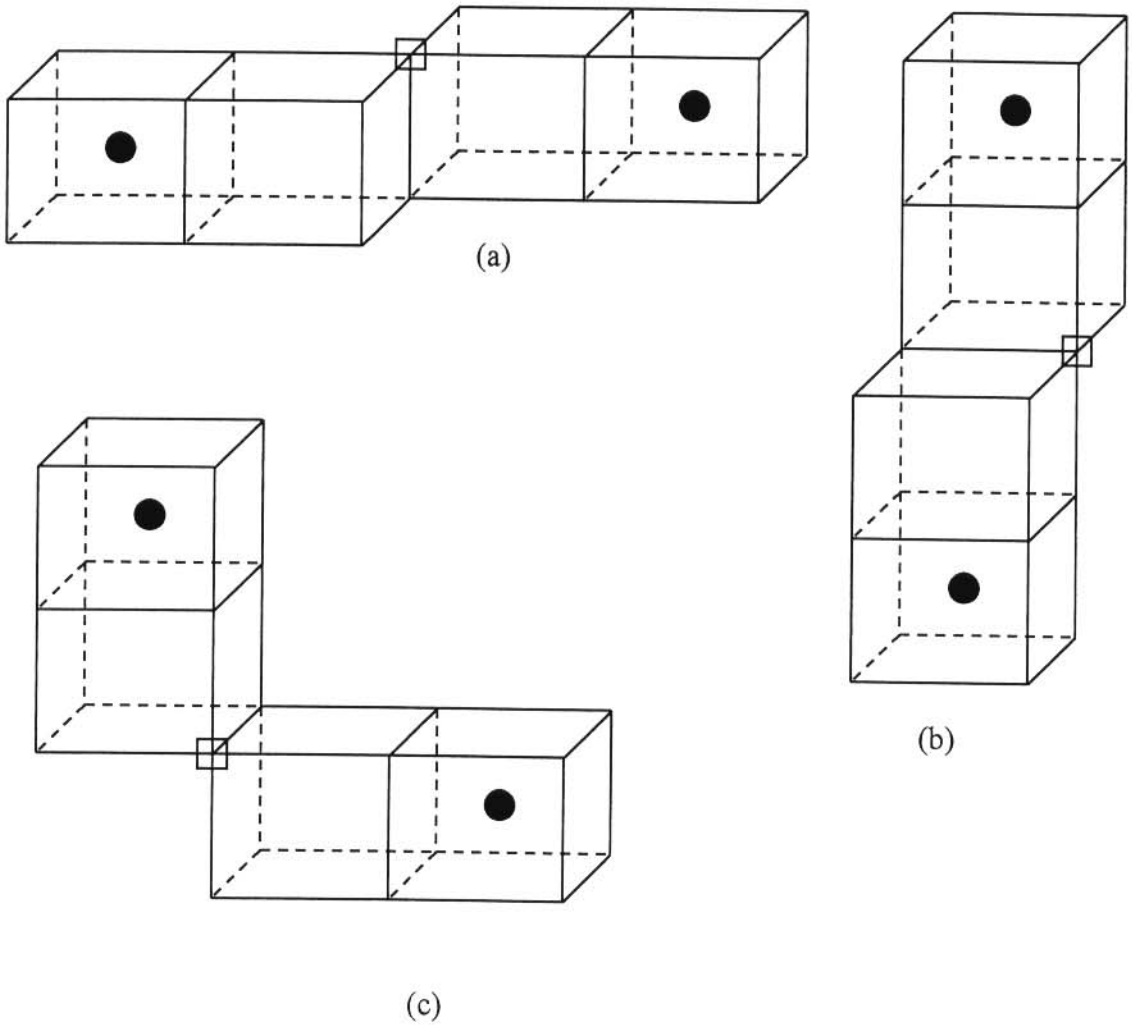

Figure 3.2.1.1(a) The various structures used for lattice stabilisation with Y^{3+} ions located at NNN distances to the oxygen vacancies: (a) *x*-, (b) *y*- and (c) *l*- configuration

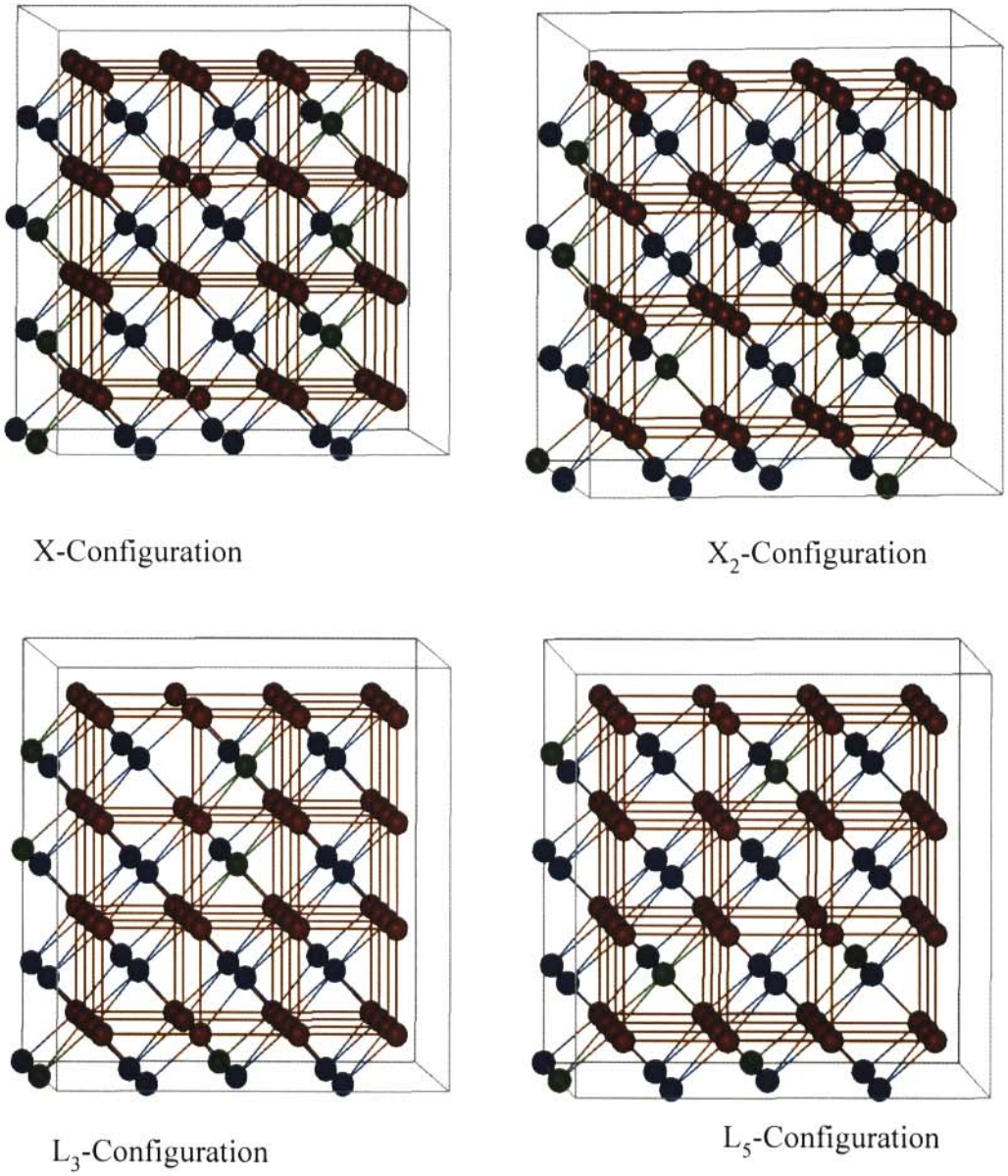

Figure 3.2.1.1(b) Ionic positions in 96 ions supercells for the x = 9.4 sample with the X-, X_2-, L_3- and L_5-configurations

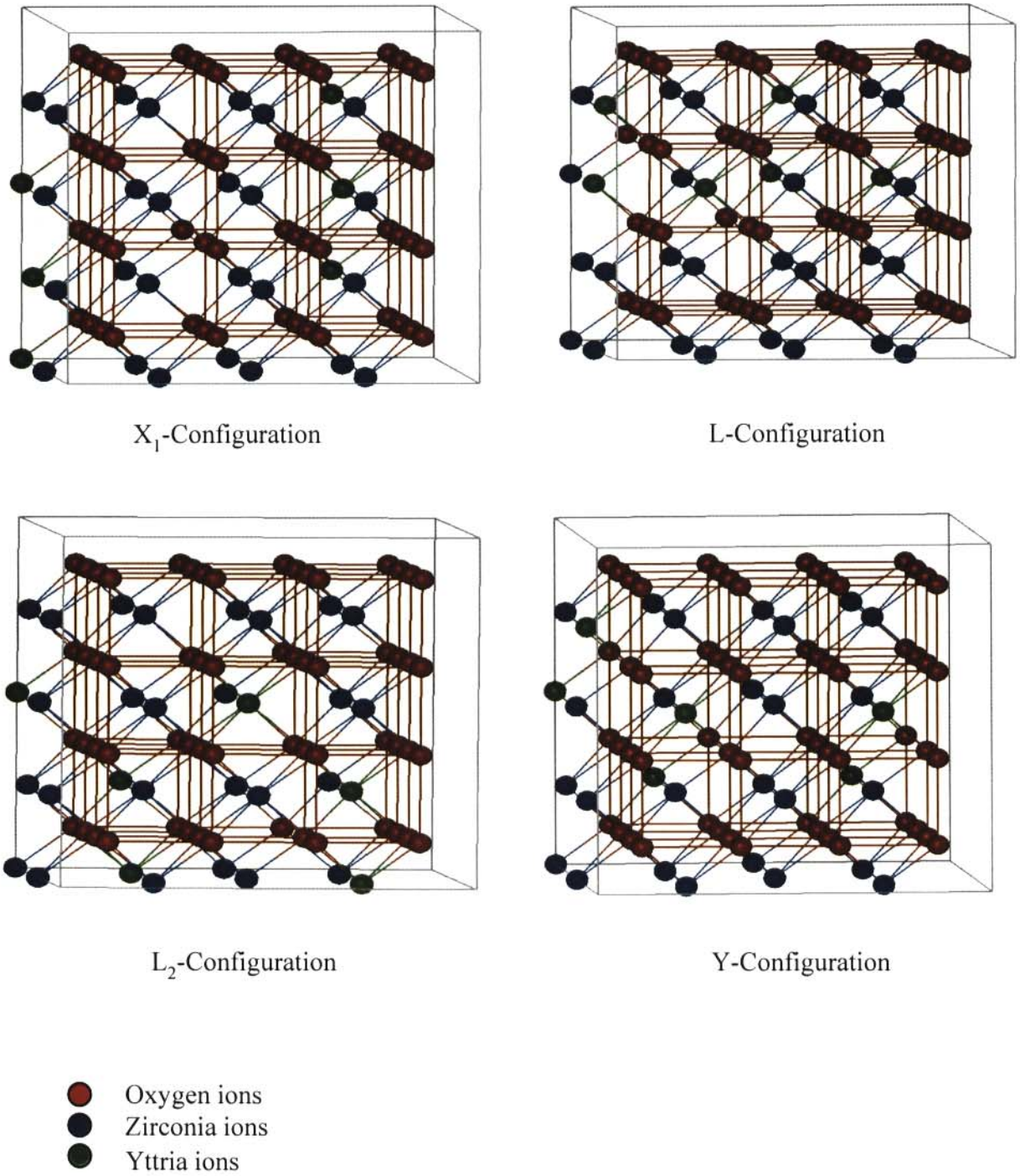

Figure 3.2.1.1(c) Ionic positions in 96 ions supercells for the x = 9.4 samples with the X_1-, L-, L_2- and Y-configurations

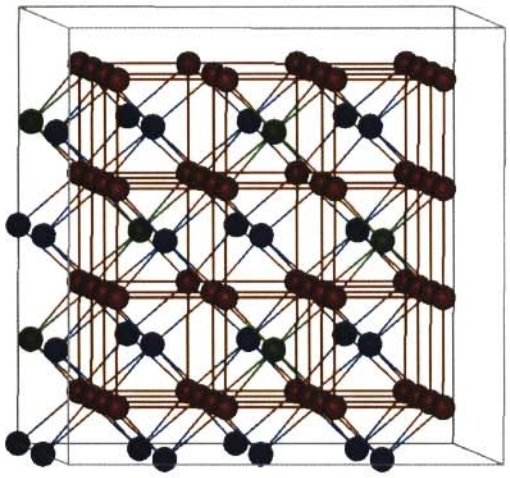

L_1-Configuration

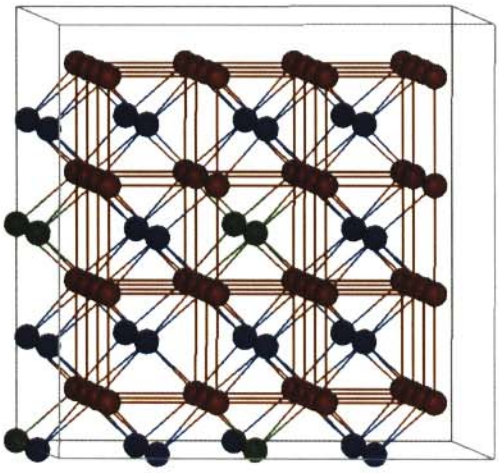

L_4-Configuration

Oxygen ions
Zirconia ions
Yttria ions

Figure 3.2.1.1(d) Ionic positions in 96 ions supercells for the x = 9.4 sample with the L_1 and L_4-configurations

3.2.2 RESULTS FROM PERFECT LATTICE CALCULATIONS

Results from perfect lattice calculations are presented in this section. Results from lattices with unrelaxed coordinates are presented first. However, the failure of the QHA has lead to the consideration of relaxed coordinates, which greately improved the linear reduction of elastic constants with temperature. High temperature Brillouin scattering and refractive index measurements (Botha *et al.* 1993) were used to study the behaviour of elastic constants in yttria-stabilised cubic zirconia for both the $x = 9.4$ and $x = 24$ samples, and in the 300 - 1400 K temperature region. They have compared the behaviour of thermodynamic quantities in these two samples. In order to compare our results with these experimental observations, we show comparisons of the thermodynamic properties in these samples in this section.

Experimental thermodynamic properties are presented in table 3.2.2.1. This is followed by the corresponding calculated values in table 3.2.2.2(a)-(d) from the various structures, for runs at both constant volume (CONV) and constant pressure (CONP) and with either $C = 0.0$ or $C = 27.89$, for the $x = 9.4$ concentration. The elastic constants in table 3.2.2.1 were taken from the ultrasonic work by Hart *et al.* (1986) while the static dielectric constant and high frequency dielectric constants were reported by Lanagan *et al.* (1989) and Botha *et al.* (1993), respectively.

Table 3.2.2.1 Experimental results for elastic and dielectric constants.

Thermodynamic quantity	Yttria content (mol%)			
	9.4	15	21	24
C_{11}(GPa)	401.4	387.9	367.8	357.2
C_{12}(GPa)	105.6	104.3	105.8	104.8
C_{44}(GPa)	57.46	64.25	71.25	72.16
ϵ_0	27.3			
ϵ_∞	2.19			2.17

The room temperature calculations in ZrO_2(9.4 mol% Y_2O_3) with impurity cations located at both NNN and NN positions to the charge compensating defects and at CONV and CONP for C = 0.0 and C = 27.89 show that in general, the values for CONV, C = 27.89 and with vacancies located at NNN sites to Y^{3+} ions agree reasonably well with experimental findings (see tables 3.2.2.2(a)-(d) and 3.2.2.1). This highlighted the role played by the inclusion of the dispersive and the van der Waals interactions very well. Reasonable thermodynamic values for vacancies located at NN positions to the dopant cations were also obtained with CONV, C = 27.89 (see table 3.2.2.4.(b)). Recall that the van der Waals interactions are occasionally important in ionic systems where they may provide attraction between NNN ions (section 2.2.2). It was gratifying to see that the adopted interionic potential model produced an accurate description of the next-nearest neighbour interactions.

Table 3.2.2.2(a) Results of elastic and dielectric constants for x = 9.4, for various configurations, from CONV, C = 0.0 and with Y^{3+} ions located at NNN to the oxygen vacancies.

	Shell model				Rigid-ion model			
Config.	C_{11} (GPa)	C_{12} (GPa)	C_{44} (GPa)	ϵ_0	C_{11} (GPa)	C_{12} (GPa)	C_{44} (GPa)	ϵ_0
X	Did not converge				402.1	112.9	78.03	22.08
X_1	409.1	98.46	82.64	27.65	395.4	117.4	62.23	21.57
X_2	430.7	123.6	87.05	26.70	405.2	113.8	82.02	23.15
Y	404.0	116.0	80.32	31.09	382.5	108.8	80.57	19.97
Y_1	435.7	116.4	79.64	23.10	396.8	120.7	81.92	20.25
L	432.5	117.6	94.54	26.76	396.4	102.8	77.79	27.20
L_1	393.3	103.9	77.44	24.11	352.7	112.6	78.13	22.42
L_2	414.1	108.0	92.25	27.42	334.5	140.6	67.60	28.43
L_3	439.0	126.2	95.06	25.80	394.1	124.5	72.43	22.84
L_4	425.8	118.6	99.23	24.75	382.2	118.3	79.29	24.38
L_5	372.0	101.5	80.91	28.38	393.1	112.4	87.58	21.58
XLY	411.6	98.36	87.10	26.26	Did not converge			
$X_1L_1Y_1$	437.4	127.1	96.67	31.57	347.5	143.2	72.79	26.45
$X_1L_2Y_1$	431.5	116.5	88.68	24.87	387.7	114.0	76.59	23.42

Table 3.2.2.2(b) Results of elastic and dielectric constants for x = 9.4, for various configurations, from CONV, C = 27.89 and with Y^{3+} ions located at NNN to the oxygen vacancies.

	Shell model				Rigid-ion model			
Config.	C_{11} (GPa)	C_{12} (GPa)	C_{44} (GPa)	ϵ_0	C_{11} (GPa)	C_{12} (GPa)	C_{44} (GPa)	ϵ_0
X	402.4	96.72	86.19	28.09	306.1	152.8	61.63	36.88
X_1	325.9	26.19	71.87	33.08	366.0	86.34	70.69	21.30
X_2	Did not converge				349.5	74.19	60.44	21.66
Y	384.9	94.87	74.88	27.20	296.0	57.41	44.56	29.09
Y_1	Did not converge				373.8	88.13	77.43	20.81
L	383.1	103.7	84.01	33.01	351.7	94.88	92.41	23.44
L_1	395.3	87.78	87.75	26.76	Did not converge			
L_2	407.9	107.9	76.69	28.97	374.5	110.2	66.84	23.86
L_3	400.3	84.87	82.25	28.87	408.8	111.3	77.89	23.12
L_4	394.5	88.01	79.77	25.43	385.9	119.1	52.45	27.82
L_5	417.5	95.44	84.20	25.51	Did not converge			
XLY	319.1	24.47	75.71	30.40	366.7	107.2	74.65	20.80
$X_1L_1Y_1$	399.8	85.89	90.92	24.64	336.5	78.12	69.49	21.84
$X_1L_2Y_1$	406.3	96.53	80.53	27.89	398.9	114.5	69.56	22.45

Table 3.2.2.2(c) Results of elastic and dielectric constants for $x = 9.4$, for various configurations, from CONP, $C = 0.0$ and with Y^{3+} ions located at NNN to the oxygen vacancies.

	Shell model				Rigid-ion model			
Config.	C_{11} (GPa)	C_{12} (GPa)	C_{44} (GPa)	ϵ_0	C_{11} (GPa)	C_{12} (GPa)	C_{44} (GPa)	ϵ_0
X	305.3	109.0	61.65	17.31	279.8	98.44	56.88	12.83
X_1	335.8	89.56	71.55	28.05	Did not converge			
X_2	406.7	101.3	83.58	30.70	201.3	39.71	49.18	14.99
Y	201.1	30.92	51.12	16.93	222.7	52.02	49.45	15.40
Y_1	Did not converge				294.4	107.4	63.18	13.20
L	270.6	85.95	70.78	17.11	Did not converge			
L_1	316.4	65.91	67.72	23.49	Did not converge			
L_2	Did not converge				299.2	91.40	54.73	19.80
L_3	350.3	90.51	64.59	25.25	Did not converge			
L_4	Did not converge				251.6	117.6	90.53	10.80
L_5	336.9	95.51	63.09	25.86	279.8	69.83	46.91	21.42
XLY	271.8	115.2	88.45	15.26	Did not converge			
$X_1L_1Y_1$	Did not converge				266.7	108.6	46.79	13.27
$X_1L_2Y_1$	288.7	81.47	64.71	26.40	Did not converge			

Table 3.2.2.2(d) Results of elastic and dielectric constants for $x = 9.4$, for various configurations, from CONP, $C = 27.89$ and with Y^{3+} ions located at NNN to the oxygen vacancies.

	Shell model				Rigid-ion model			
Config.	C_{11} (GPa)	C_{12} (GPa)	C_{44} (GPa)	ϵ_0	C_{11} (GPa)	C_{12} (GPa)	C_{44} (GPa)	ϵ_0
X	393.5	96.33	84.96	27.95	275.6	101.5	51.99	18.52
X_1	349.0	62.92	83.80	22.28	312.4	89.19	68.67	18.63
X_2	316.4	91.22	68.76	20.78	370.3	108.1	74.90	20.92
Y	394.2	93.36	74.14	30.55	295.8	108.5	58.09	14.00
Y_1	Did not converge				300.5	117.0	69.98	12.42
L	403.3	113.4	88.70	29.79	281.4	91.58	52.44	16.12
L_1	395.1	90.16	87.59	26.00	271.5	80.18	54.05	17.57
L_2	411.1	107.6	78.76	29.02	314.3	61.25	66.67	24.69
L_3	391.5	71.21	84.37	26.51	366.9	99.00	63.80	25.49
L_4	392.4	92.92	84.56	23.85	340.6	85.35	67.12	20.74
L_5	411.4	82.62	83.67	26.32	289.3	79.46	66.39	17.23
XLY	346.0	61.94	70.76	29.89	325.3	92.19	68.01	16.40
$X_1L_1Y_1$	397.9	91.25	89.56	24.59	303.3	117.6	63.44	12.22
$X_1L_2Y_1$	399.0	90.59	81.97	27.08	288.9	88.71	73.63	14.76

It was evident from tables 3.2.2.2(a)-(d) that it is often difficult to strike a balance between the elastic constants and the dielectric constants. This affirmed that indeed these properties originated from different sources (section 2.3.1). The values of C_{11} obtained from CONV, $C = 0.0$ runs were generally high while the

calculated values of ϵ_0 were reasonable. Furthermore, the calculated values of ϵ_0 obtained from the rigid-ion model agreed well with experimental results. Although polarizability and short range parameters can be derived consistently for alkali halides, yielding transferable parameters, a similar approach for oxides has not been successful. This is ascribed to the fact that the O^{2-} ion does not exist as a stable free ion, the second electron being bound only by the Madelung potential (Lewis 1985). A strong variation in electronic polarizability with crystalline enviroment is thus expected. It was found that the inclusion of the dispersive and the van der Waals interactions lowered the values of the elastic constants while the static dielectric constants increased. Furthermore, although the elastic and static dielectric constants were reproduced very well by the shell model, the rigid-ion model generally failed when C = 27.89. Results obtained from CONP were generally poor as compared with those from CONV and experiment, with worse values obtained from CONP, C = 0.0 runs. Furthermore, in contrast to the behaviour with CONV, C = 27.89 the elastic constants obtained from CONP, C = 27.89 were higher that those from the CONP, C = 0.0 runs.

It is worth noting that certain configurations were found to be unstable (e.g. *x*-configuration, CONV, C = 0.0 in table 3.2.2.1(a)). It is possible that these are configurations in which the yttria ions were forced to have a sevenfold coordination leading to the prevalance of strong vacancy-vacancy interactions as reported by Subbarao and Ramakrishnan (1979) and Dwivedi and Cormack (1990).

In this work different configurations (figure 3.2.2.1) were tried in order to test their relative stabilities so that the most stable configuration could be used in molecular dynamics studies. In this respect two approaches were followed: (a) relaxation with the calculated crystallographic coordinates and (b) relaxation with 'relaxed' ionic

coordinates. Although the calculated thermodynamic properties in the first approach were reasonable when compared with experimental values (tables 3.2.2.2(a)-(d)), calculations performed via the quasi-harmonic approximation (QHA) showed large deviations and scattering from linearity (figures 3.2.2.1), especially when C = 27.89. The variation of C_{11}, for the X_1-, L_4-, and Y-configurations with temperature is shown in figure 3.2.2.1 for structures that have not been relaxed previously. The variation of all elastic constants with temperature for relaxed coordinates, and for various configurations, are shown in figure 3.2.2.2 from CONV with (i) C = 0.0 and (ii) C = 27.89 for x = 9.4. It must be noted that only results from those configurations that have reproduced experimental results are shown in the results. For instance, although six different *l*-configurations were tested, the L_4-configuration was found to reproduce experimental results consistently. Consequently, results from this configuration were shown.

The L_4-configuration showed some degree of consistency (see figure 3.2.2.1), with the scatter of points reduced. There appeared to be a softening of C_{11} above 1000K. This behaviour was not visible in the other configurations. This problem was overcome through approach (b) wherein the structures were first brought to equilibrium by relaxation at CONP, C = 27.89 since the runs at CONP, C = 0.0 always yielded poor results (see table 3.2.2.1). Constant pressure calculations were performed since in this case both the lattice vectors and the ionic coordinates were relaxed, thus effectively bringing the structure much closer to equilibrium. This was evidenced by the fact that subsequent runs lasted, on the average, only twenty minutes as compared with the average two and half hours taken in the initial run on the ALPHA DEC 300 AXP system. The subsequent runs were done at constant volume with C = 0.0 since this has reproduced the linear reduction of elastic constants with increasing temperature from unrelaxed coordinates better.

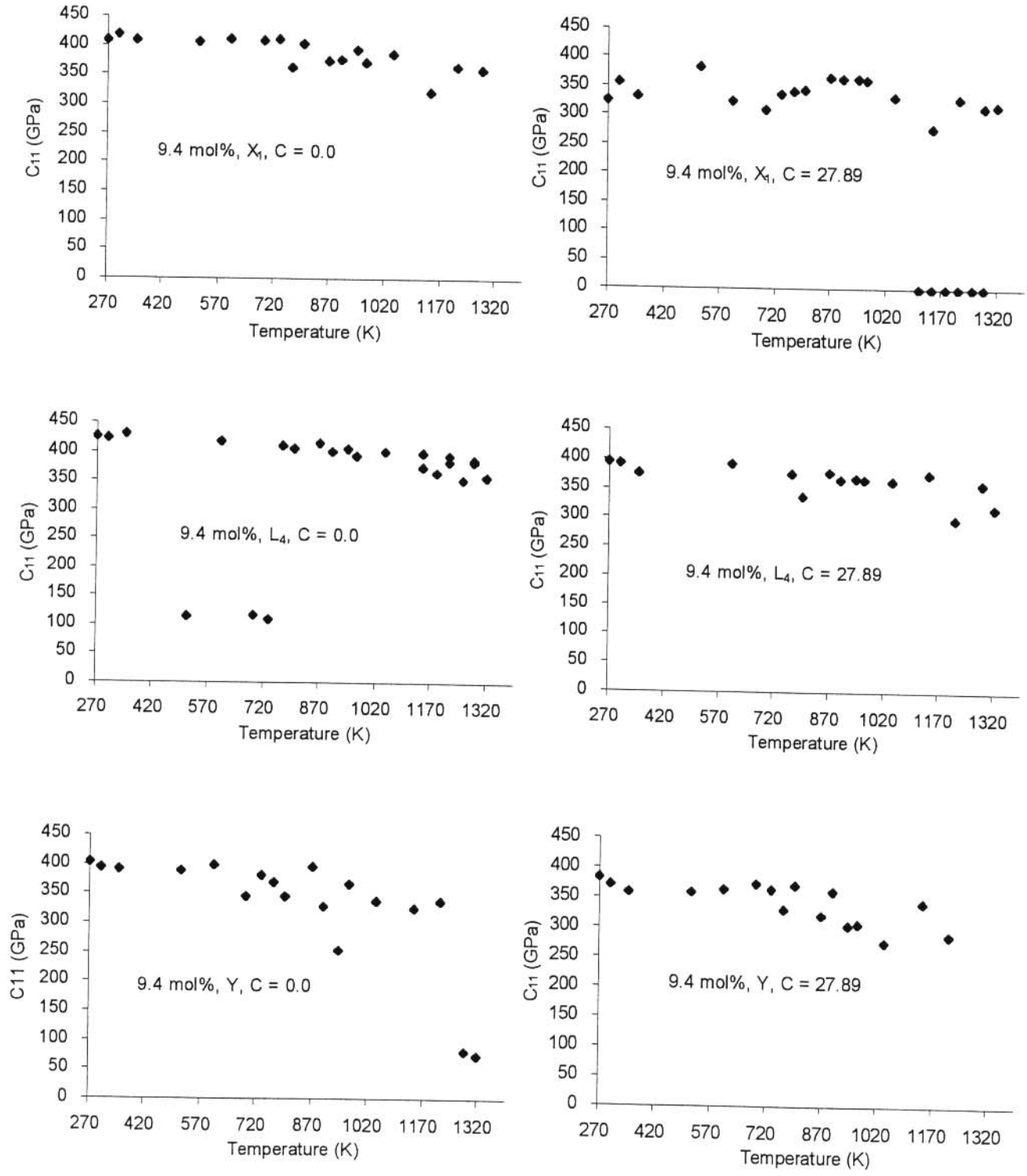

Figure 3.2.2.1 Temperature variation of C_{11} for x = 9.4 with the X_1, L_4- and Y- configurations (unrelaxed co-ordinates), from CONV with C = 0.0 and 27.89

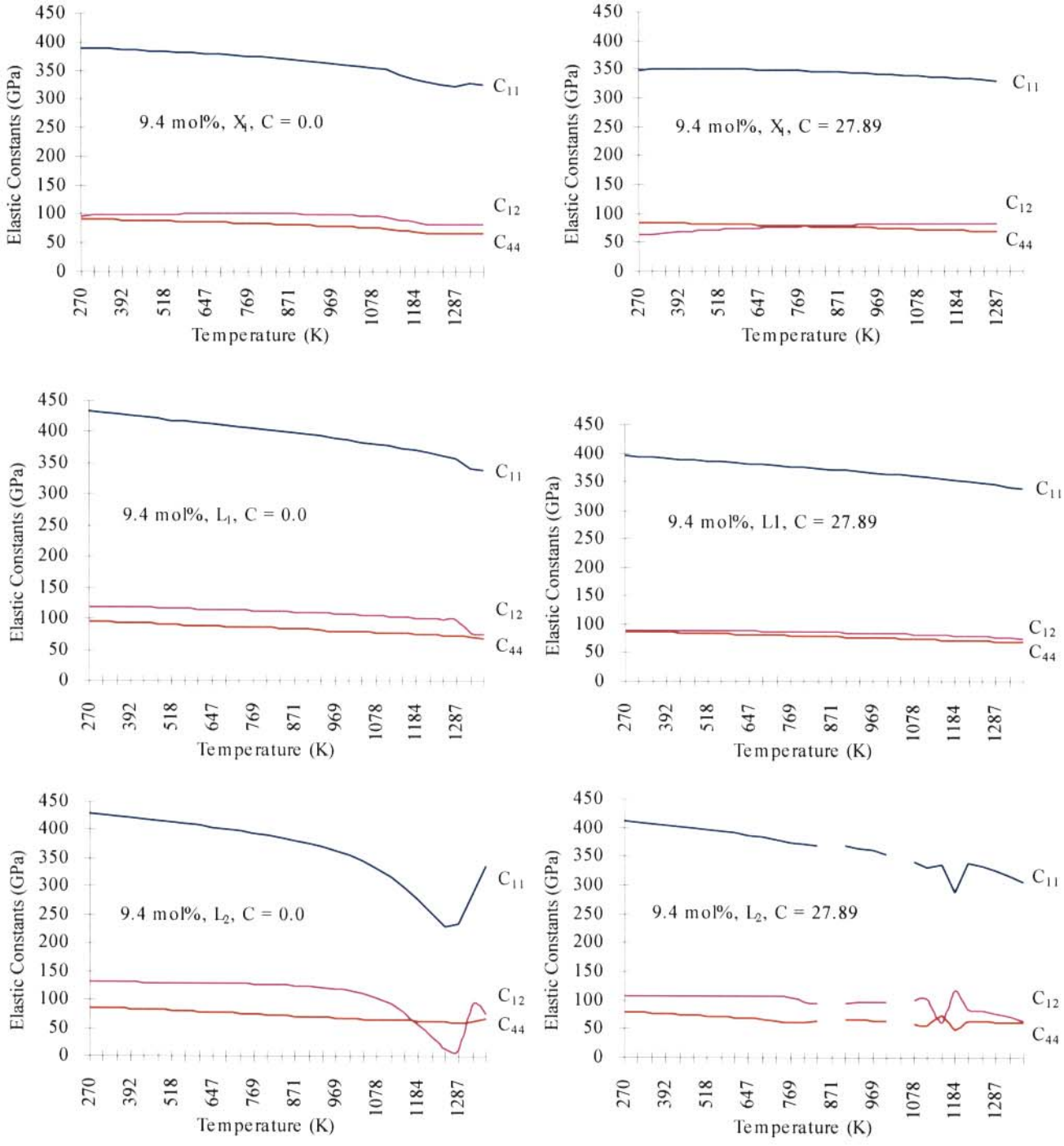

Figure 3.2.2.2(a) Temperature variation of all elastic constants for x = 9.4 from the X_1-, L_1- and L_2-configurations (relaxed co-ordinates), from CONV with both C = 0.0 and 27.89

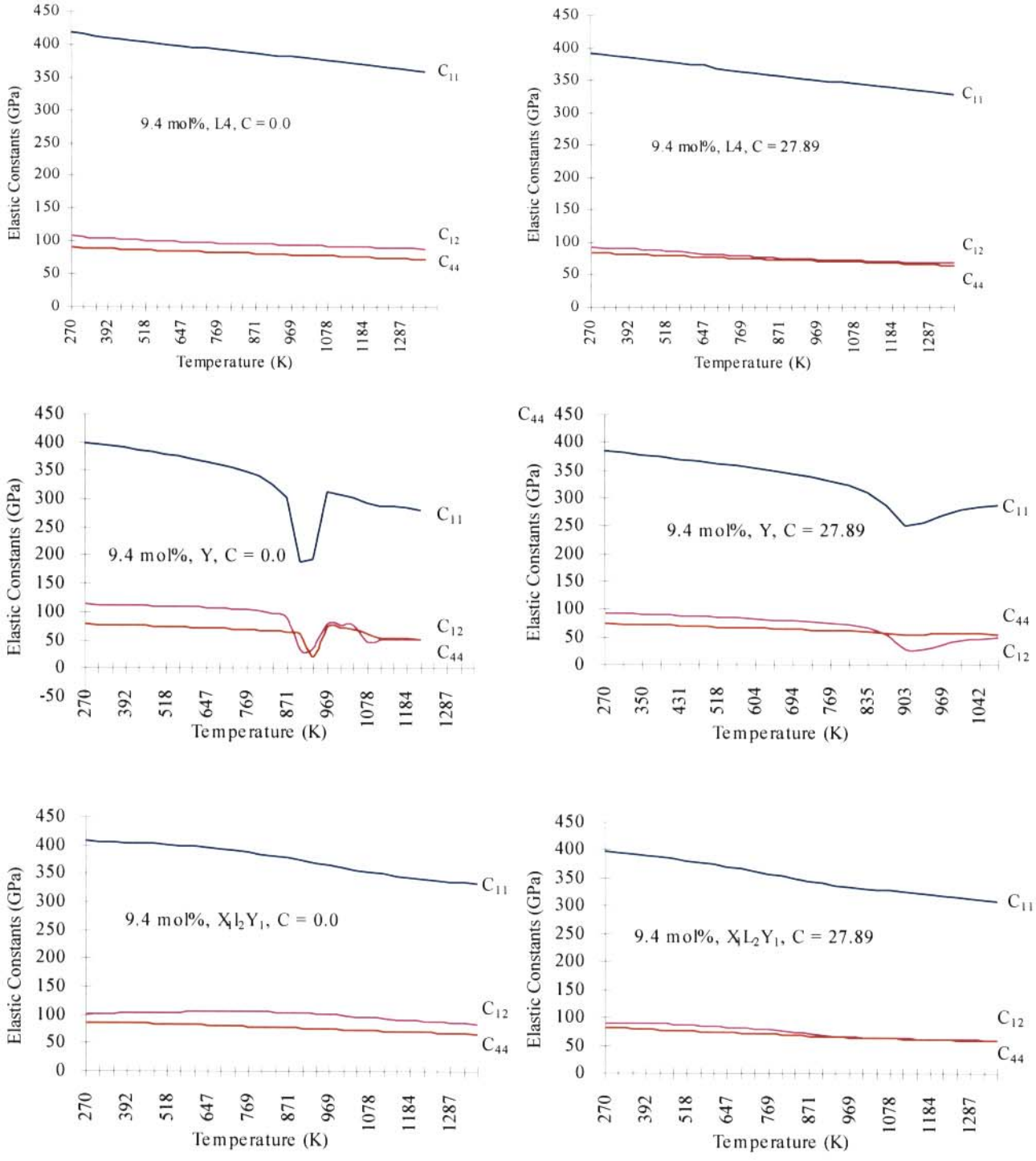

Figure 3.2.2.2(b) Temperature variation of all elastic constants for x = 9.4 from the L_4-, Y- and $X_1L_2Y_1$-configurations (relaxed co-ordinates), from CONV with both C = 0.0 and 27.89

The variation of elastic constants with temperature from relaxed coordinates is shown in figures 3.2.2.3 for the *x*-, *l*- and *y*-groups of configurations, with dopant concentration x = 24 and figure 3.2.2.4 for both x = 9.4 (L_4-configuration) and x = 24 (*l*-configuration). The *l*-configuration referred to here is a mixture of L_1-, L_2- and L_4-configurations. These configurations were used based on the consistent results obtained in terms of the magnitudes of the thermodynamic quantities (see table 3.2.2.2).

All the elastic constants in the x = 9.4 sample generally decreased linearly with temperature in the x = 9.4 sample for the X_1-configuration and with C = 0.0. The linear reductions were observed until about 1100 K, followed by deviations from linearity. In contrast, no apparent deviation was observed when C = 27.89. Near constant variation in C_{12} with increasing temperature was observed up to about 1100 K where a deviation from linearity was observed when C = 0.0. However, when C = 27.89, this elastic constant increased with increasing temperature with no sensitivity to T_c. Gradual decreases were observed in the case of C_{44} with no visible sensitivity to T_c. The results obtained with C = 27.89 generally showed no deviation from linearity and sensitivity to T_c.

Deviations from linearity were also observed in the Y-configuration (for x = 9.4), with C = 0.0, around 800 K, followed by a complete breakdown of the linear behaviour beyond 950 K. As for the results with C = 27.89, deviations from linearity were also observed around 800 K in both C_{11} and C_{12}. This was followed by a reversal of curvature around 900 K. On the other hand, C_{44} showed a gradual decrease with temperature and was insensitive to T_c.

Results from $X_1L_2Y_1$ showed linear reduction of all elastic constants with

temperature, except for C_{12} with $C = 0.0$ which increased with increasing temperature up to about 900 K, followed by a decrease with no sensitivity to T_c. Deviations from linearity were observed around 800 K. It was not possible to investigate this configuration in the $x = 24$ sample because the initial run at CONP, $C = 27.89$ failed to converge and hence there were no relaxed co-ordinates.

The elastic constants with the L_1-configuration and with $C = 0.0$ decreased linearly with temperature up to $T_c = 1300$ K, in agreement with experimental observations. However, C_{44} obtained with $C = 0.0$ and all elastic constants obtained with $C = 27.89$ appeared to be insensitive to T_c.

There were marked reductions in both C_{11} and C_{12} beyond 1000 K, followed by reversal of curvatures around T_c in the L_2-configuration and with $C = 0.0$ in the $x = 9.4$ sample. However, in the case of $C = 27.89$, erratic behaviour and reversal of curvature around 1200 K were observed in all elastic constants. As for the L_4-configuration, a linear reduction in all elastic constants was observed, with no visible deviation from linearity around T_c.

The calculated thermodynamic quantities for x = 24 with various configurations are shown in table 3.2.2.3(a)-(b). The variation in elastic constants is shown in figure 3.2.2.3 for the *x*-, *l*- and *y*-configurations. Unless otherwise stated, the calculations were performed with yttria ions located at NNN to oxygen vacancies.

Table 3.2.2.3(a) Results of the thermodynamic quantities for x = 24 with the X-, L-, Y- and $X_1L_2Y_1$-configurations from CONV, C = 0.0 with yttria ions located at NNN sites to the oxygen vacancies.

	Shell model thermodynamic quantities				
Configuration	C_{11} (GPa)	C_{12} (GPa)	C_{44} (GPa)	ϵ_0	ϵ_∞
X	354.8	94.26	89.42	15.71	2.297
L	365.5	117.7	102.8	17.62	2.299
Y	Did not converge				
$X_1L_2Y_1$	Did not converge				

Table 3.2.2.3(b) Results of the thermodynamic quantities for x = 24 with the X-, L-, Y- and $X_1L_2Y_1$-configurations from CONV, C = 27.89.

	Shell model thermodynamic quantities				
Configuration	C_{11} (GPa)	C_{12} (GPa)	C_{44} (GPa)	ϵ_0	ϵ_∞
X	330.2	89.67	73.94	18.14	2.297
L	Did not converge				
Y	328.2	85.02	83.68	17.22	2.300
$X_1L_2Y_1$	355.4	112.7	94.73	19.39	2.306

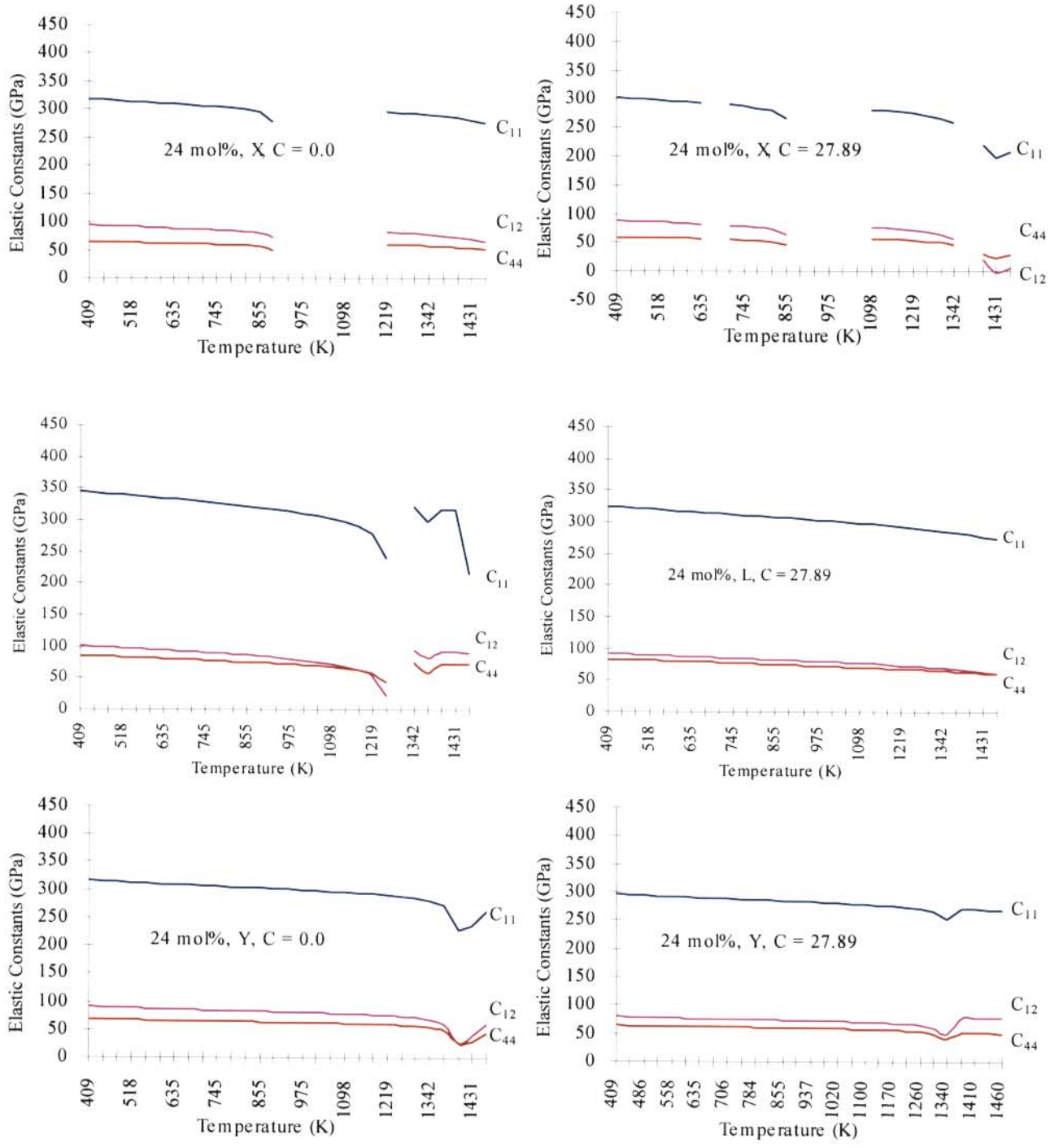

Figure 3.2.2.3 Temperature variation of all elastic constants for x = 24 from the *x*-, *l*- and *y*-configurations (relaxed co-ordinates), from CONV with both C = 0.0 and 27.89

There was a complete breakdown of linear reduction in the elastic constants versus temperature plot with the *x*-configuration for both C = 0.0 and C = 27.89. The breakdown occured around 900 K when C = 0.0 and at 600 K, 900 K and 1400 K when C = 27.98. In the *y*-configuration for the x = 24 sample, there was no indication of the departure from linearity. However, there was softening of elastic constants around 1400 K, followed by a reversal of curvature.

As for the *l*-configuration there was no departure from linearity before T_c = 1050 K. In fact, T_c was reproduced and the failure of the quasi - harmonic approximation was clearly reflected beyond T_c, when C = 0.0. However, when C = 27.89, there was no departure from linearity and the linear reduction in all elastic constants with temperature was insensitive to T_c. This clearly showed the tendency of the interionic potential model to be inconsistent when C = 27.89. Furthermore, the reversal of curvature in the plot of C_{11} versus temperature in the x = 24 sample was observed around 1300 K in both the *l*- and *y*-configurations. This is in agreement with observations by Botha *et al.* (1993).

Results for x = 15 and x = 21 are shown in table 3.2.2.4 from both C = 0.0 and C = 27.89. The corresponding temperature variation of elastic constants is shown in figure 3.2.2.5 from CONV with both C = 0.0 and C = 27.89. All the elastic constants in ZrO_2(15 mol% Y_2O_3), with C = 0.0, decreased linearly with temperature up to about 700 K, followed by a sharp decrease and a rapid increase at about 840 K (see figure 3.2.2.5). As for the C = 27.89 simulation runs, the deviations from linearity were observed at about 1100 K in both C_{11} and C_{12}. The elastic constant C_{44} did not show any such deviation.

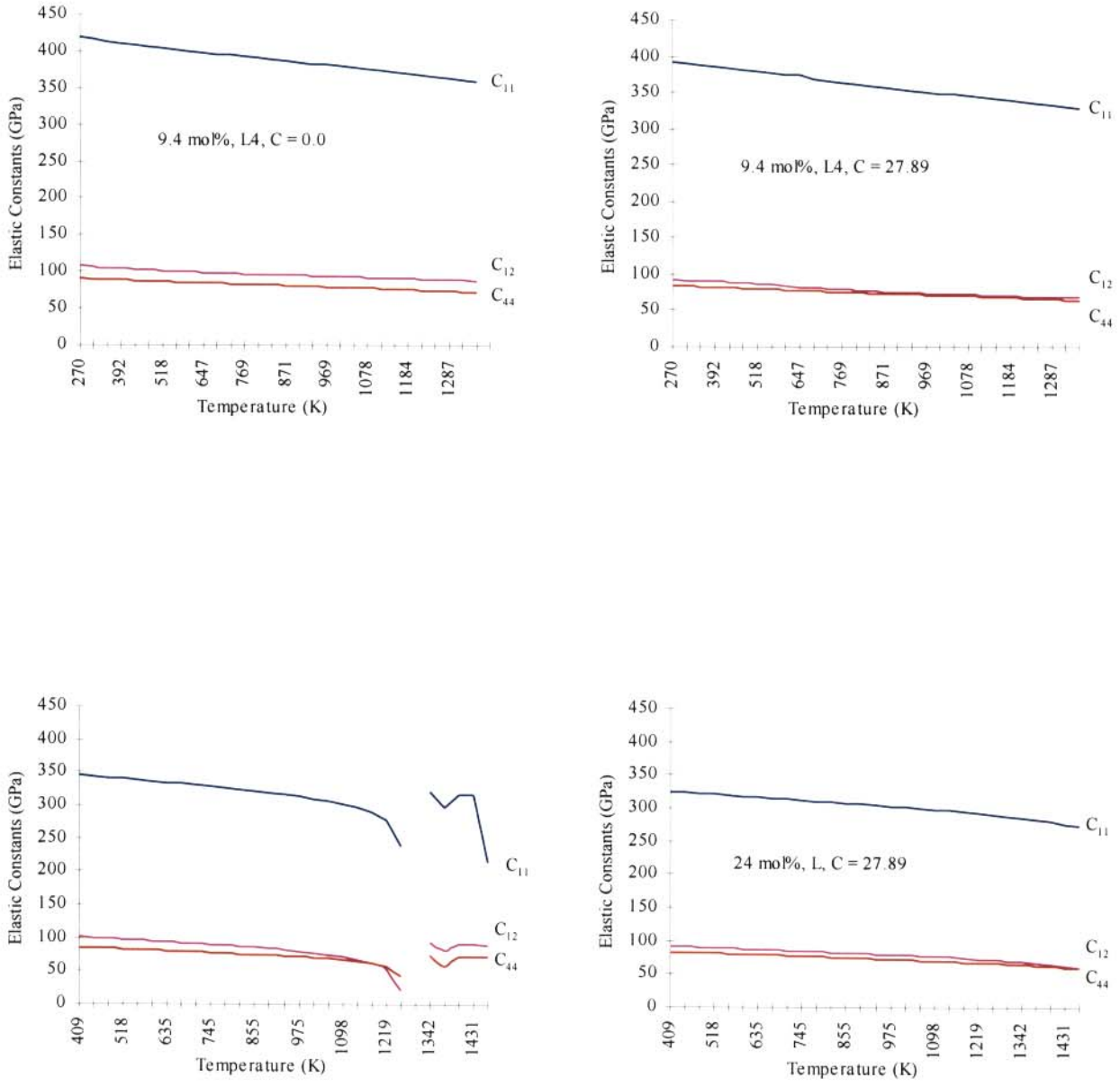

Figure 3.2.2.4 Temperature variation of all elastic constants for x = 9.4 and x = 24 from the *l*-configurations (relaxed co-ordinates), from CONV with both C = 0.0 and 27.89

Table 3.2.2.4(a) Results of elastic and dielectric constants for x = 15 and x = 21 with the *I*-configurations from CONV, C = 0.0.

	Shell model thermodynamic quantities				
Yttria content (mol%)	C_{11} (GPa)	C_{12} (GPa)	C_{44} (GPa)	ϵ_0	ϵ_∞
15	399.7	102.0	87.86	21.56	2.394
21	372.7	108.6	88.19	19.53	2.329

Table 3.2.2.4(b) Results of elastic and dielectric constants for x = 15 and x = 21 with the *I*-configurations from CONV, C = 27.89.

	Shell model thermodynamic quantities				
Yttria content (mol%)	C_{11} (GPa)	C_{12} (GPa)	C_{44} (GPa)	ϵ_0	ϵ_∞
15	351.3	103.2	70.03	30.78	2.399
21	354.4	94.01	84.07	18.99	2.333

On the otherhand, a quasi-linear behaviour was observed up to about 740 K from the x = 21 concentration with C = 27.89 (figure 3.2.2.5). However, with C = 0.0, the variation of elastic constants with temperature was found to be insensitive to the transition region, but instead, showed a continued linear reduction. This was not the case for the x = 15 concentration, where significant reductions were observed around 700 K.

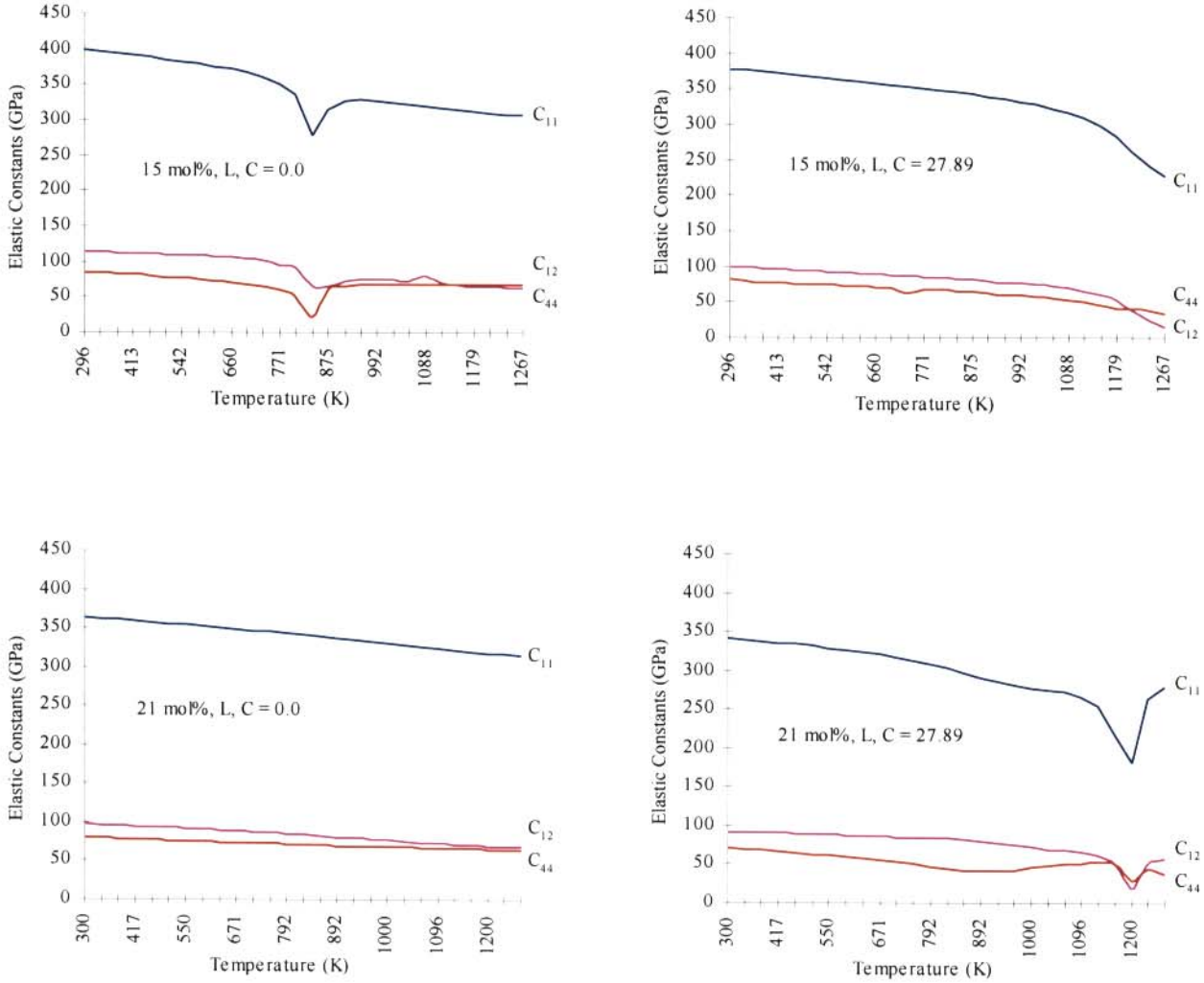

Figure 3.2.2.5 Temperature variation of all elastic constants for x = 15 and x = 21 from the *l*-configurations (relaxed co-ordinates), from CONV with both C = 0.0 and 27.89

It is difficult to draw a general conclusion on the effect of the inclusion of the van der Waals and dispersive interactions (C = 27.89) in the interionic potential model, but it would appear that the inclusion generally results in an erratic behaviour as well as departure from linearity. Furthermore, there were no experimental values of slopes for the x = 15 and x = 21, and as such, no comparisons with experimental values was made as was done in the case of the x = 9.4 and x = 24 concentrations.

On the basis of the consistency exhibited by the *I*-configurations, they were consequently chosen as structural entities on which the lattice stabilisation in the 15, 21 and 24 mol% concentrations were based. These clusters were subsequently used in molecular dynamics studies.

The temperature variation of the bulk moduli (B), the Cauchy relation failure (Δ or C in the graphs) and the anisotropy failure (A) for x = 9.4 and x = 24 are compared in figure 3.2.2.6. The bulk moduli for both the x = 9.4 (with the L_4-configuration) and x = 24 (with the *I*-configuration) concentrations decreased linearly with temperature, with no obvious strange behaviour around T_c = 1300K in ZrO_2(9.4 mol% Y_2O_3). In the x = 9.4 concentration, the magnitude of B was found to be large while the slope of B versus temperature plot was high compared with that from experiment (see table 3.2.2.8). Nonetheless, the behaviour of B was comparable with that from experiment (Botha *et al.* 1993) at high temperatures.

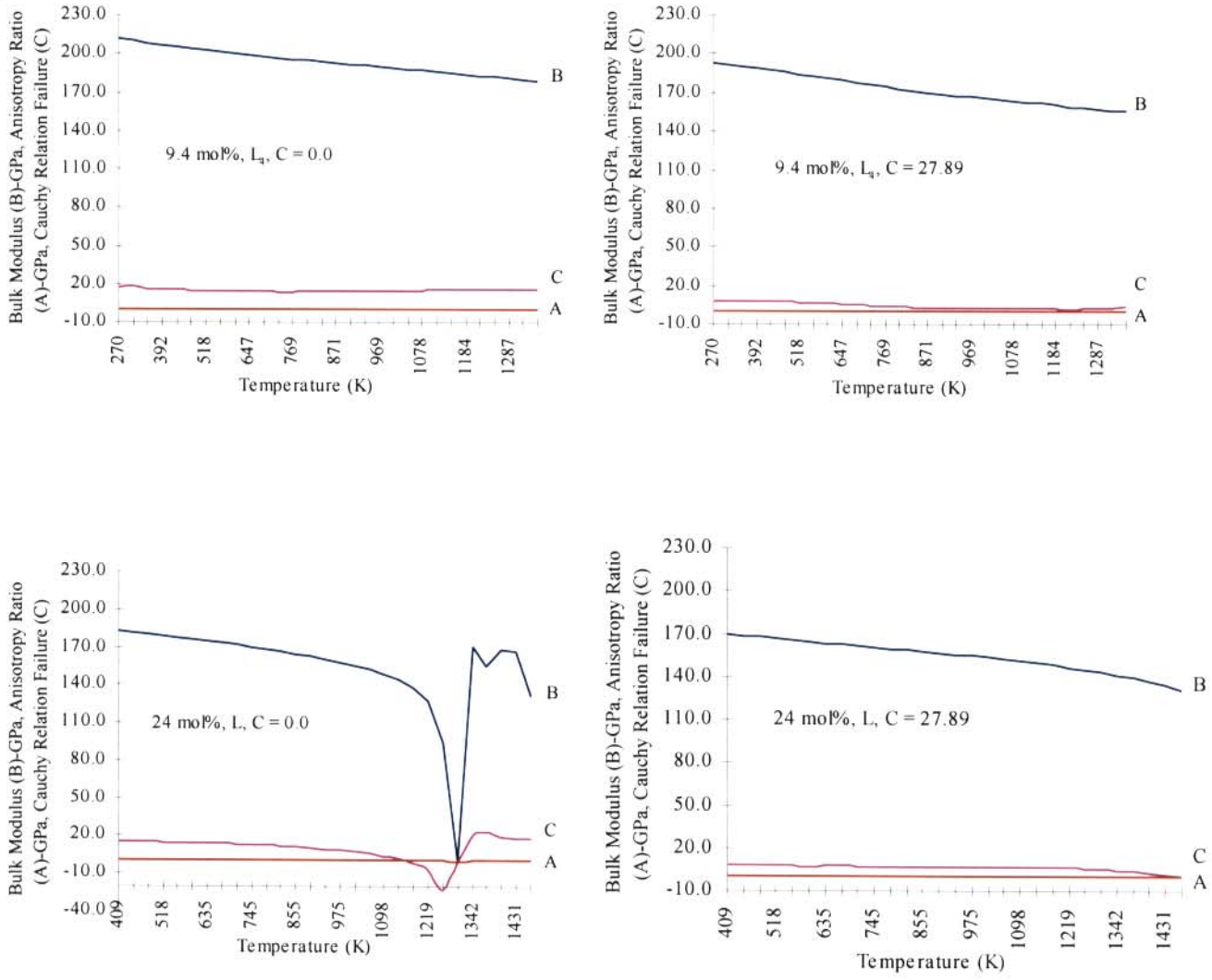

Figure 3.2.2.6 Temperature variation of bulk moduli, anisotropy ratios and Cauchy relation failures for x = 9.4 and x = 24 from the /-configurations (relaxed co-ordinates), from CONV with both C = 0.0 and 27.89

In ZrO_2(24 mol% Y_2O_3), and with $C = 0.0$, the bulk modulus showed a rapid decrease with temperature above about T_c. This was different from the behaviour from experiment (Botha *et al.* 1993) where a small increase followed by a decrease was observed. When $C = 27.89$ was used, only slight deviations from linearity in the behaviour of B occured above T_c. This was expected since the elastic constants were found to be insensitive to T_c and higher temperatures. However, the slope of B versus temperature compared very well with that from experiment (see table 3.2.2.8).

The corresponding Cauchy relation failure for $x = 9.4$ only began to slightly increase above about 800 K (figure 3.2.2.6) but continued to drop in ZrO_2(24 mol% Y_2O_3). However, the magnitudes of Δ were worse as compared with those from experiment when $C = 27.89$. Furthermore, experimental trends were not reproduciable. Comparing the behaviours of Δ for $x = 9.4$ and $x = 24$, coincidences at low temperatures were observed. However, separate behaviours were observed at high temperatures, wherein changes in Δ from the $x = 9.4$ concentration exceeded those from the 24 mol % yttria content.

The anisotropy ratio (figure 3.2.2.6) showed similar variations with those from experiment (Botha *et al.* 1993) in the high temperature region. When $C = 0.0$ then $A_{24} > A_{9.4}$, and both these ratios decreased with temperature up to below T_c in agreement with experiment (Botha *et al.* 1993). The magnitudes were comparable with those from experiment as well. However, when $C = 27.89$, the $x = 24$ reproduced experimental observation very well, and showed sensitivity to T_c. As for the 9.4 mol% yttria content, the linear reduction in A was found to be better than that observed in the case when $C = 0.0$.

Simulation runs were also made for oxygen vacancies sitting at NN distances for yttria cations. The various configurations that were used are shown in figure 3.2.2.7 while the results for the elastic and dielectric constants were calculated from CONV with both C = 0.0 and C = 27.89, and are given in table 3.2.2.5(a)-(b), respectively.

Following the suggestion by Veal *et al.* (1988) the structures with vacancies sitting at both NN and NNN positions to the yttria ions in the x = 24 concentration were investigated. The calculated values are reported in table 3.2.2.6(a)-(b). Slopes from the plots of the variation of all elastic constants with temperature for x = 9.4 and x = 24 are listed in table 3.2.2.7(a)-(d). The experimental values were determined from plots obtained from Brilluoin scattering experiments (Botha *et al.* 1993).

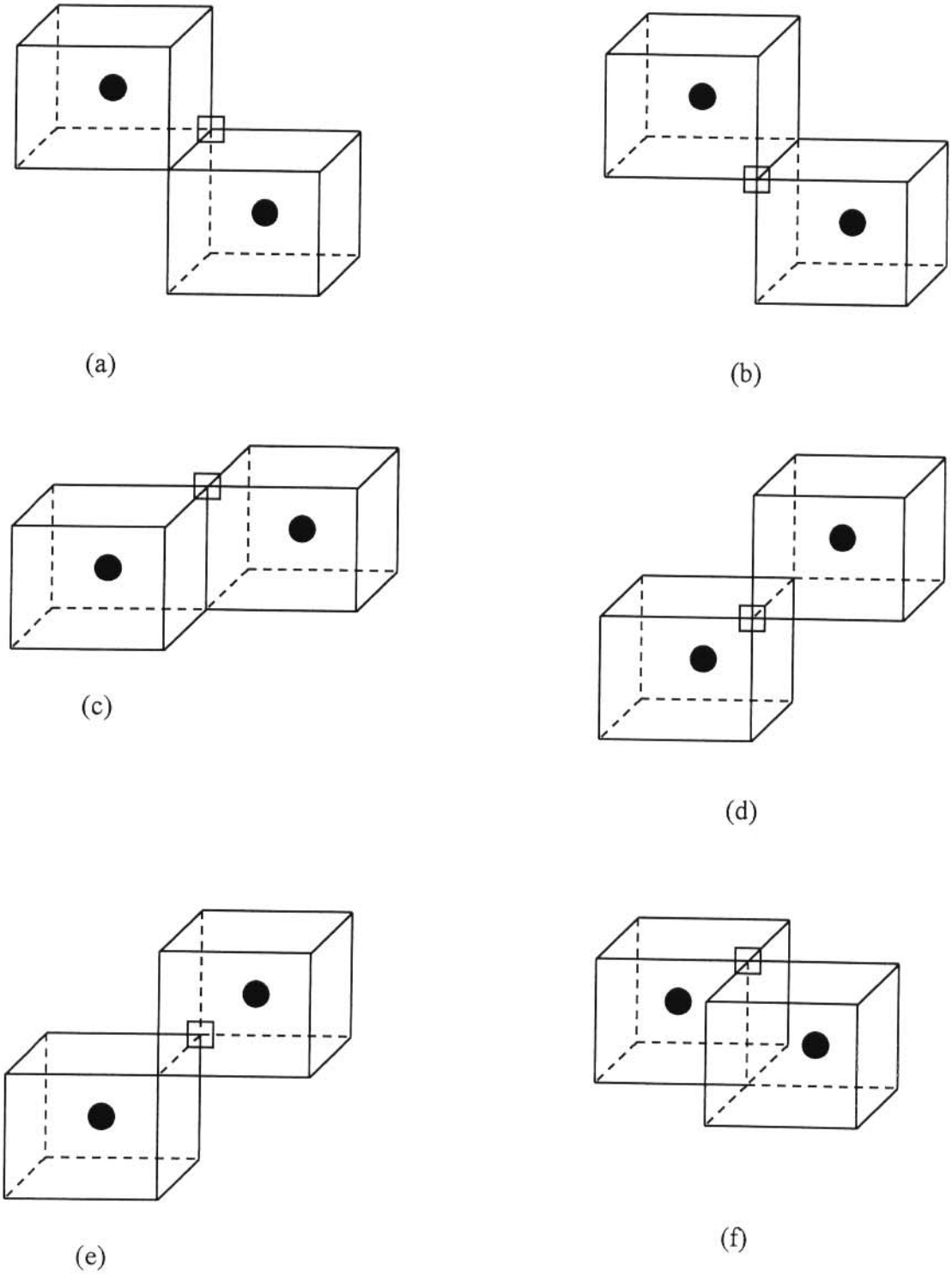

Figure 3.2.2.7 The various structure used for lattice stabilisation with Y^{3+} ions located at NN distances to the oxygen vacancies

Table 3.2.2.5(a) Results of elastic and dielectric constants for x = 9.4 with various defect positions from CONV, C = 0.0 and with Y^{3+} ions located at NN to the oxygen vacancies.

	Shell model thermodynamic quantities				
Cluster type	C_{11} (GPa)	C_{12} (GPa)	C_{44} (GPa)	ϵ_0	ϵ_∞
Fig 3.2.2.8(a)	428.3	119.6	96.44	24.24	2.458
Fig 3.2.2.8(b)	448.5	131.2	89.54	24.47	2.473
Fig 3.2.2.8(c)	420.9	112.4	87.37	25.26	2.466
Fig 3.2.2.8(d)	Did not converge				
Fig 3.2.2.8(e)	395.3	136.1	85.36	26.13	2.468
Fig 3.2.2.8(f)	357.1	79.56	86.71	26.46	2.464

Table 3.2.2.5(b) Results of elastic and dielectric constants for x = 9.4 with various defect positions from CONV, C = 27.89 and with Y^{3+} ions located at NN to the oxygen vacancies.

	Shell model thermodynamic quantities				
Cluster type	C_{11} (GPa)	C_{12} (GPa)	C_{44} (GPa)	ϵ_0	ϵ_∞
Fig 3.2.2.8(a)	426.7	105.4	-44.5	98.27	2.473
Fig 3.2.2.8(b)	398.6	91.54	81.38	28.00	2.473
Fig 3.2.2.8(c)	Did not converge				
Fig 3.2.2.8(d)	396.2	85.04	74.14	26.58	2.463
Fig 3.2.2.8(e)	401.6	97.50	77.20	30.31	2.473
Fig 3.2.2.8(f)	373.0	90.34	86.52	23.64	2.472

Table 3.2.2.6(a) Results of elastic and dielectric constants for x = 24 with various defect clusters from CONV, C = 0.0 and with Y^{3+} ions located at both NNN and NN to the oxygen vacancies.

	Shell model thermodynamic quantities				
Configuration	C_{11} (GPa)	C_{12} (GPa)	C_{44} (GPa)	ϵ_0	ϵ_∞
NNN(7L), 1NN	366.5	119.3	97.82	18.22	2.303
NNN(6L), 2NN	367.7	113.2	97.99	18.70	2.306
NNN(5L), 3NN	332.0	94.17	91.90	20.78	2.306
NNN(4L), 4NN	355.9	114.1	91.54	20.51	2.306

Table 3.2.2.6(b) Results of elastic and dielectric constants for x = 24 with various defect clusters from CONV, C = 27.89 and with Y^{3+} ions located at both NNN and NN to the oxygen vacancies.

	Shell model thermodynamic quantities				
Configuration	C_{11} (GPa)	C_{12} (GPa)	C_{44} (GPa)	ϵ_0	ϵ_∞
NNN(7L), 1NN	335.5	93.60	86.79	19.29	2.306
NNN(6L), 2NN	346.8	108.2	84.02	19.74	2.309
NNN(5L), 3NN	219.5	63.18	81.00	21.62	2.309
NNN(4L), 4NN	348.5	114.3	85.13	22.01	2.312

Table 3.2.2.7(a) Experimental slopes from the variation of all elastic constants with temperature (taken from plots by Botha *et al.* 1993).

Experimental slopes of variation of C_{ij} with temp. (GPa/K)					
Yttria content (mol%)					
9.4			24		
Elastic constant (GPa)			Elastic constant (GPa)		
C_{11}	C_{12}	C_{44}	C_{11}	C_{12}	C_{44}
0.050	0.024	0.012	0.055	0.036	0.020

Temperature gradients with random clusters for all the elastic constants were calculated by Hlungwani (1996) to be 0.125, 0.010 and 0.033 for the x = 9.4 sample. The corresponsing values in the x = 24 concentration were 0.036, 0.015 and 0.019.

Table 3.2.2.7(b) Calculated slopes from the variation of all elastic constants with temperature for x = 9.4 and with both C = 0.0 and C = 27.89.

Calculated slopes of variation of C_{ij} with temp. (GPa/K)						
	9.4 mol%					
	C = 0.0			C = 27.89		
	Elastic constant (GPa)			Elastic constant (GPa)		
Config.	C_{11}	C_{12}	C_{44}	C_{11}	C_{12}	C_{44}
X_1	0.030	0.010	0.015	0.010	0.020	0.020
Y	0.091	0.017	0.022	0.012	0.039	0.026
$X_1L_2Y_1$	0.036	0.015	0.012	0.099	0.029	0.019

Table 3.2.2.7(c) Calculated slopes from the variation of all elastic constants with temperature for x = 9.4 and with both C = 0.0 and C = 27.89 with the *I*-shape configuration.

Calculated slopes of variation of C_{ij} with temp. (GPa/K)						
	9.4 mol%					
	C = 0.0			C = 27.89		
	Elastic constant (GPa)			Elastic constant (GPa)		
Config.	C_{11}	C_{12}	C_{44}	C_{11}	C_{12}	C_{44}
L	-	-	-			
L_1	0.050	0.013	0.016			
L_2	0.066	0.004	0.022			
L_3	0.108	0.047	0.035			
L_4	0.051	0.021	0.015	0.059	0.029	0.019
L_5	0.089		0.024			

Slopes of variation of elastic constants with temperature for calculations with C = 27.89 were only determined for the L_4-configuration.

Table 3.2.2.7(d) Calculated slopes from the variation of all elastic constants with temperature for x = 24 and with both C = 0.0 and C = 27.89.

Calculated slopes of variation of C_{ij} with temp. (GPa/K)						
	24 mol%					
	C = 0.0			C = 27.89		
	Elastic constant (GPa)			Elastic constant (GPa)		
Config.	C_{11}	C_{12}	C_{44}	C_{11}	C_{12}	C_{44}
x	0.037	0.025	0.013	0.056	0.034	0.024
I	0.055	0.032	0.024	0.056	0.028	0.028
y	0.031	0.017	0.0091	0.028	0.019	0.009

Calculations of slopes in the x = 24 sample with the X-cluster were carried over a short linear region and hence the results shown in table 3.2.2.7(d) are not over the same range of linear regions used in the other clusters.

Comparison of experimental slopes from temperature dependences of elastic constants with the calculated slopes (table 3.2.2.7(a)-(c)) showed that slopes from the L_4-configuration were closest. It was for these reason that in figure 3.2.2.4 only the behaviour of the elastic constants obtained from the L_4-configuration was compared with that from the 24 mol% Y_2O_3 concentration. It was found that experimental slopes agreed reasonably well with slopes from the present computer simulation studies for x = 24 with the *I*-configuration, especially when C = 0.0.

Slopes of variation of bulk modulus with temperature were compared with those from experiment (Botha *et al.* 1993) in table 3.2.2.8. This was done only in the linear region (T = 452 - 678K) in the x = 9.4 concentration.

Table 3.2.2.8 Comparison of experimental and calculated slopes of variation of bulk modulus (B) with temperature for x = 9.4 and x = 24.

Quantity(GPa/K)	Calculated	Experimental
$\frac{dB}{dT}_{9.4}$	0.028	0.033
$\frac{dB}{dT}_{24}$	0.040	0.042

The results from the x = 24 concentration were generally comparable with those from experiment.

3.3 DISCUSSIONS

In this section the various results obtained from static lattice simulation methods are discussed. Results from defect energy calculations are discussed first, followed by those from perfect lattice calculations. This section is ended with a brief summary of the major observations made.

In view of the fact that various configurations with different orientations of oxygen vacancies with respect to the yttria ions were used, a holistic approach for picking on the best configuration was adopted. In terms of the approach the following criteria had to be met: (a) both the rigid-ion and shell model had to reproduce the elastic and dielectric constants, (b) the linear reduction of the elastic constants with increasing temperature had to be both consistent and obvious, (c) the slopes from the plots of the variation of elastic constants with temperature had to agree with those from the experimental work by Botha *et al.* (1993) and (d) the model had to yield defect energies that agree with experimental values. The configuration that yielded the best results was subsequently used in the construction of supercells for molecular dynamics calculations.

3.3.1 DEFECT ENERGY CALCULATIONS

The calculated anion interstitial and vacancy formation energies (table 3.1.2.1) were comparable with those obtained by Dwivedi and Cormack (1990) in calcia-stabilised cubic zirconia. Furthermore, the anion interstitial formation energy was found to be larger than the corresponding anion vacancy formation energy. This seems to suggest that anion vacancies would be readily formed as compared to interstitial defects.

The anion vacancy activation energy was found to be smaller than the anion

interstitial activation energy for both $x = 9.4$ and $x = 24$, indicating the preference for vacancy motion. This observation will be used to explain molecular dynamics results in the next chapter. Activation energies with $C = 0.0$ appear to be more reasonable. Our values agreed with those from experiment (Solier *et al.* 1988) in the $x = 9.4$ concentration, as well as comparable to results by Dwivedi and Cormack (1990) on calcia-stabilised cubic zirconia. The results by Dwivedi and Cormack (1990) contained a contribution from the association energy, as was the case in the present work. Further studies need to be undertaken to understand the defect interactions in high yttria content samples.

The calculated anion activation energies were greater than those in fluorine conducting solids (CaF_2, SrF_2, BaF_2, and $SrCl_2$) reported by Catlow *et al.* (1977) and UO_2 (Walker and Catlow 1981). Their values were around 0.2 eV while the calculated values in the present investigation were in excess of 0.6 eV. This seems to suggest that it is easier to generate defects in fluorine ion conducting materials than it is in oxygen conducting systems such as yttria-stabilised cubic zirconia.

Furthermore, the anion vacancy activation energy was observed to decrease linearly with temperature up to about 800 K, followed by a more dramatic decrease up to about 1300 K, which is the transition temperature to the fast-ion phase in the 9.4 mol% Y_2O_3 concentration (Ngoepe 1987, Botha *et al.* 1993). Further pronounced decreases in the anion vacancy activation energy was observed beyond $T_c = 1300$ K. High temperature ionic conductivity measurements show an anomaly near T_c (Tien and Subbarao 1963, Suzuki *et al.* 1981). These results suggested rapid diffusion accompanied by a reduction in activation energy at T_c. The deviation from linearity above 800 K is attributed to the fact that 9.4 mol% is at the lower extreme of the minimum amount of Y_2O_3 required to fully stabilise pure zirconia in

the cubic phase, then there could be tendencies for cubic-tetrahedral transitions to occur, as observed by Andersen *et al.* (1993). The above results are in agreement with experimental results on a range of yttria-stabilised cubic zirconias (Suzuki *et al.* 1981) and calcia-stabilised samples (Tien and Subbarao 1963) where the activation energies were found to decrease at high temperatures.

The energies of isolated defects in ZrO_2(24 mol% Y_2O_3) were generally higher than those in ZrO_2(9.4 mol% Y_2O_3). This may be related to the formation of larger defect aggregates in the former, in which the various isolated, ionic species were strongly bound to the aggregates, thus requiring higher energies of dissociation. It is possible that such high energies of isolated defects, especially $E_{V_O^{\cdot\cdot}}$, together with the fact that the anion vacancy activation energy when $x = 24$ is higher than that for $x = 9.4$ (table 3.1.2.3(b)), would be responsible for poor anionic conduction in the $x = 24$ concentration. However, based on the lower calculated value for interstitial activation energy in the $x = 24$, it is possible that interstitials could be contributing to the conduction process as well.

The association energies with the yttria ions at NNN positions to the oxygen vacancy were found to be negative indicating the possibility of formation of the $[Y'_{Zr} \cdot V_O^{\cdot\cdot} \cdot Y'_{Zr}]^x$ associate. This preferential sitting of the dopant cations at NNN sites to the oxygen vacancies is consistent with previous EXAFS studies by Veal *et al.* (1988) and Catlow *et al.* (1986) as well as computer simulation studies on calcia-stabilised cubic zirconia (Dwivedi and Cormack 1990). The association energy for clusters of type $[Y'_{Zr} \cdot V_O^{\cdot\cdot} \cdot Y'_{Zr}]^x$, with the charge compensating defects in NN positions to the dopant cation (figure 3.1.2.4(b)), could not be calculated because this structure failed to converge. This seems to suggest that the existence

of such a cluster in yttria-stabilised cubic zirconia is doubtful, in agreement with results from the computer simulation studies by Dwivedi and Cormack (1990).

The activation energy has been found to be the sum of the saddle-point energy and half the association energy (Dwivedi and Cormack 1990). Using this argument the low and high temperature activation energies were calculated to be 1.0413 and 0.887 (see table 3.1.2.6), respectively, which were close to the corresponding experimental values of about 1.1 eV (Etsell and Flengas 1970, Suemoto and Ishigame 1986, Oishi and Ando 1984, Solier *et al.* 1989) and 0.84 eV (Solier *et al.* 1989), respectively. Based on the magnitudes of the activation energies, it was inferred that rapid diffusion would occur at high temperatures while low oxygen migrations occur at low temperatures.

It is generally accepted (Etsell and Flengas 1970, Dwivedi and Cormack 1990, Tien and Subbarao 1963, Suemoto and Ishigame 1986, Hutchings *et al.* 1983, 1985) that highly mobile oxygen vacancies are responsible for conductivity in doped zirconia. Although the addition of 12 mol% CaO to ZrO_2 produces 6% anion vacancies compared with only 4.1% upon addition of 9 mol% Y_2O_3 to ZrO_2, the latter electrolyte is twice as conductive at $1000^{\circ}C$ (Etsell and Flengas 1970). This may be understood in terms of lower binding energies obtained with C = 0.0 (table 3.1.2.4(a)) for Y'_{Zr} - $V_o^{\cdot\cdot}$ - Y'_{Zr} associates as compared with that of Ca''_{Zr} - $V_o^{\cdot\cdot}$ associates (see table 3.1.2.5) reported by Dwivedi and Cormack (1990).

Following computer simulation studies on calcia-stabilised cubic zirconia (Dwivedi and Cormack 1990), in which the intrinsic disorder was found to be of Schottky type, the defect clusters involving zirconia vacancies in yttria-stabilised cubic zirconia were investigated. Defect clusters with C = 0.0 were found to be

unbound with respect to isolated point defects but bound when C = 27.89 though only for the neutral cluster. However, because of the high formation energy of V''''_{Zr} (table 3.1.2.7), the existence of these type of clusters in pure zirconia is doubtful.

3.3.2 PERFECT LATTICE CALCULATIONS

The temperature variations of the complete set of elastic constants were determined for ZrO_2(x mol% Y_2O_3), with x = 9.4 and x = 24. These concentrations are near the extremes of the range normally encountered in yttria-stabilised cubic zirconia. The x = 9.4 is close to the minimum yttrium concentration (x = 8) required to stabilise pure ZrO_2 from tetragonal to cubic phase. For the x = 24, the cubic phase is quite stable, and strong defect repulsive interactions were reported, particularly at high temperatures (Ngoepe and Comins 1987). In the current studies extensive calculations of temperature dependence of elastic constants were carried out on these two dopant concentrations in order to make comparisons with the experimental results by Botha *et al.* (1993) and Hart *et al.* (1986).

The experimental temperature dependence of elastic constants has two regions of interest: the linear decrease in all elastic constants up to a characteristic transition temperature T_c (region 1) followed by anomalous behaviour in certain elastic constants (Botha *et al.* 1993, Ngoepe and Comins 1987, Ngoepe 1987) characterised by deviations from linearity (region 2). The quasi-linear decrease in all elastic constants below T_c is ascribed to lattice anharmonicity associated with thermal expansion (Garber and Granato 1975). Although calculated results from some configurations do not exhibit the expected experimental behaviour, particularly in region 2 where the quasi-harmonic approximation fails, the interest in the present investigation is in region 1.

Firstly the results of ZrO_2(9.4 mol% Y_2O_3) will be discussed and three categories of cluster configurations will be considered. The first category represents all those configurations that least reproduced the linear temperature variation of elastic constants (i.e. X-, X_2-, L-, L_3- and L_5-configurations), while configurations that reproduced the linear behaviour up to about 800 K (i.e. X_1-, L_2- and Y-configurations) belong to the second category. The third category comprise all those configurations that reproduced the linear reduction in all elastic constants up to below T_c, i.e. L_1 and L_4-configurations. Configurations in these categories will further be assessed on how closely they reproduce magnitudes of experimental temperature gradients of elastic constants and prediction of elastic constants behaviour above T_c.

The first category of configurations failed to reproduce experimental linear reduction of elastic constants well below 800 K, and this rendered accurate determination of the temperature slopes of elastic constants difficult (except for the L-configuration which did not show any observable deviation from linearity). In certain configurations this linear behaviour was observed after a slight increase at lower temperatures, particularly in C_{11}. Also, in certain instances C_{12} and C_{44} failed to decrease as expected. The temperature gradients of elastic constants, where calculated, differed to a large extent with those from experiment. Schematic diagrams of supercells with 93 ions, representing configurations in this category, show an even distribution of dopant vacancy clusters throughout the cell, hence suggesting minimal cluster cluster interaction. Furthermore, the failure of the first category to reproduce the linear reduction of elastic constants could be ascribed to cubic tretragonal distortions at low yttria concentrations and also explained in terms of the results from the high temperature coherent diffuse neutron scattering work by Hull *et al.* (1988) where two distinct regions were identified: a relatively vacancy

free tetragonally distorted region and a region in which there are vacancies and aggregates of vacancy pairs with a range of sizes, suggesting that cubic stabilisation is associated with the existence of the two regions.

The second category of configurations generally yields a linear variation of elastic constants up to about 800 K, well below T_c which occurs at 1300K. The magnitude of temperature gradients of elastic constants are closer to experimental values than in the first category. A closer examination of schematic diagrams of associated supercells indicates uneven distribution of defect clusters. Certain regions within the cell contain aggregates of clusters while others are almost defect free. A similar behaviour involving termination of a linear variation of elastic constants well below T_c was noted in LaF_3 (Ngoepe and Parker 1992) and was ascribed to failure of interatomic potentials to predict such changes. However, in LaF_3 the slope of the temperature variation of elastic constants was accurately reproduced below 800K, which is not the case in configurations of the second category. Hence a different mechanism, perhaps cubic-tetragonal transitions and structural instabilities (Andersen *et al* 1986) could account for this failure.

In the third category, made up of L_1- and L_4-configurations, the linear decrease of elastic constants with temperature was well reproduced up to T_c. The temperature gradients of elastic constants compared favourably with experimental results of Botha *et al.* (1993). Since the L_4-configuration provides best agreement with experimental observations on all elastic constants, it warrants a closer attention. It is surmised, from the schematic diagram of its supercell, that the arrangement of defect clusters play a crucial role: two clusters, each consisting of one oxygen vacancy and two yttria ions, were positioned close to each other and spanned one "plane", located a third way from the top of the supercell. A third cluster was almost

at the bottom of the cell. This arrangement tends to optimise Y^{3+}-Y^{3+} interactions of adjacent clusters. The onset of deviation of elastic constants from linearity above T_c was consistent with observations from experiment (Botha *et al.* 1993, Ngoepe 1987). However, magnitudes of changes were inaccurate since the quasi-harmonic approximation is inadequate for predicting large changes of elastic constants associated with the fastion phase. The reproduction of experimental observations in L_4-configuration could be explained in terms of the experimental results from neutron scattering (Hull *et al.* 1988) where two distinct regions, one defect free and the other comprising vacancies and aggregates of vacancy pairs, were observed. It was infered that the presence of the two regions suggested the stabilisation of the cubic phase. These two regions are noted in the L_4 - configuration. The failure of other L - shaped configuration to reproduce the experimental results (see table 3.2.2.7(c)) could be ascribed to the absence of such regions. Thus, it appears that when supercells are constructed such that two distinct regions are created, following the *I* - shape cluster, experimental observations are reproduced. However, as mentioned earlier these observations are still speculative and systematic investigation needs to be carried out.

We now discuss the magnitudes of the thermodynamic quantities. The magnitudes of elastic constants, particularly with C = 0.0 in shell model simulation runs and with the rigid-ion model, show deviations from from experimental values. However, experimental results were better reproduced when the dopant cations were located at NNN sites to the oxygen vacancies. This preferential sitting of yttria ions at NNN to the vacancies is consistent with EXAFS studies (Veal *et al.* 1988) and computer simulation studies (Dwivedi and Cormack 1990). The best results were also obtained with CONV, when C = 27.89, showing the role played by the dispersive forces when magnitudes of elastic constants are sought. This inclusion tended to

lower the magnitudes of the elastic constants, thereby bringing the calculated values in close agreement with those from experiment.

Elastic constants in certain configurations could not be determined as these structures failed to converge. It is possible that these are configurations in which the yttria ions were forced to have a sevenfold coordination, leading to the prevalence of strong vacancy-vacancy interactions. This is in agreement with observations by Subbarao and Ramakrishnan (1979) and Dwivedi and Cormack (1990).

We now consider behaviour of elastic properties associated with high concentration of yttrium oxide (x = 24 mol%). For the *x*-shaped cluster configurations, the linear decrease of elastic constants occurred up to 800K well below T_c ($\simeq$ 1050K). Although temperature gradients of elastic constants were reasonable, they differed from experimental values. A similar behaviour was noted in configurations of the second category for x = 9.4 mol%. The reasonableness of such results were partly attributable to cluster-cluster interactions, which could be applicable to the x = 24 mol % compounds where such interactions are enhanced by a higher dopant concentration. The configuration associated with the *y*-shaped clusters, reproduced the linear region well, but overestimated T_c. Furthermore, the magnitudes of temperature gradients were significantly underestimated. Since the cubic phase is stable at x = 24 mol%, failure to predict accurate temperature gradients of elastic constants and T_c, by related configurations, could be inherent in the nature of the *x* and *y*-shaped clusters.

Finally, the *I*-shaped configuration yielded linear changes of elastic constants, the transition temperature ($T_c \simeq 1050$K) and the temperature slopes of elastic constants

were consistent with experimental results (Botha *et al* 1993). Although T_c was accurately predicted, the temperature gradients in the fastion phase were not well reproduced. A similar behaviour was also reflected by the third category of configurations with *I*-shaped clusters, in the x = 9.4 mol% sample, and mechanisms suggested there are equally applicable. The agreement further suggests that configurations with *I*-shaped clusters, where such clusters interact strongly, are preferable at both extreme concentrations of yttrium concentration, i.e. 9.4 and 24 mol%.

In order to broaden the scope of our studies, calculations were also carried out on configurations with different types of clusters. Firstly configurations with mixed types of clusters (X, Y, and L clusters in one supercell) were considered for both the x = 9.4 and x = 24 mol% concentrations. These clusters reproduced the linear reduction of elastic constants but failed to reproduce the magnitudes of the elastic constants. The recent studies by Hlungwani and Ngoepe (1996) have shown that configurations in which the orientation of clusters are disregarded, i.e. where dopants and oxygen vacancies are distributed randomly, give results that differ substantially from experimental values.

The magnitudes of the thermodynamic properties and temperature gradients with *I*-shaped clusters in x = 9.4 and x = 24 generally agreed with those from experiment for all the three elastic constants. The model further reproduced increased slopes of all elastic constants at 24 mol% Y_2O_3 very well. Results emanating from the other clusters deviated significantly from experimental values, the extreme case being where vacancies and dopants are randomly distributed in supercells as evidenced by computer simulation results on random clusters (Hlungwani 1996).

The lack of experimental temperature gradients of elastic constants for intermediate concentrations, x = 15 and x = 21, restricted objective validation of the associated types of clusters. However, on account of the good results obtained from the *I*-configurations, simulation runs were consequently performed only with the *I*-configuration. The reproduction of the linear region was also ascribed to lattice anharmonicity associated with thermal expansion.

Results from perfect lattice calculations with oxygen vacancies located at NN sites to yttria ions, with x = 9.4, showed that in general C = 0.0 yielded more consistent values of both the elastic and dielectric constants. As for the x = 24 concentration with a mixture of vacancies, some at NNN while others at NN to the dopant cations, the results seemed to suggest that a high proportion of vacancies at NNN sites was unfavourable but failed to show an optimum concentration (see table 3.2.2.5(a)-(b)). Thus, it is possible that a mixture of such clusters could yield favourable results as suggested by Veal *et al.* (1988). However, more calculations have to be done.

A comparison of the calculated high temperature dependence of the thermodynamic quanties, Bulk Modulus (B), Anisotropy Ratio (A), and Cauchy Relation Failure (Δ), in x = 9.4 and x = 24 with experimental results appears reasonable. This is particularly the case with the bulk moduli results.

The following were the major observations made in this chapter:

(a) Anion vacancy motion was found to be preferable on account of the lower calculated activation energy.

(b) Negative association energies were found in the case where the oxygen vacancies were located at NNN sites to the yttria ions. These association

energies show the possibility of formation of the clusters.

(c) The *I*-configuration yielded better results in general, and showed that the charge compensating oxygen vacancies were preferentially located at NNN sites to the dopant cations. This is consistent with the observation highlighted in point (b) above.

(d) Better thermodynamic quantities were consistently obtained when C = 27.89, highlighting the importance of the van der Waals and dispersive interactions when only the magnitudes on the elastic constants are sought.

(f) The temperature gradients of the elastic constants generally agreed with those from experiment for certain types of clusters. The differences at the 9.4 mol% concentration among various clusters is attributed to instabilities associated with the minimum stabilisation of the cubic phase.

(g) The linear reduction of elastic constants with temperature occurred up to the respective transition temperature only in certain configurations. This could be related to the types of defect orientations in these configurations.

(h) There appears to be a relationship between the orientation of the defects and reproduction of experimental results and properties. The optimal situation seemed to be the location of two pairs of dopant cations in one plane and the third pair positioned in the alternate "plane", as in the L_4-configuration. However, more work needs to be done before a conclusive argument can be advanced.

i) The bulk moduli results were reasonable when compared with experimental results for both the x = 9.4 and x = 24 mol%.

CHAPTER 4

MOLECULAR DYNAMICS CALCULATIONS

In previous molecular dynamics (MD) studies dopant charge compensating vacancy complexes in yttria stabilised cubic zirconia were chosen more randomly. Our energy minimisation calculations in Chapter 3 (section 3.4.2) have shown that the *l*-shaped vacancy dopant clusters yields better results of themodynamic quantities. Consequently, this type of configuration was used as the structural entity on which supercells for MD calculations were based. The key reasons for adopting the *l*-shaped cluster are the following:

1. Reproduction of the magnitudes of the thermodynamic quantities
2. The linear reduction of all elastic constants with temperature, below T_c, was reproduced
3. The temperature gradients of the elastic constants generally compared well with experimental results
4. The reproduction of experimental results is valid for the two extreme concentrations, x = 9.4 and 24.

In this chapter results from molecular dynamics studies are presented. MD allows for the calculation of properties of the material above T_c, which is not possible in perfect lattice or defect energy calculations. Results of anion transport and structural properties in ZrO_2(x mol% Y_2O_3), with x = 9.4, 15, 21 and 24, are presented for various temperatures. The structural properties were obtained from the radial distribution functions. The various results are discussed in section 4.3.

4.1 COMPUTATIONAL PROCEDURE

The FUNGUS (see section 2.3.3) computer program was used for the simulation of ion transport properties reported in this chapter. This is a general purpose program that may be applied to crystals of any symmetry.

Although a conventional fluorite-structured unit cell contains 96 ions, supercells containing 8 unit cells were used for adequate statistics. Calculations were performed on systems containing 744, 728, 712 and 704 ions, corresponding to the four concentrations x = 9.4, 15, 21 and 24. The number of species are shown for the four concentrations in table 4.1.1.

The rigid-ion potential parameters used in molecular dynamics simulations were similar to those used in perfect lattice and defect energy calculations (table 3.1.1.2(a)-(b)). The rigid-ion potentials can reliably model structural and ion transport mechanisms and the idea of their validity is seen in tables 3.2.2.1(a)-(d) and 3.2.2.6 where the calculated elastic and dielectric constants were compared with experimental values.

Table 4.1.1 Number of ions in 8-unit cells supercells

	Number of different species			
Yttria content (mol %)	Zr^{4+}	Y^{3+}	O^{2-}	$V_O^{\cdot\cdot}$
9.4	208	48	488	24
15	179	77	474	38
21	148	108	458	54
24	133	123	451	61

A time step of 5×10^{-15} s and potential cutoff of 1.89×10^{-10}m were used. The time step is sufficiently shorter than any important process in the system such as the period of ionic vibration. Coordinates corresponding to crystallographically determined structure were assigned to particles. A problem inherent in this approach is that the ions gain potential energy and loses kinetic energy when drifting away from the lattice sites, resulting in about 1000 time steps taken in achieving a correct distribution of energy between potential and kinetic energy terms. The equilibration of kinetic and potential energies was attained after about 1000 time steps, and was followed by a simulation run of $7000\Delta t$, corresponding to 35 ps. This time is sufficiently long for noting diffusion in yttria-stabilised cubic zirconia.

The particular value of MD methods is that they allow direct calculation of diffusion coefficients. The anion diffusion coefficient D_i was obtained from the equation $< \Delta r_i^2(t) > = 6D_i|t| + B_i$, where $B_i \rightarrow 0$ where $|t| \rightarrow \infty$ for an infinitesimally small time step. Thus, D_i is obtained directly from the slope of the mean-square displacement versus time graph. However, the mean-square displacement tells us about the rate of diffusion and little else. Self-correlation functions, on the other hand, provide a means of capturing the diffusion process by giving the full probability distributions of the displacements. The radial distribution function (RDF), $g_{ij}(r)$, is the simplest positional correlation function that gives the probability of finding an ion of type *j* from an ion of type *i* situated at the origin (see section 2.4.2.1(b) for further details).

It was established in Chapter 3 that in general the *l*-group of configurations were most stable as compared to the *x*- and *y*-groups. It was for this reason that only clusters based on the *l*-type (L_4- and a combination of L_1-, L_2- and L_4-configurations for $x = 9.4$ and $x = 15$, 21 and 24, respectively) were taken

as structural entities on which transport and structural properties in cubic zirconia were calculated. It was also established (Chapter 3) that results obtained with the short range parameter C = 0.0 were broadly consistent. Consequently, MD calculations were performed with C = 0.0. Nonetheless, some calculations were also performed with C = 27.89 for completeness sake.

4.2 RESULTS

Results from molecular dynamics studies are presented in this section. The variation of the mean-square displacements (MSD) with both temperature and yttria content are investigated. Next, results from ion trajectories are presented, which reveal the type(s) of migration processes involved in yttria-stabilised cubic zirconia. The nature of the defect structure is shown using radial distribution functions. The results are discussed in section 4.3.

The runs were made at temperatures ranging from 300 K to 1600 K, at 100 K intervals, but only results obtained from T = 1600 K, 1500 K, 1300 K, 1000 K, 700 K and 300 K are used in the results and discussions. Furthermore, since the transition temperatures in the concentrations x = 9.4 and 24 are 1300 K and 1050 K (Ngoepe *et al.* 1990), respectively, the range of temperatures considered in the present investigation spanned the regions above and below the respective transition temperatures.

Plots of the mean-square displacements versus time (35 ps) for the anions in ZrO_2(x mol% Y_2O_3), with x = 9.4, 15, 21 and 24, for T = 1600 K, 1500 K, 1300 K, 1000 K, 700 K and 300 K are shown in figure 4.2.1(a)-(b), respectively, for calculations performed with both C = 0.0 and C = 27.89. It appears from the plots that inclusion (exclusion) of the van der Waals and dispersive interactions has

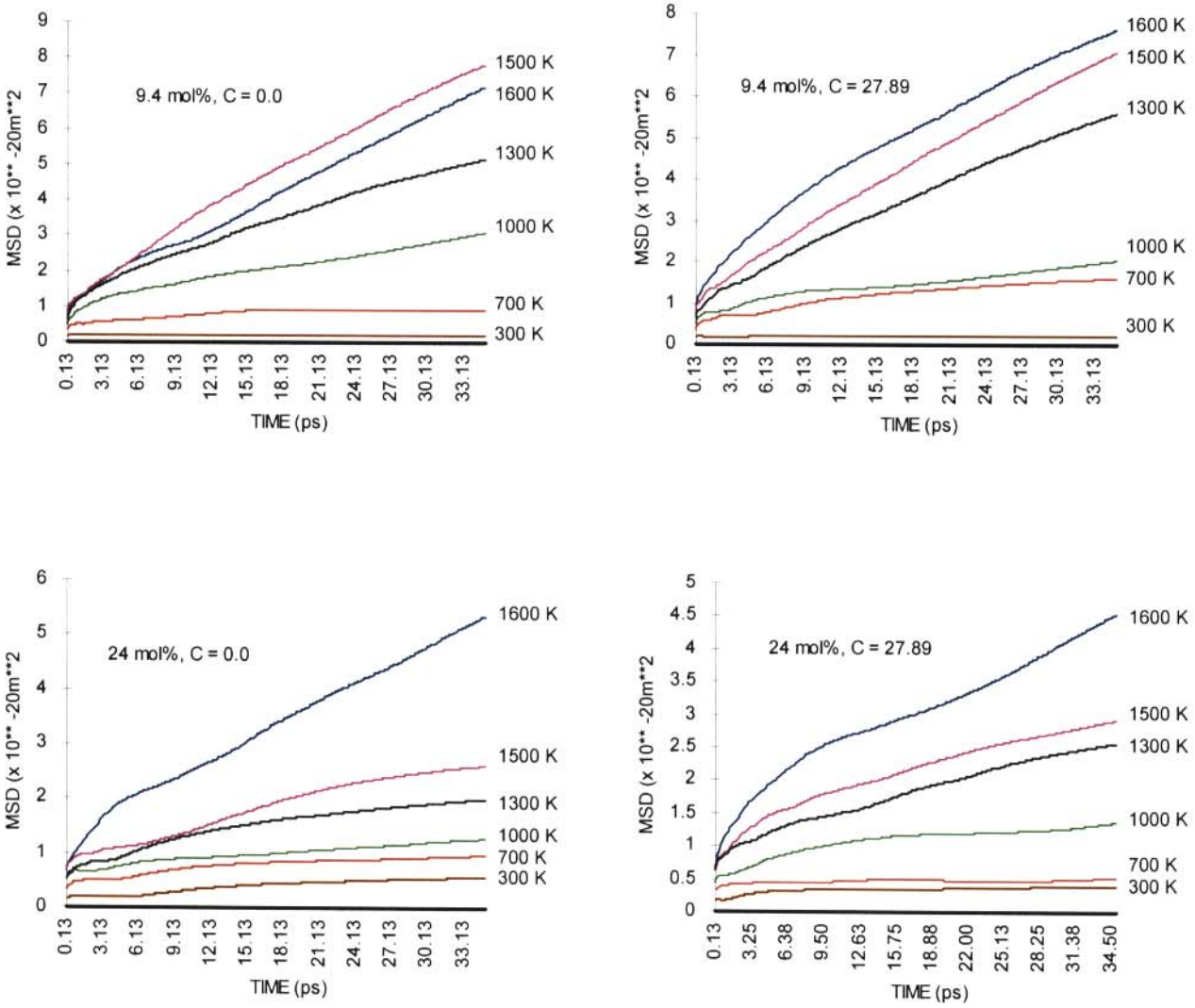

Figure 4.2.1(a) The variation of mean-square displacements with time for oxygen ions from x = 9.4 and x = 24, and at various temperatures with both C = 0.0 and 27.89

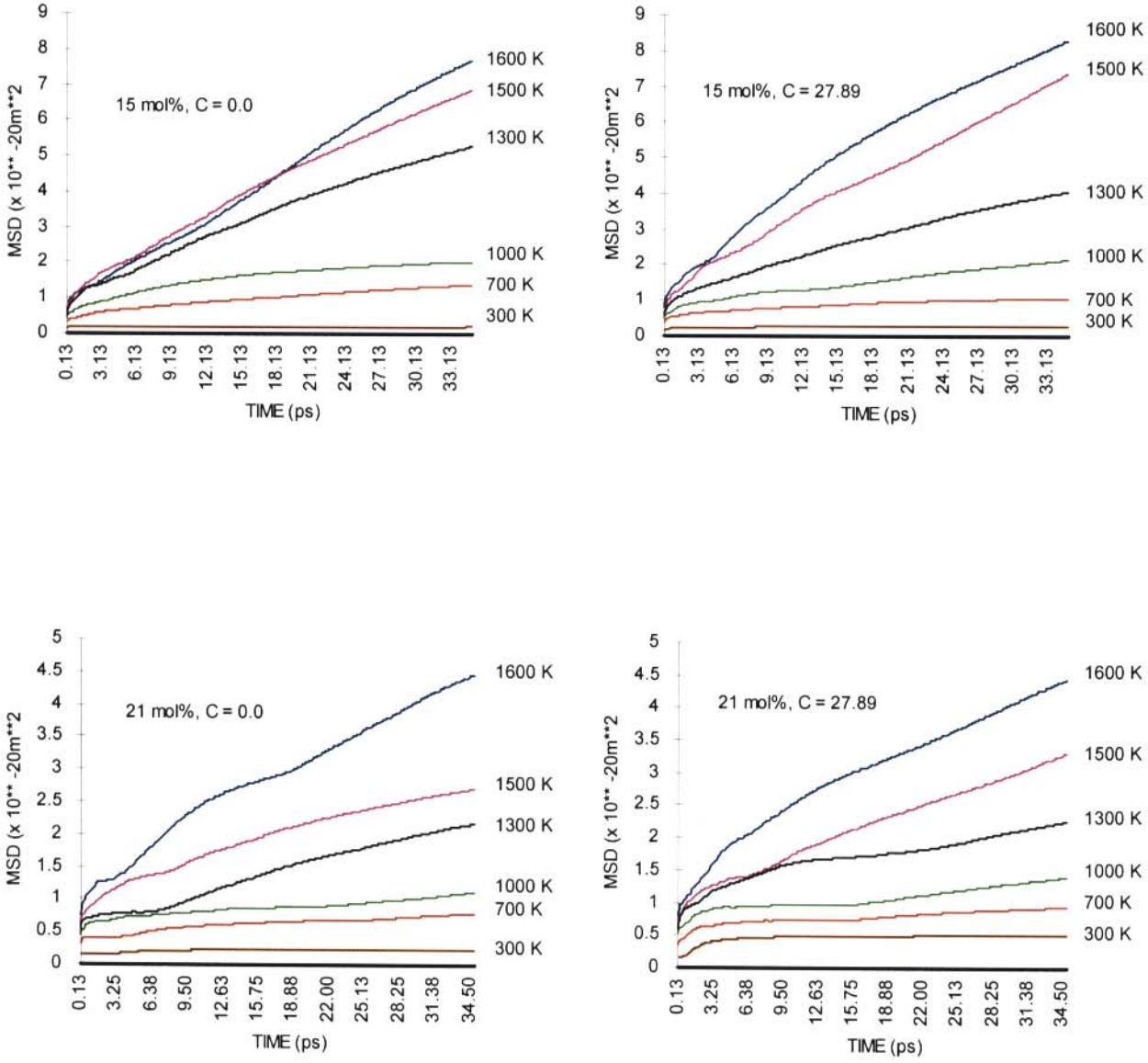

Figure 4.2.1(b) The variation of mean-square displacements with time for oxygen ions from x = 15 and x = 21, and at various temperatures with both C = 0.0 and 27.89

an influence on the mean-square displacements in the lower concentrations, particularly the x = 9.4 and x = 15 samples. Figure 4.2.1(c) illustrates the variation of MSD with time for Zr^{4+} and Y^{3+} ions. This is only shown for the x = 9.4 concentration since the behaviour is the same for all concentrations.

Figure 4.2.2(a)-(b) shows the variations of mean-square displacements with temperature for the various concentrations. Anion diffusion coefficients at various concentrations and temperatures are reported in table 4.2.2(a) for both (i) C = 0.0 and (ii) C = 27.89, while experimental values are reflected in table 4.2.2(b). The variation of anion diffusion coefficients with yttria content are shown in figure 4.2.3 for T = 1500, 1300, 1000, and 700 K. It is apparent from this plot that the maximum in conductivity will occur somewhere between 9.4 and 15 mol%.

Plots of ion trajectories for ion 507 are shown in figure 4.2.4 for x = 9.4 at T = 1600 K, T = 1500 K, 1300 K and 1000 K, for the periods of 35 ps. These are shown for both C = 0.0 and C = 27.89. The idea was to demonstrate the effects of temperature on ion mobility; on those ions that have been identified as highly mobile at T = 1600 K. In a similar manner, these effects were shown for ions 470, 329 and 439 for x = 15, 21 and 24, respectively, in figure 4.2.5, figure 4.2.6 and figure 4.2.7, respectively. Ion motion appears to be occuring predominantly along the [100] direction.

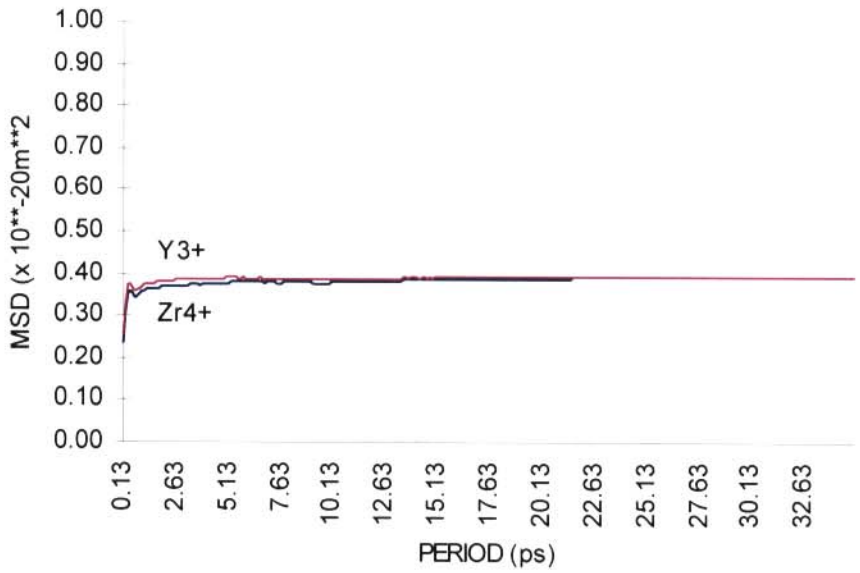

Figure 4.2.1(c) The variation of mean-square displacements with time for cations from x = 9.4 with C = 0.0

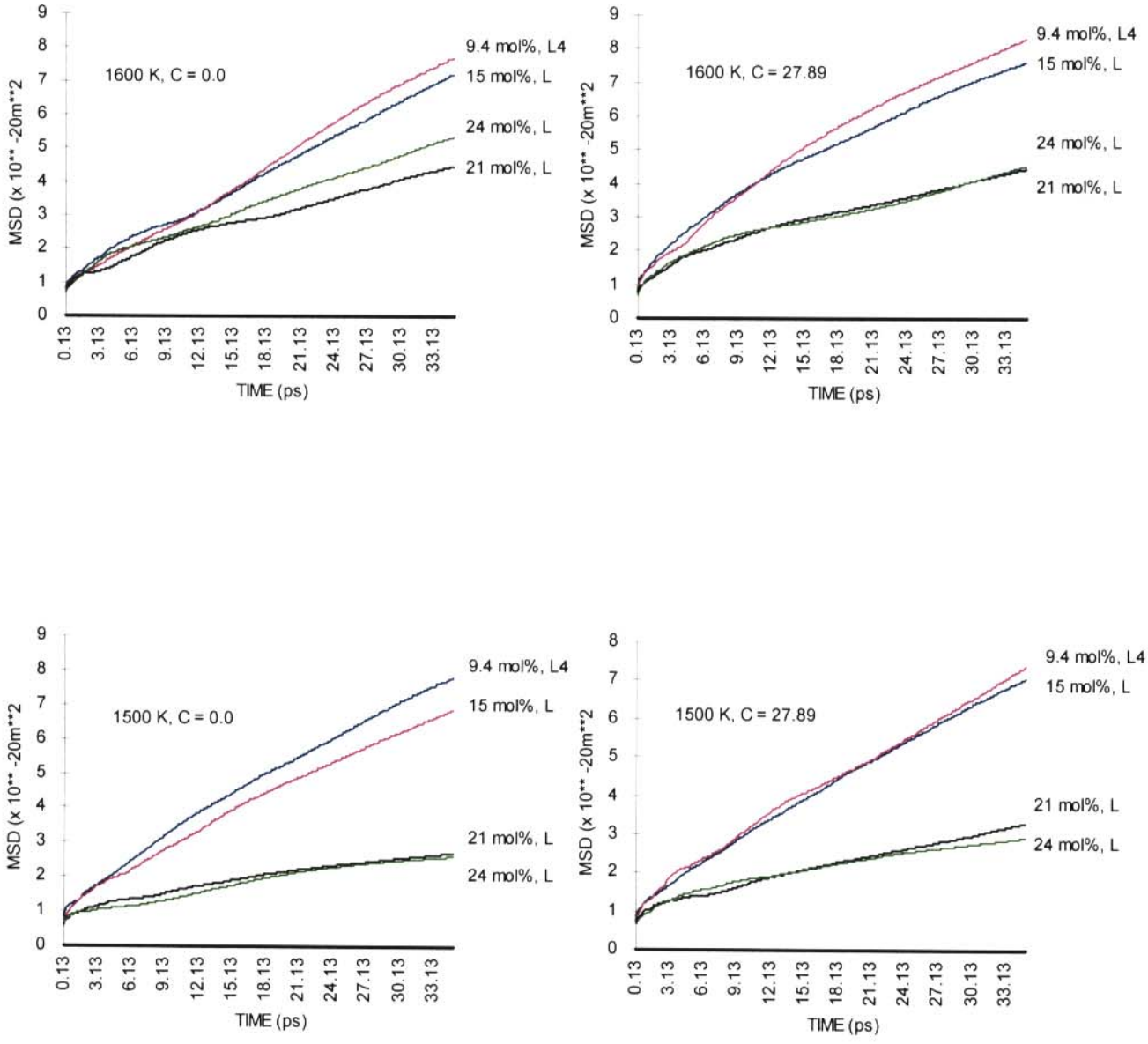

Figure 4.2.2(a) The variation of mean-square displacements with temperature (T = 1600 and 1500 K) at various yttria contents with both C = 0.0 and 27.89

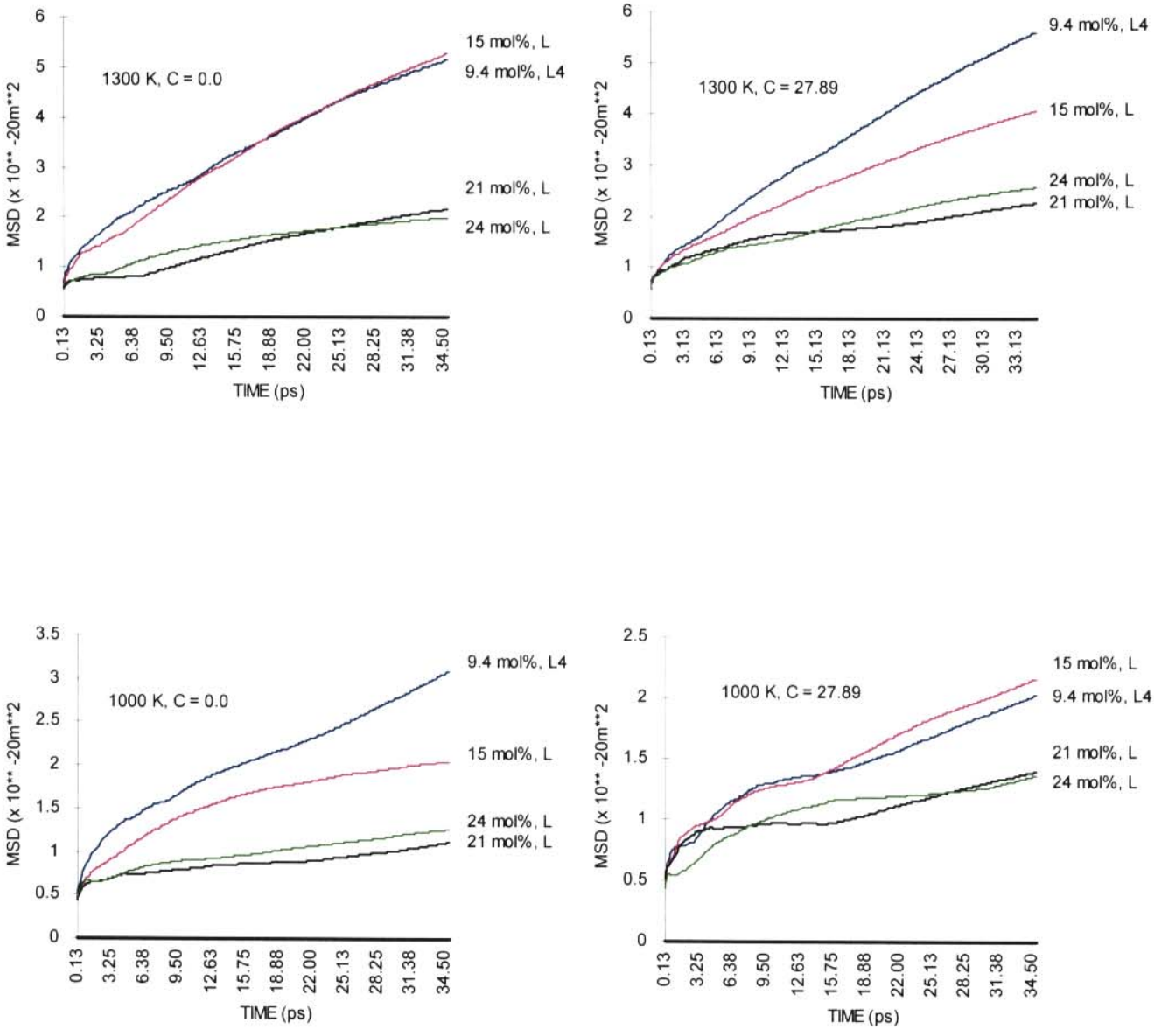

Figure 4.2.2(b) The variation of mean-square displacements with temperature (T = 1300 and 1000 K) at various yttria contents with both C = 0.0 and 27.89

Table 4.2.2(a) Anion diffusion coefficients at various yttria contents and temperatures.

	C = 0.0				C = 27.89			
	D_i (x 10^{-5} cm^2 / s)				D_i (x 10^{-5} cm^2 / s)			
Temperature	Yttria content (mol%)				Yttria content (mol%)			
(K)	9.4	15	21	24	9.4	15	21	24
1600	0.297	0.332	0.136	0.196	0.250	0.290	0.120	0.130
1500	0.290	0.255	0.071	0.060	0.270	0.270	0.100	0.070
1300	0.158	0.185	0.075	0.020	0.190	0.130	0.040	0.080
1000	0.094	0.038	0.022	0.027	0.040	0.060	0.020	0.010
700	0.007	0.033	0.009	0.011	0.030	0.020	0.010	0.000
300	0.000	0.000	0.000	0.000	0.000	0.000	0.000	0.000

Table 4.2.2(b) Experimental values for diffusion coefficients in yttria-stabilised cubic zirconia.

Yttria content (mol%)	Temperature (K)	D_i(x $10^{-5}$$cm^2$/s)
12	1000	1.4#
10.2	2073	0.19*
10	1040	0.42@

Perry and Feinberg (1980), @ Suemoto (1990), * Shimojo *et al.* (1992). Note that there were no experimental values of diffusion coefficients for the concentrations considered in the present investigation.

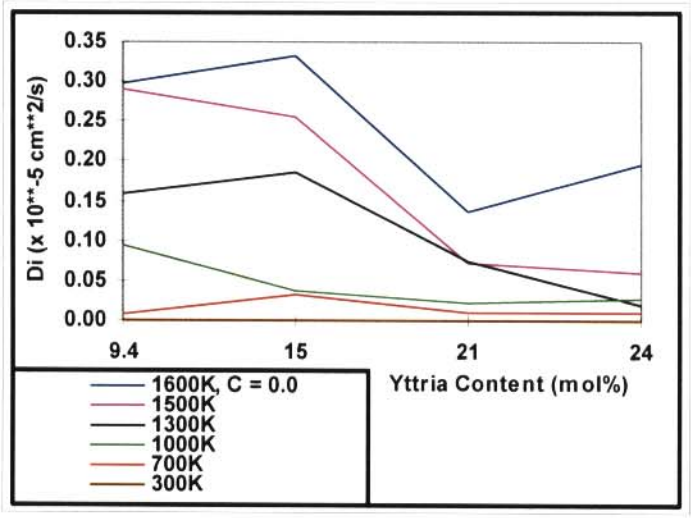

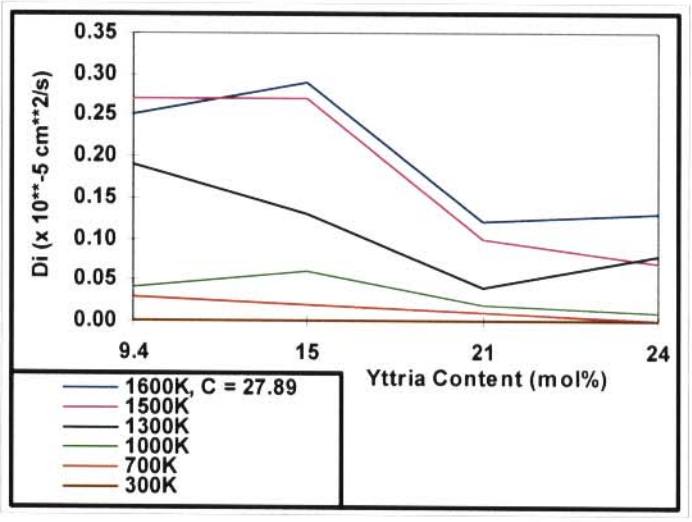

Figure 4.2.3 The variation of anion diffusion coefficients with yttria content at T = 1600, 1500, 1300, 1000, 700 and 300 K

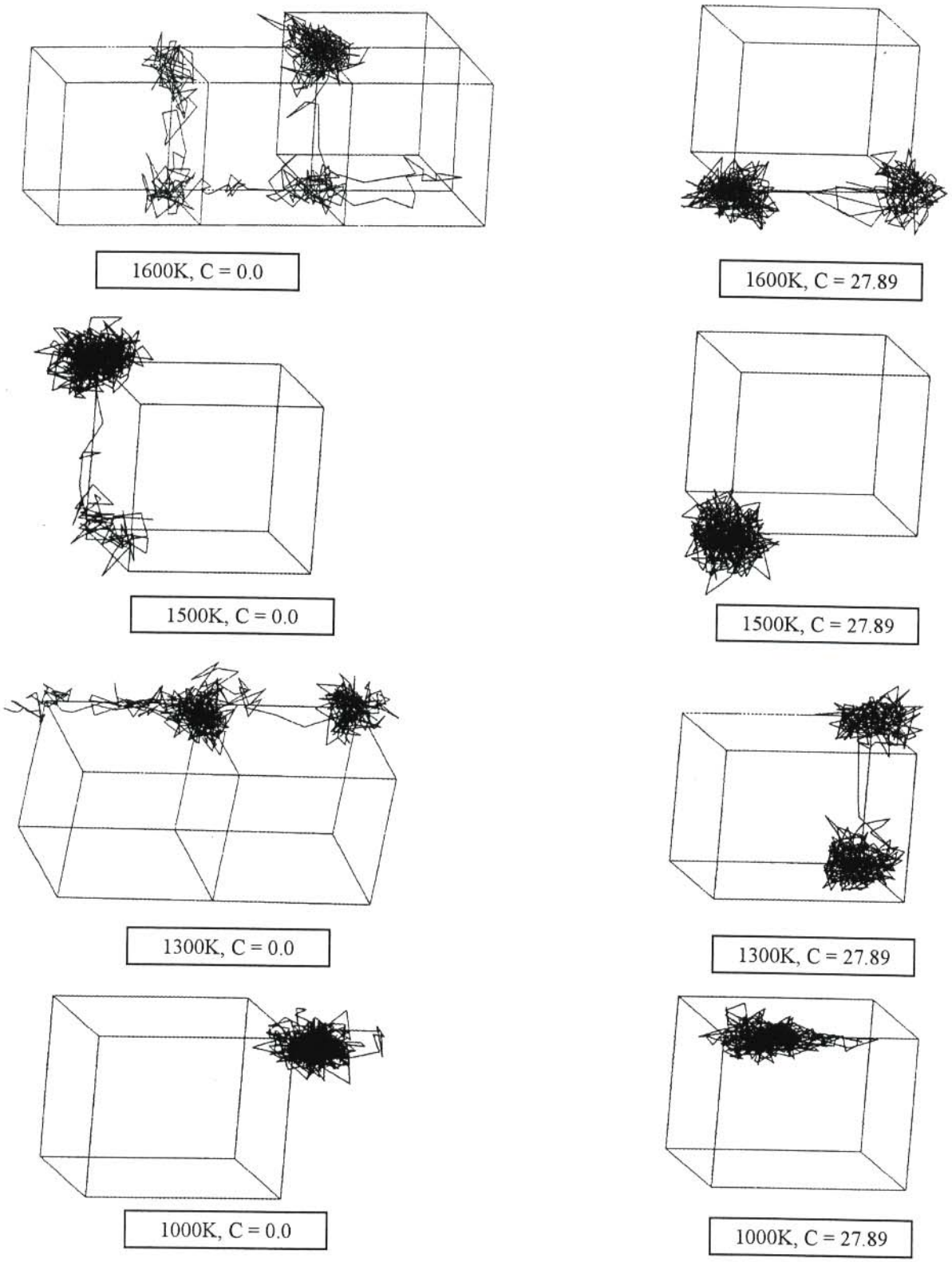

Figure 4.2.4 Plots of ion trajectories for ion 507 from x = 9.4 at various temperatures and with both C = 0.0 and C = 27.89

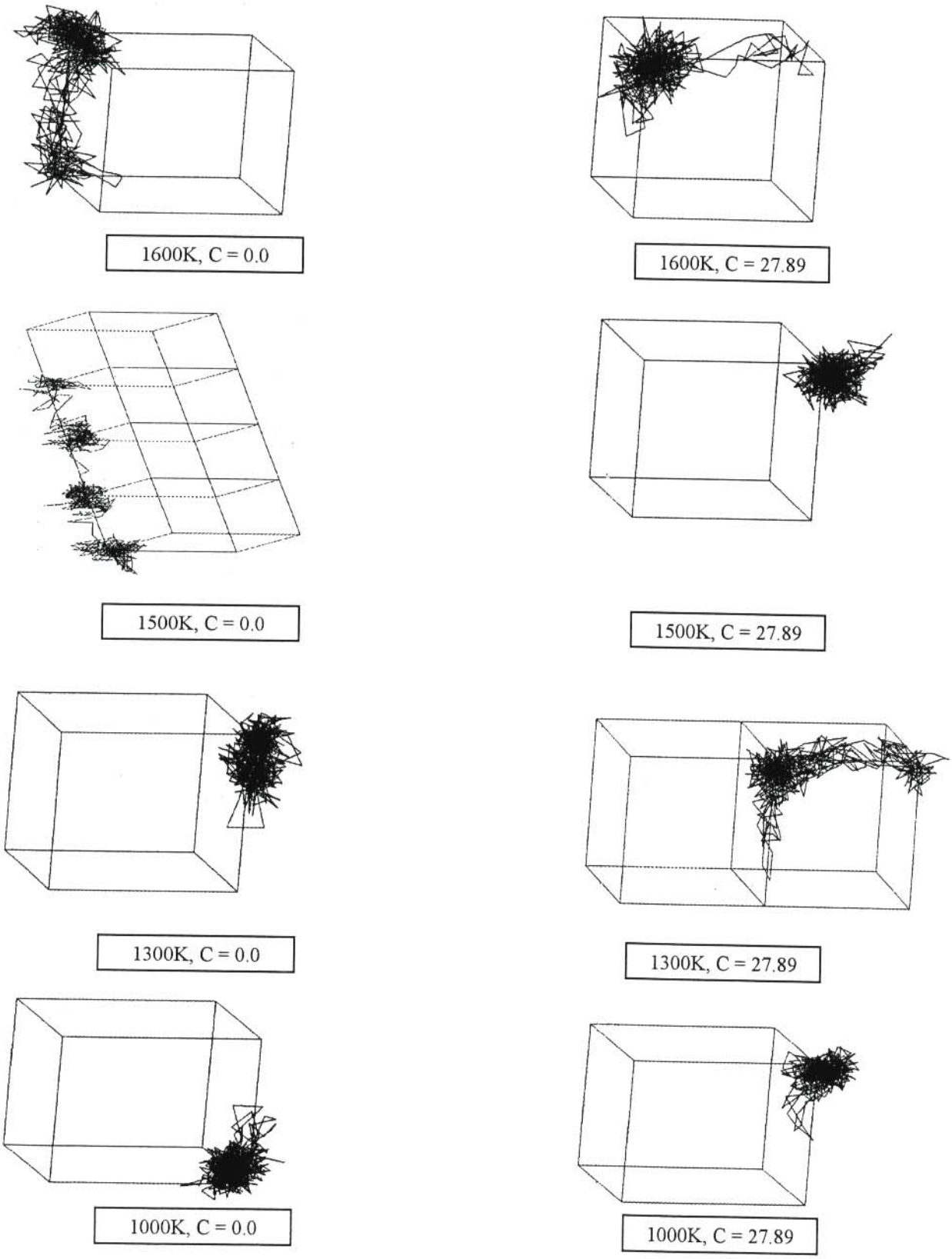

Figure 4.2.5 Plots of ion trajectories for ion 470 from x = 15 at various temperatures and with both C = 0.0 and C = 27.89

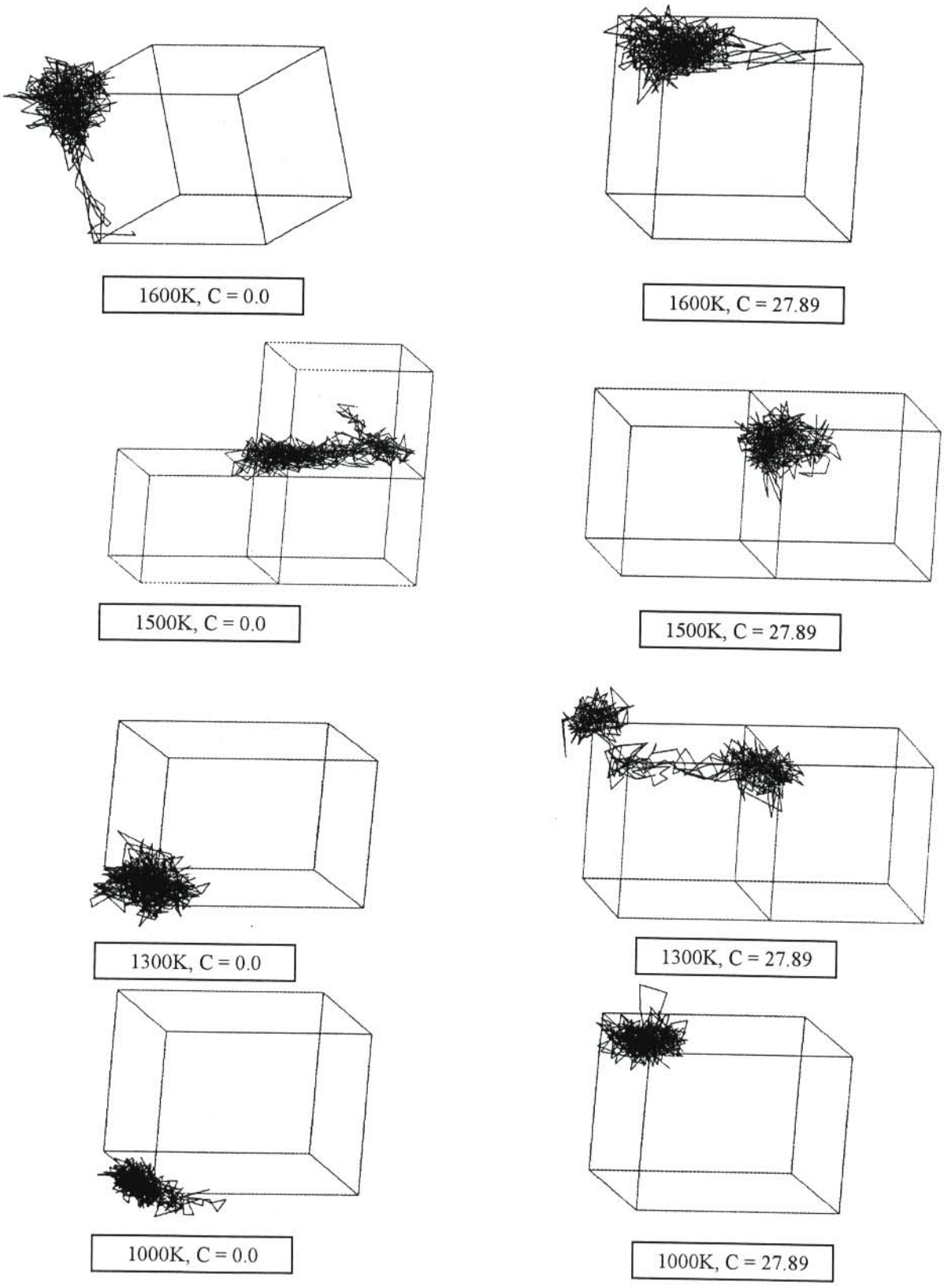

Figure 4.2.6 Plots of ion trajectories for ion 329 from x = 21 at various temperatures and with both C = 0.0 and C = 27.89

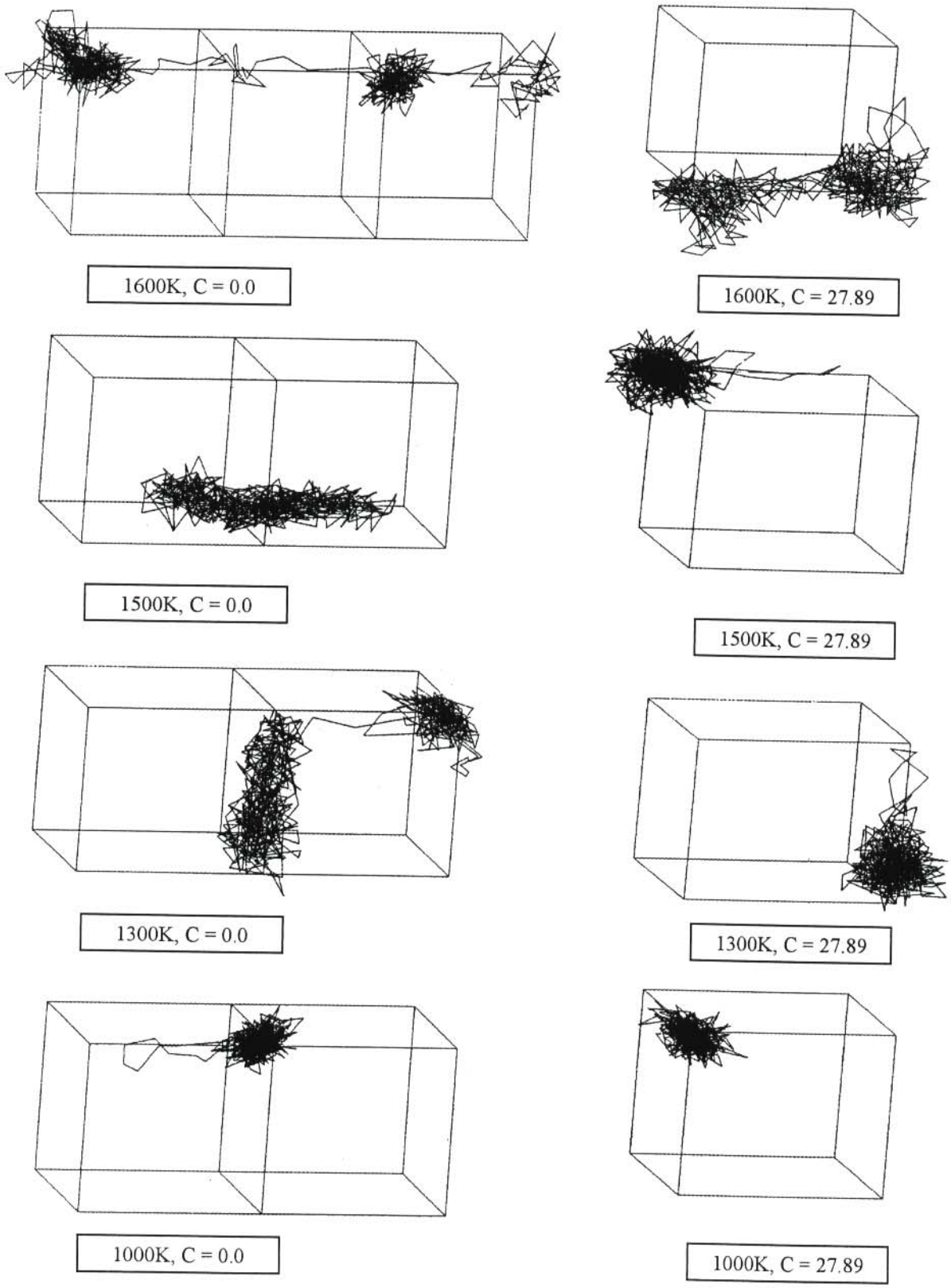

Figure 4.2.7 Plots of ion trajectories for ion 493 from x = 24 at various temperatures and with both C = 0.0 and C = 27.89

Partial pair distribution functions, $g_{ij}(r)$, for all pairs of ions at 1600K and 1000K, for x = 9.4, 15, 21 and 24, are shown in figure 4.2.8(a)-(b) with C = 0.0 only. These temperatures span the various transition temperature regions, the highest being T_c = 1300K, for x = 9.4 and the lowest being T_c = 1050K, for x = 24 (Ngoepe 1987). Furthermore, only radial distribution functions obtained when C = 0.0 were used since those obtained when C = 27.89 were similar. The corresponding heights of the first peaks are listed for T = 1600 K, 1500 K, 1300 K, 1000 K, 700 K and 300 K in table 4.2.3(a)-(c) while NN distances are presented in table 4.2.4(a)-(c).

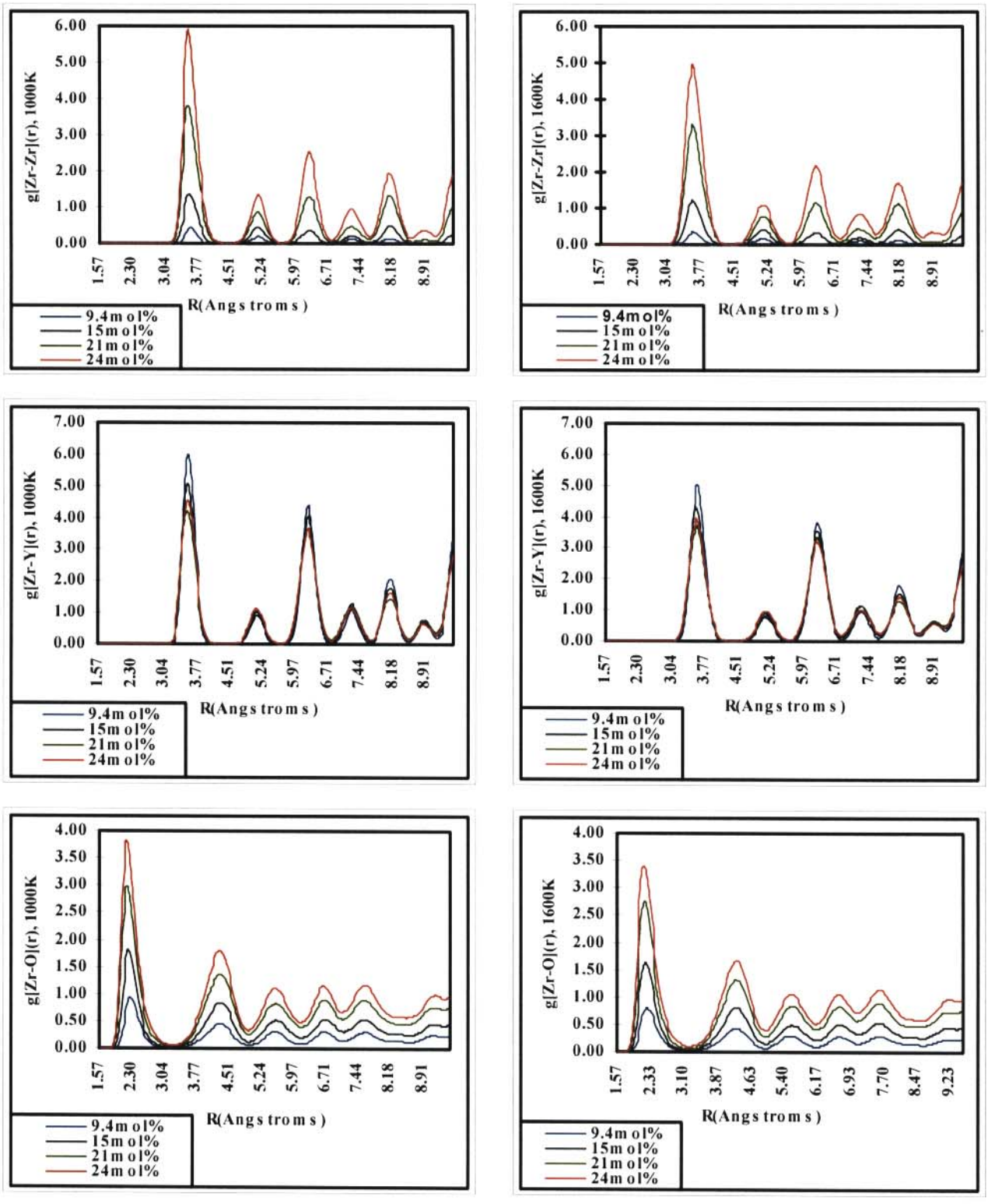

Figure 4.2.8(a) Partial pair distribution functions for $g_{Zr\text{-}Zr}$, $g_{Zr\text{-}Y}$ and $g_{Zr\text{-}O}$ at various concentrations, at both T = 1600 and 1000 K and with C = 0.0

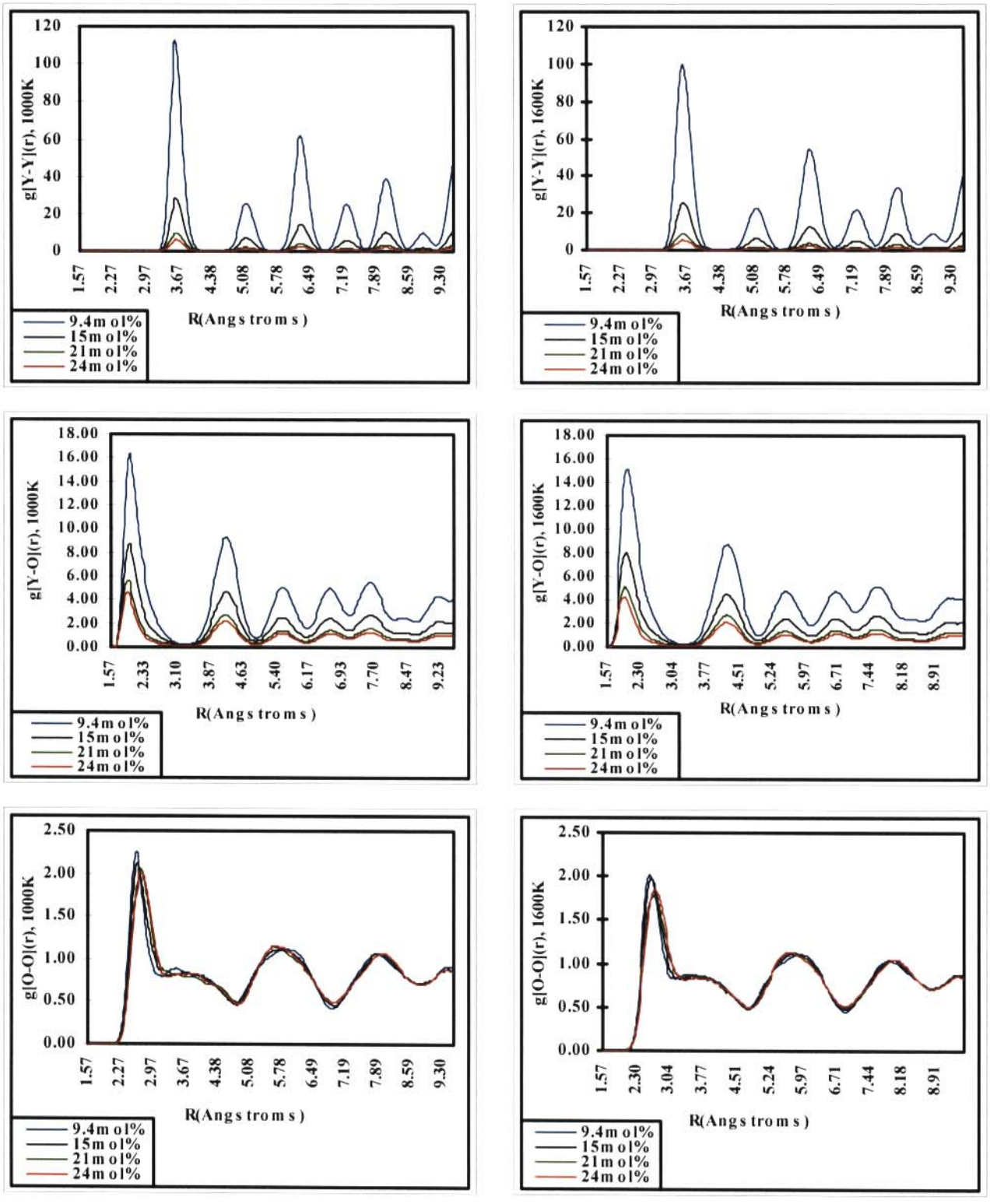

Figure 4.2.8(b) Partial pair distribution functions for $g_{Y\text{-}Y}$, $g_{Y\text{-}O}$ and $g_{O\text{-}O}$ at various concentrations, at both T = 1600 and 1000 K and with C = 0.0

Table 4.2.3(a)-(c) The heights of the first peaks for the various concentrations and temperatures with C = 0.0.

Temp. (K)	Heights of the first peaks (10^{-10}m)							
	Zr - Zr				Zr - Y			
	Yttria content (mol%)				Yttria content (mol%)			
	9.4	15	21	24	9.4	15	21	24
1600	0.35	1.22	3.44	5.01	5.04	4.35	3.65	4.02
1500	0.38	1.27	3.45	5.16	5.12	4.49	3.87	4.03
1300	0.38	1.33	3.64	5.35	5.67	4.77	4.04	4.21
1000	0.43	1.37	3.82	5.90	6.00	5.06	4.24	4.54
700	0.48	1.64	4.41	6.10	7.06	5.35	4.55	4.85
300	0.67	1.87	5.46	6.75	8.57	5.99	5.27	5.57

(a)

Temp. (K)	Heights of the first peaks (10^{-10}m)							
	Zr - O				Y - Y			
	Yttria content (mol%)				Yttria content (mol%)			
	9.4	15	21	24	9.4	15	21	24
1600	0.79	1.62	2.76	3.46	99.60	25.45	8.88	4.02
1500	0.80	1.62	2.78	3.50	103.7	25.63	9.03	4.03
1300	0.86	1.69	2.86	3.60	107.1	25.88	9.23	4.21
1000	0.93	1.81	2.99	3.83	113.2	28.29	9.82	4.54
700	1.02	1.84	3.22	4.07	123.9	30.90	10.43	4.85
300	1.20	2.02	3.52	4.71	136.7	32.74	10.89	5.57

(b)

Heights of the first peaks (10^{-10}m)								
	Y - O				O - O			
Temp.	Yttria content (mol%)				Yttria content (mol%)			
(K)	9.4	15	21	24	9.4	15	21	24
1600	15.15	8.03	5.07	4.20	2.03	1.98	1.92	1.94
1500	15.40	8.04	5.11	4.35	2.05	1.97	1.93	1.99
1300	15.89	8.46	5.35	4.41	2.14	2.01	2.01	1.93
1000	16.47	8.73	5.63	4.67	2.25	2.15	2.06	2.02
700	17.61	9.51	5.89	4.95	2.38	2.19	2.16	2.13
300	20.79	10.6	7.05	5.22	2.71	2.45	2.12	2.22

(c)

Table 4.2.4(a)-(c) Nearest neighbour distances for various concentrations and temperatures with C = 0.0.

Nearest neighbour distances (10^{-10}m)								
	Zr - Zr				Zr - Y			
Temp.	Yttria content (mol%)				Yttria content (mol%)			
(K)	9.4	15	21	24	9.4	15	21	24
1600	3.61	3.57	3.57	3.57	3.60	3.59	3.58	3.63
1000	3.64	3.61	3.56	3.58	3.59	3.58	3.58	3.58

(a)

Temp. (K)	Nearest neighbour distances (10^{-10}m)							
	Y - O				Y - Y			
	Yttria content (mol%)				Yttria content (mol%)			
	9.4	15	21	24	9.4	15	21	24
1600	2.25	2.24	2.22	2.17	3.61	3.61	3.61	3.61
1000	2.27	2.24	2.22	2.21	3.61	3.61	3.62	3.64

(b)

Temp. (K)	Nearest neighbour distances (10^{-10}m)							
	Zr - O				O - O			
	Yttria content (mol%)				Yttria content (mol%)			
	9.4	15	21	24	9.4	15	21	24
1600	2.02	1.99	1.98	1.95	2.60	2.63	2.70	2.72
1000	2.02	1.98	1.96	1.95	2.62	2.65	2.74	2.72

(c)

4.3 DISCUSSIONS

In this section results obtained from molecular dynamics studies are discussed. Ion transport and structural properties in yttria-stabilised cubic zirconia are explained in terms of results obtained from static lattice simulation methods (Chapter 3) as well as observations by other workers, be experimental or computational. Where previous complementary results are lacking, possible suggestions and explanations of observed phenomena are advanced.

The range of concentrations used in the present investigation (9.4, 15, 21 and 24 mol% Y_2O_3) is at extremes of the minimum and maximum amount of yttria content required to fully stabilise pure zirconia in the cubic phase (Ngoepe 1987, Botha *et al.* 1993). We have also covered the temperature range from 300 K to 1600 K. Shimojo and Okazaki (1992) investigated oxygen migrations in systems containing 4.85, 10.2 and 22.7 mol% Y_2O_3. The x = 4.85 and x = 22.7 concentrations are clearly below the extremes of the yttria contents normally encountered in cubic zirconia. In particular, the x = 4.85 yttria content is lower than the minimum value (8 mol%) required to fully stabilize zirconia in the cubic phase (Duwez *et al.* 1951). The maximum yttria content is usually 24 mol%. Hence, the calculations in the present investigation should produce better results.

In the current work, the mean-square displacement versus time plots show that diffusion is almost negligible at room temperature but increases with temperature on the oxygen sub-lattice in ZrO_2(x mol% Y_2O_3), with x = 9.4, 15, 21 and 24. Furthermore, cation mobility is significantly small at all temperatures. This is in agreement with previous molecular dynamics studies in oxygen (Li and Hafskjold 1995, Khan *et al.* 1998) and fluorine ion conductors (Netshisaulu 1996). The presence of the fast - ion phase has been well established in yttria stabilised cubic

zirconia (Li and Hafskjold 1995); and transition temperatures to this phase, at different yttria contents, were determined by Brillouin scattering studies (Ngoepe and Comins 1987). They were found to be about 1300 K, 1200 K, 1100 K and 1050 K for the x = 9.4, 15, 21 and 24 concentrations, respectively.

A notable feature, in the current study, is the enhanced oxygen diffusion below the respective transition temperatures in all the doping concentrations. This is in contrast to diffusion trends in pure fluorine ion conductors with the flourite structure (Ngoepe and Catlow 1991) and (Netshisaulu *et al.* 1992) as well as in pure oxygen ion conductors (Islam *et al.* 1996). However, substantial oxygen diffusion was reported by MD studies (Ngoepe and Catlow 1991) on CaF_2(10 mol% LaF_3) and Brillouin and Raman scattering (Anghel and Comins 1997) in LaF_3(5 mol% BaF_2). Hence, some of the mechanisms responsible for enhanced anion diffusion below T_c in doped oxygen and fluorine ion conductors could account for the observed high oxygen mobility at lower temperatures in ZrO_2(x mol% Y_2O_3).

Generally, significant increases in oxygen diffusion is noted above T_c in almost all the yttria concentrations considered in the present investigation. This is in agreement with high temperature ionic conductivity measurements (Tien and Subbarao 1963, Suzuki *et al.* 1981), wherein anomalous increases in ionic conductivity were mentioned above T_c. This was also observed in doped oxygen ion conductors (Islam *et al.* 1996).

In the current work, oxygen diffusion was found to decrease with increasing yttria content. Generally, the diffusion arises essentially from the migration of oxygen ions through the anion vacancies (Tien and Subbarao 1963), and as such the relationship between conductivity and vacancies might be expected to lead to an increase in

conductivity with increasing yttria content. Results of our work are in agreement with MD studies on fluorine ion conductors (Ngoepe and Catlow 1991) where fluorine ion diffusion was found to be very rapid in pure CaF_2 and reduced on doping. This retarded motion was ascribed to defect repulsive interactions. A similar behaviour was also observed (Li and Hafskjold 1995) in ZrO_2(x mol% Y_2O_3) from MD studies. This was attributed to an increasing number of Y^{3+} - Y^{3+} neighbour pairs, which tend to trap oxygen vacancies. It would seem that large defect aggregates, which form as the doping level increases (Dwivedi and Cormack 1990), trap the oxygen vacancies, resulting in a decrease in diffusion coefficient. Thus, at low concentrations, small dynamic clusters prevail and the highest mobility occurs through the tetrahedrally distorted regions (Andersen *et al.* 1986a). The presence of considerable dopant concentrations affects oxygen diffusion as observed from figure 4.2.1(a). Futhermore, as the yttria content was increased, the number of charge compensating defects also increased, giving rise to a highly defective system. Under these conditions, the charges tend to cancel themselves locally, thus increasing the probability of the formation of Y^{3+} ion-anion vacancy complexes and even larger defect complexes. The formation of such clusters has been evidenced by the negative association energies observed in section 3.4.1. However, with increasing doping level the lattice becomes gradually filled with static defects and the paths of least activation energy through which the oxygen ions percolate become blocked and the ions are trapped at strongly bound sites (Catlow 1991). This explains why the diffusion coefficients generally decrease with increasing yttria content (figure 4.2.2(a)-(b)).

We now compare the magnitudes of oxygen diffusion at high temperatures with those from experiment. There are marked differences among oxygen diffusion coeffients from previous experimental studies (see table 4.2.2(b)). Our value is of

the same order of magnitude as that from quasielastic light scattering (Suemoto 1990) and Shimojo and Okazaki (1992) although the latter measurements were carried out at a much higher temperature. The experimental value obtained by Perry and Feinberg (1980) is very high compared to the other measurements. Our value is a reasonable estimation to be given by molecular dynamics calculation based on rigid ion potential.

It has been shown (section 1.4.2.2) that a maximum in conductivity occurs around 10.2 mol% Y_2O_3 by Shimojo *et al.* (1992). Although there is an increase in the diffusion coefficient between $x = 9.4$ and $x = 24$ samples, it is difficult, given the largely spaced concentrations, to say exactly where the maximum occurs in figure 4.2.5. However, it is possible that the curve could reach a maximum anywhere between $x = 9.4$ and $x = 15$. More calculations need to be done, especially around the $x = 10$ region, before a firm conclusion can be reached. However, it can be said with certainty that the rate of diffusion decreases substantially beyond the $x = 15$ concentration.

One of the important features of molecular dynamics studies has been the determination of atomistic mechanisms controlling bulk transport properties. The pictures of ion trajectories derived from molecular dynamics simulations illustrate anion migration processes very clearly. The oxygen ions spend most of their time at lattice sites and only hop to the nearest-neighbour positions (satisfying $t_{dwe} \geq t_{sp}$: section 1.1) via vacancy mechanisms along the $<100>$ directions. It may be concluded that whereas oxygen diffusion is negligible at room temperature, it proceeds predominantly by a hopping vacancy mechanism at higher temperatures. This type of motion is consistent with the lower calculated oxygen vacancy as compared to interstitial activation energy, for both $x = 9.4$ and $x = 24$

concentrations (Chapter 3). The prevalence of the anion vacancy motion was reported in pure alkaline-earth fluorides (Ngoepe and Catlow 1991). On the contrary, interstitialcy motion appears to be dominant in rare-earth doped alkaline - earth fluorides (Ngoepe and Catlow 1991) and mixed metal fluorides (Netshisaulu 1996) and on $RbBiF_4$ (Cox and Catlow 1994) . Differences in migration mechanisms between our current ZrO_2(x mol% Y_2O_3) and doped rare-earth flourides may suggest that the nature of disorder responsible for the fast-ion phase in these systems is different.

An important feature also observed from the trajectories is that the dwell-time differs at various lattice sites. This phenomenon was investigated in relation to the locality of the anion vacancies to the migrating O^{2-} ions. In general there is very little backward-forward migrations in the vicinity of the oxygen vacancies (away from the dopant cations) indicating that indeed the vacancies facilitate rapid migration and hence were responsible for the observed high ionic conductivities. Furthermore, the dwell-time around a vacancy was very short while that away from the vacancy was generally very long. It is possible that the mobile ions experienced strong coulombic repulsions from other oxygen ions at large distances from the vacancy. In this region the ions came into close encounter with the larger Y^{3+} ions which effectively slowed them down, prolonging the dwell-time. There were instances where the vacancies were remote to the anions but limited dwell-time was observed. In this case the vacancy at NNN position shifted towards the mobile ion during the equilibration period to be in the NN position to the particular lattice position.

We now discuss results from the radial distribution functions (RDFs) in ZrO_2(x mol% Y_2O_3) for x = 9.4, 15, 21 and 24. RDFs provide more definite information on the local structure in this system. The cation-cation RDFs have well shaped, sharp

peaks corresponding to successive NN distances. This is normal for an order solid and is in agreement with results from the recent MD studies (Islam *et al.* 1996, Shimojo *et al.* 1992). In contrast, the anion-anion RDFs show a weak, diffuse structure for separations larger than NN. Thus, the anions form a weakly correlated subsystem and point to the loss of long range order on the oxygen sub-lattice. Similar results were obtained by Islam *et al.* (1996).

In the current work, the first peaks decrease in size while the general profile broadens away from the first peak when the temperature increases. This behaviour was also observed in previous MD studies (Islam *et al.* 1996) in yttria-stabilised cubic zirconia and was ascribed to increasing level of disorder emanating from increased temperature. Thus, as the temperature was increased, thermally generated defects and hence disorder, increased as expected. The longest peaks were obtained from the Y-Y, Y-O and Zr-Y interactions, indicating a large disorder accompanying the introduction of the Y^{3+} ions. This was also observed by Shimojo *et al.* (1992).

Increasing the yttria concentration also had an opposite effect on the first peak: it increased in size. However, the profile further away from the first peak also widened. This is in agreement with other MD results (Shimojo *et al.* 1992). The height of the subpeak in $g_{O\text{-}O}(r)$ gradually decreased and disappeared at $x = 24$. This is attributed to local deformation on the anion sublattice and was also observed by Shimojo *et al.* (1992) in yttria-stabilised cubic zirconia using MD techniques.

Our results also show that the magnitudes of the cation-anion distances are in the same order of magnitude as MD results on the same system (Shimojo *et al.* 1992). Furthermore, in general the Y - O nearest neighbour distances are larger than the

corresponding Zr - O distances. This is in agreement with MD (Shimojo *et al.* 1992) and experimental (Catlow *et al.* 1986, Roth *et al.* 1986, Veal *et al.* 1988) results.

In conclusion, the *I*-shaped cluster identified in the previous chapter was used as the structural entity on which supercells used in MD calculations were formed. The calculations were performed at various dopant concentrations and at different temperatures. The calculated mean-square displacements, diffusion coefficients and radial distribution functions are generally in agreement with previous MD results.

CHAPTER 5

CONCLUSIONS AND RECOMMENDATIONS

The objectives of the research were to understand elastic properties, defect and transport mechanisms in yttria-stabilised cubic zirconia. These properties have been extensively investigated using computer simulation techniques. The major conclusions and recommendations for future work are advanced in this chapter.

The unique features of the current investigation are the following:

1. Different dopant clusters were systematically investigated to identify the configuration that will yield the best thermodynamic properties
2 We have presented for the first time a full set of elastic properties, and their temperature dependences, in yttria-stabilised cubic zirconia using computer simulation techniques
3 The MD calculations were carried on supercells designed from the cluster that reproduced thermodynamic properties. In contrast, the dopant charge compensating vacancy complexes were randomly chosen in previous MD studies.
4. We have covered the full range of concentrations (9.4, 15, 21 and 24 mol% Y_2O_3), which includes the extremes of the minimum and maximum amount of yttria content required to fully stabilise pure zirconia in the cubic phase; as well as the temperature range (300K to 1600K) which covers the transition temperatures to the fastion phase.

5.1 CONCLUSIONS

The calculated anion vacancy activation energies were found to be smaller than the

anion interstitial activation energies for both $x = 9.4$ and $x = 24$, indicating the preference for vacancy motion in yttria-stabilised cubic zirconia. The activation energy values agreed with those from experiment (Solier *et al.* 1988) in the $x = 9.4$ concentration, and are in the range of results by Dwivedi and Cormack (1990) on calcia-stabilised cubic zirconia. However, the calculated anion activation energies were greater than those in fluorine ion conducting solids (CaF_2, SrF_2, BaF_2, and $SrCl_2$) reported by Catlow *et al.* (1977) and UO_2 (Walker and Catlow 1981). This seems to suggest that it is easier to generate defects in fluorine ion conducting materials than it is in oxygen conducting systems such as yttria-stabilised cubic zirconia.

Different clusters involving the oxygen vacancies and dopant cations were systematically investigated to identify the configuration that will yield the best thermodynamic properties. The *I*-group of clusters reproduced the experimental elastic constants and their temperature gradients results very well and was subsequently used as the structural entity on which supercells for MD calculations were based.

In general, a linear decrease in all elastic constants up to a characteristic transition temperature T_c followed by anomalous behaviour in certain elastic constants was observed. This is in agreement with results from Brillouin scattering from Botha *et al.* 1993, Ngoepe and Comins (1987) and Ngoepe (1987). The quasi-linear decrease in all elastic constants below T_c is ascribed to lattice anharmonicity associated with thermal expansion (Garber and Granato 1975).

The oxygen vacancies are preferentially located at NNN sited to the dopant cations. This is consistent with previous EXAFS studies (Veal *et al.* 1988, Catlow *et al.*

1986) as well as computer simulation studies on calcia-stabilised cubic zirconia (Dwivedi and Cormack 1990).

Substantial oxygen diffusion was observed below the respective transition temperatures in all the dopant concentrations. This is in contrast to diffusion trends reported in studies on pure fluorine ion conductors with the flourite structure (Ngoepe and Catlow 1991, Netshisaulu *et al.* 1992) as well as in pure oxygen ion conductors (Islam *et al.* 1996), but agrees with MD results on CaF_2(10 mol% LaF_3) reported by Ngoepe and Catlow (1991) and Brillouin and Raman scattering (Anghel and Comins 1997) in LaF_3(5 mol% BaF_2). It is suggested that some of the mechanisms responsible for enhanced anion diffusion below T_c in doped oxygen and fluorine ion conductors could account for the observed high oxygen mobility at lower temperatures in ZrO_2(x mol% Y_2O_3).

Oxygen diffusion was found to decrease with increasing yttria content, in agreement with MD studies on fluorine ion conductors (Ngoepe and Catlow 1991) as well as in yttria-stabilised cubic zirconia (Li and Hafskjold 1995, Shimojo *et al.* 1992). The observed retarded motion is ascribed to an increasing number of Y^{3+} - Y^{3+} neighbour pairs, particularly in large defect aggregates, which tend to trap oxygen vacancies. This is in agreement with results from defect energy calculations on calcia stabilised cubic zirconia (Dwivedi and Cormack 1990).

MD was also used to determine atomistic mechanisms controlling bulk transport properties. The pictures of ion trajectories show that the oxygen ions spend most of their time at lattice sites and only hop to the nearest-neighbour positions via vacancy mechanisms along the <100> directions. This type of motion is consistent with the lower calculated oxygen vacancy activation energy (Chapter 3) as well as the

results from pure alkaline-earth fluorides (Ngoepe and Catlow 1991) but differed with results from rare-earth doped alkaline - earth fluorides (Ngoepe and Catlow 1991), mixed metal fluorides (Netshisaulu 1996) and Cox and Catlow (1994) on $RbBiF_4$ where intersticialcy motion was preferred. Differences in migration mechanisms between our current ZrO_2(x mol% Y_2O_3) and doped rare-earth flourides may suggest that the nature of disorder responsible for the fast-ion phase in these systems is different.

The cation-cation radial distribution functions (RDFs) have well shaped, sharp peaks corresponding to successive NN distances. This is normal for an ordered solid and is in agreement with results from the recent MD studies (Islam *et al.* 1996, Shimojo *et al.* 1992). In contrast, the anion-anion RDFs show a weak, diffuse structure for separations larger than NN. Thus, the anions form a weakly correlated subsystem and point to the loss of long range order on the oxygen sub-lattice. Similar results were obtained by Islam *et al.* (1996) on doped oxygen ion conductors.

5.2 RECOMMENDATIONS

In this section recommendations for further study in those aspects which will help clarify the underlying mechanisms, suggestions and observations identified in this work are presented.

The dependence of defect energies on the size of region I, the centering mechanism as well as the effect of the host lattice after the removal or introduction of an ionic species in the system on defect energies require a systematic investigation. Pursuit of these thoughts may lead to a better understanding of the apparent relationship between the ageing phenomenon, and decrease in ionic conductivity with increasing doping level, and formation of larger defect clusters. The information obtained will

be valuable in MD studies which will provide further clarifications on some of the observations made in this work.

The relationship between the various configurations and elastic constants must be explored much further, particularly since certain configurations were found to be unstable while others did not show the expected behaviour in accordance with experimental observations. In this regard, it might be worthwhile to even consider larger unit cells for better statistics.

MD calculations were performed using the *I*-shaped cluster only. Different configurations should be investigated to check whether previous MD results will be reproduced.

REFERENCES

Adby P R and Dempster M A H 1974 Introduction to Optimisation Methods (Chapman and Hall: London)

Alder B J and Wainwright T W 1959 J. Chem. Phys. **31** 459

Alder B J and Wainwright T W 1958 Transport Processes in Statistical Mechanics ed Prigogine I (Interscience: New York)

Aleksandrov V I, Kitaeva V F, Kozlov I V, Osiko V V, Sobolev N N, Tatarintsev V M and Chistyi L I 1975 Sov. Phys. Solid State **16** 1456

Allen M P and Tildeskey D J 1987 in "Computer Simulation of Liquids" (Clarendon: Oxford)

Allpress J G 1975 J. Solid State Chem. **15** 68

Allpress J G and Rossell H J 1975 J. Solid State Chem. **15** 68

Allpress J G, Rossell H J and Scott H G 1975 J. Solid State Chem. **14** 264

Anastassakis E, Papanicolaou B and Asher I M 1975 J. Phys. Chem. Solids **36** 667 - 676

Andersen H C 1980 J. Chem. Phys. **72** 2384

Andersen N H, Clausen K, Hackett M A, Hayes W, Hutchings M T, Macdonald J E and Osborn R 1985 Proceedings of the 6th Riso International Symposium on Metallurgy and Materials Science eds F W Paulsen, N H Andersen, K Clausen, S Skaarup and O T Sorensen

Andersen N H, Clausen K, Kjems J K and Schoonman J 1986a J. Phys. C**19** 2377

Andersen N H, Clausen K, Hackett M A, Hayes W, Hutchings M T, Macdonald J E and Osborn R 1986b Physica B**136** 315

Antonsen O, Baukal W, Fischer W 1966 Brown Boven Mitteiling **53** 21 - 30

Asher I, Papanicolaou B and Anastassakis E 1976 J. Phys. Chem. Solids **37**

Archer D H and Sverdrup E F 1962 Ann. Power Sources Conf. **16** 34

Archer D H, Sverdrup E F and Zahrardrik R L 1964 Chem. Eng. Progr. Symp. Ser. **60** 64 - 68

Bansal G K and Heuer A H 1972 Acta Met. **20** 1281

Bauer E and Preis H 1937 Z. Electrochem. **43** 727

Bayer G 1970 J. Am. Ceram. Soc. **53** 294

Beeman D 1976 J. Comp. Phys. **20** 130

Berendsen H J 1986 Molecular Dynamics Simulation of Statistical Mechanical Systems eds G Cicotti and W G Hoover (North-Holland: Amsterdam)

Binder H, Kohling A, Krupp H, Ritcher K and Sandstede G 1963 Electrochim. Acta **8** 781

Blumenthal R N and Seitz M A 1974 Electrical Conductivity in Ceramics and Glass ed N M Tauan (Dekker: New York) Part A 15

Born M and Huang K 1954 Dynamical Theory Of Crystal Lattices (Oxford Univ. Press: London)

Botha J C, Chiang J C-H, Comins J D, Mjwara P M and Ngoepe P E 1993 J. Appl. Phys. **73** 7268

Boyce J B and Huberman B A 1979 Phys. Rep. **51** 189

Brugger K 1964 Phys. Rev. A**133** 1611

Buchanan R C 1986 Ceramic Materials for Electronics ed R C Buchanan (Marcel Dekker: New York) 57

Butler V, Catlow C R A and Fender B E F 1981 Solid State Ionics **5** 539

Butler V, Catlow C R A, Fender B E F and Harding J H 1983 Solid State Ionics **8** 109

Bystrom A and and Bystrom A M 1950 Acta Cryst. 3 146

Carter R E and Roth W L 1968 Electromotive Force Measurements in High

Temperature Systems ed C R Alcock (Institute of Mining and Metallurgy: New York) 125

Carter R E, Rocco W A, Spacil H S and Tragert W E 1963 Chem. Eng. News. **47** 14

Catlow C R A 1977 Proc. R. Soc. Lond. A**353** 533

Catlow C R A 1980a Proc. Roy. Soc. A**353** 533

Catlow C R A 1980b J. Phys. (Paris) C**6** 41

Catlow C R A 1981 in "Non-Stoichiometric Oxides" ed O T Sorensen (Academic: Press: London)

Catlow C R A 1983 Solid State Ionics **8** 89 - 107

Catlow C R A 1986a Ann. Rev. Mater. Sci. **16** 516

Catlow C R A 1986b in "Defects in Solids" eds A V Chadwick and M Terenzi (Plenum Press: New York) 269

Catlow C R A 1987 in "Defects in Solids, Modern Techniques" eds Chadwick A V and Terenzi M ASI Series B: Physics **147** (Plenum Press: London)

Catlow C R A and Jackson R A 1988 Molecular Simulations **1** 207

Catlow C R A 1990 in "Computer Modelling of Fluids, Polymers and Solids" **293** eds Catlow C R A, Parker S C and Allen M P (Kluwer Academic Publishers: London)

Catlow C R A 1997 in "Computer Modelling in Inorganic Crystallography" (Academic Press: London)

Catlow C R A, Chadwick A V, Greaves G N and Moroney L M 1986c J. Am. Ceram. Soc. **69**

Catlow C R A 1990 Computer Modeling of Fluids, Polymers and Solids **293** eds C R A Catlow, S C Parker and M P Allen (Kluwer Academic: London)

Catlow C R A, Chadwick A V and Corish J 1983 J. Solid State Chem. **48** 165

Catlow C R A, Chadwick A V, Cormack A N, Greaves G N, Leslie N and

Moroney L M 1986 Defect Properties and Processing of High Technology nonmetallic materials, Materials Research Society Symposium Proceeding **60** eds Y Chen, W D Kingesy and R J Stokes (Material Research Society: Pittsburgh, Pennsylvania) 173

Catlow C R A, Chadwick A V, Greaves G N and Moroney L M 1985 Cryst. Lattice Defects **12** 193

Catlow C R A, Comins J D, Germano F A, Haley R T and Hayes W 1978 J. Phys. C**11** 3197

Catlow C R A, Comins J D, Germano F A, Haley R T, Hayes W and Owen I B 1981 J. Phys. C**1** 93

Catlow C R A, Comins J D, Germano F A, Haley R T and Hayes W 1982 Phys. Lett. A**71** 97

Catlow C R A and Fender B E F 1975 J. Phys. C**8** 3267

Catlow C R A and Hayes W 1982 J. Phys. C**15** L9

Catlow C R A and James R 1982 Proc. Roy. Soc. Lond. A**384** 157

Catlow C R A and Mackrodt W C 1982 Computer Simulation of Solids, Lecture Notes in Physics **166** (Springer-Verlag: Berlin)

Catlow C R A and Norgett M J 1973 J. Phys. C**6** 1325

Catlow C R A, Norgett M J and Ross T A 1977 J. Phys. C: Solid State Phys. **10** 1627

Catlow C R A and Parker S C 1982 in "Computer Simulation of Solids, Lecture Notes in Physics" **166** (Springer-Verlag: Berlin)

Chandra S 1981 Superionic Solids (North-Holland: Amsterdam)

Chase L L 1976 Superionic Conductors eds G D Mahan and W L Roth (Plenum Press: New York) 299

Cheetham A K, Fender B E F and Cooper M J 1971 J. Phys. C: Solid State Phys. **4** 3107

Chisty I L, Fabelinskii I L, Kitaeva V F, Osiko V V, Pisarevskii Yu V, Sil'vestrova I M and Sobolev N N 1977 J. Raman Spectros. **6** 183

Clausen K, Hayes W, Hutchings M T, Kjems J K, Schnabel P and Macdonald J E 1983 High Temp. - High Press. **15** 383

Clausen K, Hayes W, Hutchings M T, Kjems J K, Macdonald J E and Osborn R 1985 High Temp. Sci. **19** 189

Clausen K, Hayes W, Macdonald J E, Osborn R and Schnabel P 1984a Rev. Phys. Appl. **19** 719

Clausen K, Hayes W, Macdonald J E and Osborn R 1984b Phys. Rev. Lett. **52** 1238

Cohen J B, Morinaga M and Faber Jr J 1981 Solid State Ionics **3 & 4** 61

Cole M, Catlow C R A and Dragun J P 1990 J. Phys. Chem. Solids **51** 507

Comins J D, Ngoepe P E and Catlow C R A 1990 J. Chem. Soc. Faraday Trans. **86** 1183

Cox P A, Catlow C R A and Chadwick A V 1994 J. Mater. Sci. **29** 2725

Cowley E R and Cowley R A 1965 Proc. Roy. Soc. Lond. A**287** 259

De Bruin H J and Murch G E 1973 Phil. Mag. **27** 1475

De Dios Solier J, Perez-Jubindo M A, Dominguez-Rodriguez A and Heuer A H 1989 J. Am. Ceram. Soc. **72** 1500

Dell R M and Hooper A 1978 Solid Electrolytes eds P Hagenmuller and W van Gool (Academic Press: New York)

Derrington C E and O'Keefe M 1973 Nature (London) Phys. Sci. **246** 44

Dick B G and Overhauser A W 1958 Phys. Rev. B**112** 90

Dickens M H, Hayes W, Hutchings M T and Smith C 1982 J. Phys. C**15** 4043

Dietrich W and Peschel I 1983 J. Phys. C**16** 3841

Dietzel A and Tober H 1953 Ber. Deut. Keram. Ges. **30** 47

Duwez P, Brown F H Jr. and Odell F 1951 J. Electrochem. Soc. **9** 356

Dwivedi A and Cormack A N 1989 J. Solid State Chem. **79** 218

Dwivedi A and Cormack A N 1990 Phil. Mag. A**61** 1

Dworkin A S and Bredig M A 1968 J. Phys. Chem. **72** 1277

Egelstaff P A 1965 Thermal Neutron Scattering (Academic Press: New York)

Elliot R J, Hayes W, Klappmann W G, Rushworth A J and Ryan J F 1978 Proc. Soc. London A**360** 317

Etsell T H and Flengas S N 1970 Chem. Rev. B**11** 3990

Faber J Jr, Mueller M H and Looper B R 1978 Phys. Rev. B**17** 4884

Farley J M, Thorp J S, Ross J S and Saunders G A 1972 J. Mat. Sci. **7** 475

Faux I D and Lidiard A B 1971 Z. Naturforsh A**26** 62

Feinberg A and Perry C H 1981 J. Phys. Chem. Solids **42** 513

Figueroa D R, Chadwick A V and Strange J H 1978 J. Phys. C**11** 55

Figueroa D R, Fontana J J, Wintersgill M C and Andersen G C 1984 Phys. Rev. B**29** 5909

Fincham D 1990 Computer Modelling of Fluids and Polymers eds C R A Catlow, S C Parker and M P Allen (Kluwer Academic: Dordrecht) chp 11

Funke K 1976 Prog. Solid State Chem. **11** 345

Garber J A and Granato A V 1975 Phys. Rev. B**11** 3990

Gerhardt-Andersen R and Norwick A S 1981 Solid State Ionics **5** 547

Gillian M J 1985 Physica B**131** 157

Gillian M J 1986 J. Phys. C**19** 3517

Gillan M J and Dixon M J 1980 J. Physique Coll. C**41** 24

Ginzburg V L, Levanyuk A P and Solyanin A A 1980 Phys. Lett. **11** 310

Gordon R G and Kim Y S 1972 J. Chem. Phys. **56** 3122

Goto K and Pluschkell W 1973 Physics of Electrolytes ed J Hladick (Academic Press: New York) **2** 539

Hackett M A, Anderson N H, Clausen K, Hayes W, Hutchings M T, Macdonald J

E and Osborne R 1985 Defects in Solids eds A V Chadwick and M Terenzi (Plenum Press: London)

Hailing T and Saunders G A 1982 J. Mat. Sci. Lett. **1** 416

Hamilton J C and Nagelberg A 1984 J. Am. Ceram. Soc. **67** 686

Hammou A, Deporters C, Robert G and Vitter G 1971 Mater. Res. Bull. **6** 823

Hansen J P and Macdonald I R 1986 Theory of Simple Liquids (Academic Press: London)

Harding J H 1985 Physica B**13** 13

Harley R T, Hayes W, Rushworth A J and Ryan J F 1975 J. Phys. C**8** L530

Hart S, Wallis J and Sigalas I 1986 Physica B**139 & 140** 183

Hayes W 1978 Contemp. Phys. **19** 469

Hayes W and London R 1978 Scattering of Light by Crystals (John Wiley & Sons: New York)

Hayes W and Stoneham A M 1985 Defects and Defect Processes in Non-Metalic Solids (John Wiley & Sons: New York)

Hibma T and Beyeler Ho 1976 Superionic Conductors eds G D Mahan and W L Roth (Plenum Press: New York) 221

Hiki Y, Thomas J F and Granato A V 1967 Phys. Rev. **153** 764

Ho S M 1982 Mat. Sci. Eng. **54** 23

Hodby J W 1974 Crystals with the Fluorite Structure ed W Hayes (Clarendon Press: Oxford) 1

Hoshen J and Kopelman R 1976 Phys. Rev. B**14** 3428

Huberman B A 1974 Phys. Rev. Lett. **32** 1000

Hudson B and Moseley P T 1976 J. Solid State Chem. **19** 383

Hull S, Farley T W D, Hackett M A, Hayes W, Osborn R, Andersen N A, Clausen K, Hutchings M T and Stirling W G 1988 Solid State Ionics **28** 30

Hutchings M T, Clausen K, Dickens M H, Hayes W, Kjems J K, Schnabel P G and Smith C 1983 Harwell Report AERE - R11127

Hutchings M T, Clausen K, Hayes W, Macdonald J E, Osborn R and Schnabel P 1985 High Temp. Sci. **20** 97

Iijima S 1974 Proc. Conf. Diffr. of Real Atoms and Real Crystals, Melbourne

Ishigame M and Sakurai T 1977 J. Am. Ceram. Soc. **60** 367

Islam M S, Cherry M and Catlow C R A 1996 J. Solid State Chemistry **124** 230

Jackson R A, Murray A D, Harding J H and Catlow C R A 1986 Phil. Mag. A**53** 27

Jacobs P W M and Moscinski J 1985 Physica **131**B 175

Jacobs P W M and Rycerz Z A 1987 Molecular Dynamics Methods in "Computer Modelling in Inorganic Crystallography" (Academic Press: New York)

Jacobs P W M, Rycerz Z A and Moscinski J 1990 Adv. Solid State Chem. **2** 113

Jordan M M and Catlow C R A 1987 Cryst. Latt. Def. **15** 81

Jost W and Kubaschewski P 1968 Z. Phys. Chem. **60** 69

Jost W 1971 J. Chem. Phys. **55** 4680

Kandil H M, Greiner J D and Smith J F 1984 J. Am. Ceram. Soc **67** 341

Kawamura K and Okada I 1978 Atomic Eng. Rev. **16** 209

Kermidas V and White W 1974 J. Am. Ceram. Soc. **57** 22

Ketron L 1989 Ceram. Bull. **68** 860

Khan M S, Islam M S and Bates D R 1998 J. Phys. Chem. B**102** 3099

Kilner J, Benson S, Lane J and Walker D 1997 Chem. Ind. **22** 907

Klein M V 1976 Proc. 3rd Int. Conf. on Light Scatt. in Solids (Flammerion Sci.: Paris)

Ladd A J C 1990 Computer Modelling of Fluids, Polymers and Solids eds C R A

Catlow, S C Parker and M P Allen (Kluwer Academic: London)

Lanagan M T, Yamamoto J K, Bhalla A and Sankor S G 1989 Mater. Lett. **7** 437

Leslie M 1982 SERC Daresbury Laboratory Technical Memorandum No. DL/SCI/TM31 - T

Leslie M 1983 Solid State Ionics **8** 243

Lewis G V and Catlow C R A 1985 J. Phys. C**18** 1149

Li X and Hafskjold B 1995 J. Phys.: Condensed Matter **7** 1255

Lindan P J D, Muscat J, Bates S, Harrison N M and Gillan M 1997 Farady Discuss. **106** 135

Lindan P J D and Gillan M J 1991 J. Phys. **3** 3929

Lindan P J D and Gillan M J 1994 Phil. Mag. **B69** 535

Mackrodt W C, Birnie D and Kingery D, to be published

Mackrodt W C and Woodrow P M 1986 J. Am. Ceram. Soc. **69** 277

Mainwood A, Larkins F P and Stoneham A M 1978 Solid State Electron. **21** 1431

Manasreh M D and Pederson D O 1984 Phys. Rev. B**30** 3482

Manasreh M D and Pederson D O 1985 Phys. Rev. B**31** 3960

Markin T L, Bones R J and Dell R M 1976 In "Int. Conf. Superionic Conductors", Schenectady (North-Holland: Amsterdam)

Masri P, Harker A H and Stoneham A M 1983 J. Phys. C: Solid State Phys. **16** L613

Matsui T and Wagnet J B 1977a J. Electrochem. Soc. **124** 300

Matsui T and Wagnet J B 1977b J. Electrochem. Soc. **124** 610

McCullough J D and Trueblood K N 1959 Acta Crystallogr. **12** 507

Minh N Q 1993 J. Am. Ceram. Soc. **76** 563

Mitskevich V V 1963 Sov. Phys. Solid State **5** 1127

Mombourquette M J and Weil J A 1985 Can. J. Phys. **63** 1282

Morinaga M and Cohen J B 1979 Acta Crystallogr. A**35** 789

Morinaga M and Cohen J B 1980 Acta Crystallogr. A**36** 520

Morinaga M, Cohen J B and Faber Jr J 1980 Acta Crystallogr. A**36** 520

Morinaga M, Cohen J B and Faber Jr J 1979 Acta Crystallogr. A**35** 789

Moscinski J and Jacobs P W M 1985 Physica B**131** 175

Mott N F and Gurney R 1957 Electronic Processes in Ionic Crystals (Clarendon: Oxford)

Mott N F and Littleton M J 1938 Trans. Faraday Soc. **34** 485

Moulson A J and Herbert J M 1990 Electroceramics: Materials Properties and Applications (Chapman and Hall: London)

Murch G E 1975 Phil. Mag. **32** 1129

Murch G E 1982a Phil. Mag. A**46** 151

Murch G E 1982b Phil. Mag. A**46** 575

Murch G E 1984a Phil. Mag. A**46** 575

Murch G E 1984b Diffusion in Crystalline Solids eds G E Murch and A S Norwick (Academic Press: New York)

Murch G E 1984c Traditional Methods in Diffusion eds G E Murch, H K Birnbaum and J R Cost (AIME: Warrendale)

Murch G E, Catlow C R A and Murray A D 1986 Solid State Ionics **18 & 19** 196

Nemanich R J, Martin R M and Mikkelsen Jr J C 1979 Sol. State Commun. **32** 79

Netshisaulu T T, Ngoepe P E, Comins J D and Catlow C R A 1992 Proceedings of the XII International Conference on Defects in Insulating Materials, eds Karnet O and Spaeth J M World Scientific Publishers

Netshisaulu T T 1996 M. Sc. Dissertation, University of the North

Ngoepe 1987 PhD Thesis University of the Witwatersrand

Ngoepe P E and Comins J D 1987 J. Phys. C: Solid State Phys. **20** 2983

Ngoepe P E and Catlow C R A 1991 Crys. Lattice Defects and Amophours Materials

Ngoepe P E and Comins J D 1987 Cryst. Lattice Defects **15** 317

Ngoepe P E, Jordan W M, Catlow C R A and Comins J D 1990 Phys. Rev. B**41** 3815

Ngoepe P E and Parker S C 1992 Mol. Simulation **8** 345

Nikol'skii Y V, Filatov S K, Zhuraii T A and Frank - Kannenetskii V A 1972 Inorg. Mat. **8** 1322

Norgett M J 1974 UKAEA Report AERE-M 2936

Norgett M J and Lidiard A B 1972 in "Computational Solid State Physics" eds F Herman, N W Dalton and T R Coehler (Plenum Press: New York)

Nosi S 1984 Mol. Phys. **52** 255

Notting J and Rein D D 1969 J. Phys. Chem. **66** 150

Oishi Y and Ando K 1984 Transport in Non-Stoichiometric Compounds eds G Simkovich and V S Stubican (Plenum Press: New York) **129** 189

Osborn R, Andersen N H, Clausen K, Hackett M H, Hayes W, Hutchings M T and Macdonald J E 1986 Mat. Sci. Forum **7** 55

Pace N G, Sauders G A, Sumengen Z and Thorp J S 1969 J. Mater. Sci. **4** 1106

Parrinello M and Rahman A 1980 Phys. Rev. Lett. **45** 1196

Parrinello M and Rahman A 1981 J. Appl. Phys. **52** 7182

Payne M C, Teter M P, Allan D C, Arias T A and Joannopoulos J D 1992 Rev. Mod. Phys. **64** 1045

Perry C H, Liu D W and Ingel R P 1985 J. Am. Ceram. Soc. **68** C184

Perry C H and Feinberg A 1980 Solid State Commun. **36** 519

Phillippi C M and Mazdiyasni K S 1971 J. Am. Ceram. Soc. **45** 5

Pople J A and Beveridge D L 1970 Approximate Molecular Orbital Theory (McGraw-Hill: New York)

Rahman A 1976 J. Chem. Phys. **65** 4845

Rapaport D C 1990 Computer Modelling of Fluids and Polymers eds C R A Catlow, S C Parker and M P Allen (Kluwer Academic: Dordrecht) chp 10

Rapp R A and Shores D A 1970 Techniques in Metals Research ed R F Bunshah (John Wiley: New York) **4**

Rhodes W H and Carter R E 1962 Bull. Am. Ceram. Soc. **41** 283

Rice M J, Strassler S and Toombs G A 1974 Phys. Rev. Lett. **32** 596

Roth W L 1972 J. Solid State Chem. **4** 60

Rohr F J 1966 B B C-Nachrichten **48** 200

Ruckley J D and Braslli D N 1967 J. Am. Ceram. Soc. **50** 220

Ruff O and Ebert F 1929 Z. Anorg. Allg. Chem. **180** 19

Sangster M J and Dixon M 1976 Adv. Phys. **25**[3] 247342

Saul P, Catlow C R A and Kendrick J 1985 Phil. Mag. B**51** 107

Schmalzried H and Pelton A D 1972 Am. Rev. Mater. Sci. **2** 143

Schuouler E, Hammou A and Kleitz M 1976 Mater. Res. Bull. **11** 1137

Shapiro S M 1976 Superionic Conductors eds G D Mahan and W L Roth (Plenum Press: New York) 261

Shimojo F and Okazaki H 1992 J. Phys. Soc. Jpn. **61** 4106

Shimojo F, Okabe T, Tachibana F, Kobayashi M and Okazaki H 1992 J. Phys. Soc. Jpn **61** 2848

Sindzingare P and Gillan M J 1988 J. Phys. C: Solid State Phys. **21** 4017

Smith D K and Cline C F 1962 J. Am. Ceram. Soc. **45** 249

Smith D K and Newkirk H W 1965 Acta Crystall. **18** 983

Solier de Dios J, Perez-Jubindo M A, Dominquez-Rodriguez A and Heuer A H 1989 J. Am. Ceram. Soc. **72** 1500

Steel D and Fender B E F 1974 J. Phys. C**7** 1

Steele B C H 1968 Elecromotive Force Measurements in High Temperature Systems ed C B Alcock (Elesevier: Amsterdam) 3

Steele B C H 1992 Mater. Sci. Eng. **13** 79

Steele B C H 1995 Solid State Ionics **75** 157

Steger J and Kostiner E 1973 J. Chem. Phys. **58** 3389

Stern E A 1958 Phys. Rev. **111** 786

Subbarao E C 1981 Advances in Ceramics eds A H Heuer and L N Hobbs 3 (Am. Ceram. Soc. : Ohio)

Suemoto T and Ishigame M 1986 Phys. Rev. B**33** 2757

Suzuki Y, Takahashi T and Nagae N 1981 Solis State Ionics **3 & 4** 483

Telton J 1944 Ann. Phys. Leipzig **5** 63

Telton J 1949 Ann. Phys. Leipzig **5** 71

Telton J 1950 Z. Phys. Chem. Leipzig **195** 197

Teufer G 1962 Acta Crystallogr. **15** 1187

Terblanche S P 1989 J. Appl. Crystallogr. **22** 283

Tien T Y and Subbarao E C 1963 J. Chem. Phys. **39** 1041

Tretyakov Y D and Kaul A R 1972 Physics of Electrolytes ed J Hladick **2** (Academic Press: New York)

Tuband C and Lorenz E 1914 Z. Phys. Chem. **87** 513

Tuiler M H, Dexpert-Ghys J, Dexpert H and Lagarde P 1987 J. Solid State Chem. **69** 153

Van Der Marel D and den Hartog H W 1982 Phys. Rev. B**25** 6602

Veal B W, Mckale A G, Paulikas A P, Rothman S J and Nowicki L J 1988

Physica B**150** 234

Wagner C 1943 Naturwissenschaften **31** 265

Walker J R 1982 in "Computer Simulation In the Physics and Chemistry of Solids" eds C R A Catlow and W C Mackrodt (Springer-Verlag: Berlin) 58

Walker J R and Catlow C R A 1981 J. Phys. C**19** L979

Watson G W, Tschaufeser P, Wall A, Jackson R A and Parker S C 1997 in "Lattice and Free Energy Minimisation Techniques" (Academic Press: New York)

Wedepohl P T 1967 Proc. Phys. Soc. **92** 79

Weissbart J and Ruka R 1962 J. Electrochem. Soc. **109** 723

Welch D O and Dienes 1975 Phys. Rev. B**11** 3060

Welch D O and Dienes 1977 J. Phys. Chem. Solids **38** 311

Wimmer E 1996 Mater Sci Eng **B37** 72

Wolff E G 1969 Rev. Sci. Instrum. **40** 544

Wyckoff R W G 1965 Crystal Structures (Interscience Publishers: New York) I 239